Numerical Modeling of Supercontinuum Generation in Optical Fibers

François St-Hilaire
Master of Engineering
Department of Electrical and Computer Engineering

McGill University
845 Sherbrooke St W
Montréal, QC H3A 0G4
January 31, 2020

A thesis submitted to McGill University in partial fulfillment of the requirements of the degree of Master of Engineering

ABSTRACT

This thesis reports the comparison of numerical modeling approaches for the extreme case of pulse propagation in optical fibers leading to supercontinuum generation. The widely-used generalized nonlinear Schrödinger equation is introduced along with two other propagation models, the Fourier-domain generalized Schrödinger equation and the nonlinear envelope equation, which are physically more accurate and retain the same first-order differential equation formalism. The performance of the three propagation model is investigated with simulations of different experimental results from the literature. The numerical results show that the Fourier-domain generalized Schrödinger equation and the nonlinear envelope equation are useful tools in specific cases and that the generalized nonlinear Schrödinger equation is nonetheless sufficiently accurate to model supercontinuum generation in a wide range of experimental conditions. This is subsequently corroborated in a practical example of supercontinuum source prototype optimization aided with numerical simulations.

RÉSUMÉ

Ce mémoire est une étude comparative des approches de modélisation numérique de la propagation d'impulsions lumineuses dans la fibre optique, spécifiquement appliquée au cas extrême de génération de supercontinuum. Largement utilisée en optique nonlinéaire, l'équation de Schrödinger nonlinéaire généralisée est présentée parallèlement avec deux modèles de propagation alternatifs, l'équation de Schrödinger non linéaire généralisée dans le domaine spectral et l'équation d'envelope nonlinéaire généralisée. Ces deux modèles alternatifs sont plus précis au niveau phénoménologique et conservent le même formalisme d'équation différentielle de premier ordre. La performance des trois modèles de propagation est évaluée au moyen de simulations de résultats expérimentaux provenant de la litérature. Les résultats numériques montrent que les deux models alternatifs peuvent être essentiels dans certains cas spécifiques, mais que l'équation de Schrödinger nonlinéaire généralisée demeure suffisament précise pour modéliser la génération de supercontinuum dans une large étendue de conditions expérimentales. Cette conclusion est ensuite corroborée par un exemple pratique d'optimisation d'un prototype de source supercontinuum à l'aide de simulations numériques.

ACKNOWLEDGMENTS

I would like to thank my supervisor, professor Martin Rochette, for his support and mentorship. I would also like to thank Thibaut Sylvestre from the Femto-ST institute for giving me the opportunity to work as part of his team for an internship.

I am also grateful for the financial support from professor Rochette, the SUPUVIR European project, the department of electrical and computer engineering of McGill University, the Mitacs organization, and the STARaCom strategic cluster.

Contents

List of Figures

Chapter 1: Introduction

Numerical modeling is an essential tool in the development of novel laser sources as it allows to gain insight on the physical mechanisms at play and sheds light on the effects of design changes and possible optimizations from the earliest stages of development to the final prototype. One of the more challenging elements to model in an optical system is nonlinear pulse propagation in waveguides: the interplay between linear and nonlinear interactions of light inside a waveguide gives rise to complex behaviours which in most cases cannot be predicted analytically. In optical fibers, these mechanisms (self-phase modulation, soliton formation, soliton fission, self-steepening, Raman scattering, etc.) have been extensively studied and theorized. While these nonlinear effects are often avoided and can be neglected in telecommunication systems, they play a key role in the generation of supercontinuum (SC) light. With their unique high brightness and large bandwidth characteristics, SC light sources are in high demand for applications in medicine, environmental monitoring, industrial processes, and sensing [1],[2]. In response to this, several research groups have invested efforts towards the development of SC sources with improved properties. Taking the Nonlinear Photonics Group at McGill University as an example, important characteristics of SC sources such as broad bandwidth but also low power consumption, brightness, and compactness have been the subject of many investigations [3],[4],[5],[6],[7],[8].

SC generation is an extreme case of pulse propagation in optical fiber where nonlinear effects interact to produce large spectral broadening. It was first observed in bulk glass by Alfano and Shapiro in 1970 [9]. Pulse propagation in this regime has been the subject of numerous studies, and is generally well understood. It is most commonly modeled with the generalized nonlinear Schrödinger equation (GNLSE) [2], a first-order differential equation that describes pulse propagation and includes the effects of dispersion and nonlinearity with some approximations. With the advent of novel speciality fibers and high-energy ultra-short laser sources, multi-octave spectral broadening and sub-cycle dynamics are now achievable experimentally. These effects go beyond what was observed in 1970 by Alfano and Shapiro, and beyond what is achievable in conventional silica fiber. Some approximations of the

GNLSE model become questionable in these cases. Consequently, efforts have been made to develop pulse propagation models with fewer approximations [10],[11],[12],[13] for more accurate simulations in these extreme regimes.

The propagation equations proposed by Laegsgaard [12] and by Kibler *et al.* [25] are of particular interest because they conserve the same simple formalism as the GNLSE are numerically solved with the same techniques. They are referred to as the Fourier-domain GNLSE (FD-GNLSE) and the generalized nonlinear envelope equation (GNEE) respectively. The aim of this work is to compare the performance of the GNLSE with these two alternative propagation models in the context of SC generation. Performance will be evaluated for the three models in terms of their ability to accurately model different physical mechanisms, and in terms of the time complexity of their algorithm.

This thesis is divided into seven chapters. After this introductory chapter, the GNLSE is derived from first principles to highlight the important approximations in the model. The FD-GNLSE and the GNEE models are then presented. The assumptions and approximation for the three models are then discussed. In chapter 3, an overview of the different SC generation mechanisms is presented. Chapter 4 presents the numerical methods used in this work to solve the three propagation equations and introduces the performance criteria. In Chapter 5, the three envelope equation models are compared quantitatively using these performance criteria. Four examples of experimental SC generation are used as references. In chapter 6, a practical example of SC source prototype optimization aided with numerical simulations is presented. This work is the result of a three-month internship at the Femto-ST institute in France. Finally, the conclusion is presented in chapter 7, where the results are summarized.

Chapter 2: Pulse Propagation Equations

In this chapter, three mathematical models for pulse propagation in optical fiber are introduced: the generalized nonlinear Schrödinger equation (GNLSE), the Fourier-domain GNLSE (FD-GNLSE), and the generalized nonlinear envelope equation (GNEE).

2.1 Derivation of a Propagation Equation from First Principles

This derivation closely follows the work presented in references [2] and [14] and aims to provide insight on the origin of the widely used nonlinear Schrödinger equation in optics. In the next subsection, it is shown how this propagation model can be adapted for short pulses ($<$ 1 ps) and extreme spectral broadening (*i.e.* the GNLSE). We start the discussion by defining the electric field $\mathbf{E}(\mathbf{r},t)$ of a pulse guided by an optical fiber. A z-propagating and linearly x-polarized field with a slowly varying envelope is assumed. Hence $\mathbf{E}(\mathbf{r},t)$ is described as the product of a rapidly oscillating field with a spatial and temporal envelope $E(\mathbf{r},t)$:

$$\mathbf{E}(\mathbf{r},t) = \frac{1}{2}\big(E(\mathbf{r},t)\exp[-\mathrm{i}\omega_0 t] + c.c.\big)\hat{\mathbf{x}} \tag{2.1}$$

where *c.c.* denotes the complex conjugate and $\mathbf{r}$ is the position vector with its origin at the center of the fiber cross-section. ω_0 is the reference frequency of the pulse, which is assumed far from any material resonances, and $E(\mathbf{r},t)$ is separated into its spatial and temporal envelopes:

$$E(\mathbf{r},t) = F(x,y)A(z,t)\exp[\mathrm{i}\beta_0 z] \tag{2.2}$$

where $F(x,y)$ is the transverse spatial distribution of the guided mode, β_0 is the corresponding propagation constant at the reference frequency, and $A(z,t)$ is the temporal pulse profile, with $|A|^2$ normalized to represent instantaneous power. Single-mode propagation only is considered, thus $F(x,y)$ is described as a two-dimensional Gaussian distribution as an approximation of the fundamental Bessel mode profile [2], [15]. The complex pulse envelope $A(z,t)$ will become central to the discussion as the propagation model is developed. It contains relevant information about pulse evolution: temporal profile, power, phase, chirp,

spectral phase, and spectral power density.

To model propagation of the pulse electric field $\mathbf{E}(\mathbf{r}, t)$ in a dielectric medium, the starting point is the set Maxwell's equations with current density, charge density, and magnetization set to zero:

$$\nabla \times \mathbf{E} = -\mu_0 \frac{\partial \mathbf{H}}{\partial t} \tag{2.3}$$

$$\nabla \times \mathbf{H} = \frac{\partial \mathbf{D}}{\partial t} \tag{2.4}$$

$$\nabla \cdot \mathbf{D} = 0 \tag{2.5}$$

$$\nabla \cdot \mathbf{H} = 0 \tag{2.6}$$

Where $\mathbf{H}$ is the magnetic field related to the pulse electric field $\mathbf{E}$, μ_0 is the vacuum permeability, and $\mathbf{D}$ is the electric flux density response in the medium:

$$\mathbf{D} = \epsilon_0 \mathbf{E} + \mathbf{P} \tag{2.7}$$

where ϵ_0 is the vacuum permittivity. The polarization response of the medium $\mathbf{P}$ is separated into a linear part $\mathbf{P}_L$ and a nonlinear part $\mathbf{P}_{NL}$: $\mathbf{P} = \mathbf{P}_L + \mathbf{P}_{NL}$. The effects of this linear and nonlinear polarization response will become clear later on. Optical fibers are made of amorphous materials with inversion symmetry and therefore exhibit third-order nonlinearity. Neglecting non-instantaneous molecular vibrations (Raman scattering) in the nonlinear term for now, the material response is described as:

$$\mathbf{P} = \mathbf{P}_L + \mathbf{P}_{NL} = \epsilon_0 \chi^{(1)} \cdot \mathbf{E} + \epsilon_0 \chi^{(3)} \vdots \mathbf{EEE} \tag{2.8}$$

Where $\chi^{(1)}$ and $\chi^{(3)}$ are the first and third order susceptibility tensors defined by the material properties of the fiber. It is worth noting that in general, the tensor products of $\mathbf{P}$ are described by time convolutions because of the frequency dependence of linear and nonlinear susceptibilities. This is considered when shifting to the frequency domain later on. Furthermore, without the inclusion of the delayed Raman response, $\chi^{(3)}$ is treated as constant for this derivation. With these definitions in place, the derivation of a propagation equation for the pulse envelope $A(z, t)$ can start. Taking the curl of equation 2.3, inserting equation 2.4

and using the definition for electric flux density (equation 2.7), the following equation for $\mathbf{E}$ is obtained:

$$\nabla \times \nabla \times \mathbf{E} = -\frac{1}{c^2}\frac{\partial^2 \mathbf{E}}{\partial t^2} - \mu_0 \frac{\partial^2 \mathbf{P}_L}{\partial t^2} - \mu_0 \frac{\partial^2 \mathbf{P}_{NL}}{\partial t^2} \tag{2.9}$$

Where c is the speed of light in vacuum. Then, using the following relation with $\nabla \cdot \mathbf{E} = 0$ from equation 2.5 (weak-guidance approximation, see section 2.5):

$$\nabla \times \nabla \times \mathbf{E} = \nabla(\nabla \cdot \mathbf{E}) - \nabla^2 \mathbf{E} = -\nabla^2 \mathbf{E} \tag{2.10}$$

the following equation is obtained:

$$\nabla^2 \mathbf{E} = \frac{1}{c^2}\frac{\partial^2 \mathbf{E}}{\partial t^2} + \mu_0 \frac{\partial^2 \mathbf{P}_L}{\partial t^2} + \mu_0 \frac{\partial^2 \mathbf{P}_{NL}}{\partial t^2} \tag{2.11}$$

This is now transferred to the frequency domain centered at the reference frequency with the Fourier transform:

$$\tilde{E}(\mathbf{r},\omega) = \int_{-\infty}^{\infty} \mathbf{E}(\mathbf{r},t)\exp[\mathrm{i}\omega t]\mathrm{d}t = \int_{-\infty}^{\infty} E(\mathbf{r},t)\exp[(\mathrm{i}(\omega-\omega_0)t]\mathrm{d}t = F(x,y)\tilde{A}(z,\omega)\exp[\mathrm{i}\beta_0 z] \tag{2.12}$$

and equation 2.11 becomes

$$\nabla^2 \tilde{E} = -\frac{\omega^2}{c^2}\tilde{E} - \omega^2 \mu_0 \tilde{P}_L - \omega^2 \mu_0 \tilde{P}_{NL} \tag{2.13}$$

The tilde superscript is used to denote Fourier space. At this point, both polarization terms are substituted by the result of their tensor product, which are both reduced to a single term since a linearly polarized electric field in $\hat{\mathbf{x}}$ far from any material resonances is assumed (see [14] for more details). For the linear term: $\tilde{P}_L = \epsilon_0 \tilde{\chi}^{(1)}_{xx} \tilde{E}$, where $\tilde{\chi}^{(1)}_{xx}$ is the frequency-dependent nonzero tensor element from $\chi^{(1)}$. For nonlinear polarization, the third-harmonic generation (THG) term that arises from the tensor product is neglected. $\tilde{P}_{NL}$ is transferred to the Fourier domain to obtain:

$$\tilde{P}_{NL} = \int_{-\infty}^{\infty} \frac{3\epsilon_0}{4}\chi^{(3)}_{xxxx}|E|^2 E \cdot \exp[(\mathrm{i}(\omega-\omega_0)t]\mathrm{d}t \approx \frac{3\epsilon_0}{4}\chi^{(3)}_{xxxx}|E|^2\tilde{E} \tag{2.14}$$

where $\chi^{(3)}_{xxxx}$ is the nonzero tensor element from $\chi^{(3)}$. Here, the frequency-dependence of $\chi^{(3)}$ is neglected and the quantity $\frac{3\epsilon_0}{4}\chi^{(3)}_{xxxx}|E|^2$ is treated as a constant in time. This is justified

by the slowly varying envelope approximation (SVEA) and the perturbative nature of this nonlinear term [2]. $\tilde{\chi}^{(1)}_{xx}$ and $\chi^{(3)}_{xxxx}$ are related to the refractive index and the nonlinear refractive index respectively. For now, the imaginary parts of $\tilde{\chi}^{(1)}_{xx}$ and $\chi^{(3)}_{xxxx}$ are neglected. They are related to linear and nonlinear losses respectively; their effect is included later on. Substituting the polarization terms, equation 2.13 then becomes:

$$\nabla^2 \tilde{E} = -\frac{\omega^2}{c^2}\tilde{E}\left(1 + \tilde{\chi}^{(1)}_{xx} + \frac{3}{4}\chi^{(3)}_{xxxx}|E|^2\right) \tag{2.15}$$

which is rewritten in the following form, with $\varepsilon(\omega) = 1 + \tilde{\chi}^{(1)}_{xx} + \frac{3}{4}\chi^{(3)}_{xxxx}|E|^2$:

$$\nabla^2 \tilde{E} = -\frac{\omega^2}{c^2}\tilde{E}\varepsilon(\omega) \tag{2.16}$$

$\tilde{E} = F(x,y)\tilde{A}(\omega,z)\exp[\mathrm{i}\beta_0 z]$ is now substituted and the separation of variables method is used to obtain separate equations for the mode profile $F(x,y)$ and the pulse envelope $\tilde{A}(\omega,z)$:

$$\nabla_T^2 F = \left(\bar{\beta}^2 - \tfrac{\omega^2}{c^2}\varepsilon(\omega)\right)F \tag{2.17}$$

$$\frac{\partial \tilde{A}}{\partial z} = \tfrac{\mathrm{i}}{2\beta_0}\left(\bar{\beta}^2 - \beta_0^2\right)\tilde{A} \tag{2.18}$$

Equation 2.18 is obtained by assuming that the pulse envelope is a slowly varying function of z and thus neglecting the second-order z-derivative term from the Laplacian. Here, $\bar{\beta}^2$ is introduced as a separation constant. Its relation with the propagation constant will become clear in the following.

The goal is now to obtain an explicit expression with known fiber parameters for $\bar{\beta}^2$ so that equation 2.18 becomes a practical pulse propagation equation. To start, the nonlinear part of $\varepsilon(\omega)$ is treated as a small perturbation and the unperturbed equation 2.17 is evaluated with $\varepsilon(\omega) = 1 + \chi^{(1)}_{xx}$. Using the relation between refractive index and linear susceptibility: $n^2 = 1 + \chi^{(1)}_{xx}$, and converting to cylindrical coordinates, equation 2.17 becomes

$$\frac{d^2F}{d\rho^2} + \frac{1}{\rho}\frac{dF}{d\rho} + \left(\frac{\omega^2}{c^2}n^2 - \bar{\beta}^2\right)F = 0 \tag{2.19}$$

In this form, equation 2.19 corresponds exactly to the Bessel differential equation describing the fundamental mode profile of a step-index fiber (see [2] for more details). Therefore, in

this unperturbed case, the eigenvalue $\tilde{\beta}$ is equivalent to the modal propagation constant $\beta(\omega)$. First order perturbation theory is now used to include the effect of the nonlinear part of $\varepsilon(\omega) = 1 + \tilde{\chi}^{(1)}_{xx} + \frac{3}{4}\chi^{(3)}_{xxxx}|E|^2$. $\varepsilon(\omega)$ is approximated as

$$\varepsilon(\omega) = (n + \Delta n)^2 \approx n^2 + 2n\Delta n \tag{2.20}$$

where it is assumed that $n >> \Delta n$. Δn is related to the nonlinear refractive index n_2 in the following way:

$$2n\Delta n = \frac{3}{4}\chi^{(3)}_{xxxx}|E|^2 \implies \Delta n = \frac{3}{8n}\chi^{(3)}_{xxxx}|E|^2 = n_2|E|^2 \tag{2.21}$$

In the same way, the perturbed eigenvalue $\bar{\beta}$ is rewritten as :

$$\bar{\beta} = \beta + \Delta\beta \tag{2.22}$$

where β is the modal propagation constant found from equation 2.19 (or in practice, found from dispersion measurements in the optical fiber) and $\Delta\beta$ is the first-order perturbation to the eigenvalue (its frequency dependence is implicit). Using $(\beta + \Delta\beta)^2 \approx \beta^2 + 2\beta\Delta\beta$, the perturbed case for equation 2.17 is:

$$\left[\nabla_T^2 + \frac{\omega^2}{c^2}n^2\right]F - \beta^2 F + \frac{\omega^2}{c^2}2n\Delta n F = 2\beta\Delta\beta F \tag{2.23}$$

It is assumed that this nonlinear index perturbation does not affect the modal distribution $F(x, y)$. It follows that the first two terms on the left side of equation 2.23 cancel out through their relation from the unperturbed equation 2.17. Following first-order perturbation theory [16], equation 2.23 is now multiplied by the conjugate F^* and integrated over the transverse plane on both sides:

$$\int\int F^*\frac{\omega^2}{c^2}2n\Delta n F \mathrm{d}x\mathrm{d}y = \int\int F^* 2\beta\Delta\beta F \mathrm{d}x\mathrm{d}y \tag{2.24}$$

Rearranging, this yields:

$$\Delta\beta = \frac{\omega^2 n}{c^2\beta}\frac{\int\int \Delta n|F(x,y)|^2\mathrm{d}x\mathrm{d}y}{\int\int |F(x,y)|^2\mathrm{d}x\mathrm{d}y} \tag{2.25}$$

The propagation equation for the pulse envelope (equation 2.18) is now written as

$$\frac{\partial\tilde{A}}{\partial z} = \mathrm{i}\Big(\beta + \Delta\beta - \beta_0\Big)\tilde{A} \tag{2.26}$$

where the approximation $(\tilde{\beta}^2 - \beta_0^2) \approx 2\beta_0(\tilde{\beta} - \beta_0)$ is used. To obtain the time-domain formulation of the nonlinear Schrödinger equation from equation 2.26, a few steps are still necessary. First, the propagation constant $\beta(\omega)$ is expanded as a Taylor series around the reference frequency ω_0:

$$\frac{\partial \tilde{A}}{\partial z} = \mathrm{i}\left[\left(\beta_1\Omega + \frac{\beta_2}{2}\Omega^2 + \frac{\beta_3}{6}\Omega^3 + ...\right) + \Delta\beta\right]\tilde{A} \tag{2.27}$$

where $\Omega = \omega - \omega_0$ and $\beta_m = \frac{\partial^m \beta}{\partial \omega^m}$. It is now clear how the linear polarization term P_L from the medium's electric flux density response directly leads to familiar phenomena such as group velocity, related to β_1, group velocity dispersion (GVD), related to β_2, third-order dispersion (β_3), and so on. Next, several approximations regarding the nonlinear perturbation $\Delta\beta$ are necessary. The propagation constant β is approximated as $\beta = \frac{\omega}{c} n_{\text{eff}} \approx \frac{\omega}{c} n$. Then, Δn is replaced by its definition (equation 2.21) and n_2 is factored out of the integral assuming it does not vary significantly along the fiber diameter. Finally, all frequency dependence (which is implicit in n_2 and $F(x, y)$) is dropped and $\Delta\beta$ is evaluated at the reference frequency:

$$\Delta\beta \rightarrow \Delta\beta_0 = \frac{\omega_0 n_2 |A|^2}{c} \frac{\int\int |F(x,y)|^4 \mathrm{d}x\mathrm{d}y}{\int\int |F(x,y)|^2 \mathrm{d}x\mathrm{d}y} \tag{2.28}$$

Converting to the time domain using the following inverse Fourier transform definition:

$$A(z,t) = \mathcal{F}^{-1}\{\tilde{A}(z,\Omega)\} = \frac{1}{2\pi}\int_{-\infty}^{\infty} \tilde{A}(z,\Omega)\exp[-\mathrm{i}\Omega t]\mathrm{d}\Omega \tag{2.29}$$

Equation 2.27 becomes:

$$\frac{\partial A(z,t)}{\partial z} = \mathrm{i}\sum_{k>1} \frac{\mathrm{i}^k \beta_k}{k!} \frac{\partial^k}{\partial t^k} A + \mathrm{i}\Delta\beta_0 A \tag{2.30}$$

As a final step, the following normalization is performed: $A \rightarrow \frac{A}{\sqrt{\int\int |F(x,y)|^2 \mathrm{d}x\mathrm{d}y}}$ and equation 2.30 is multiplied by $\sqrt{\int\int |F(x,y)|^2 \mathrm{d}x\mathrm{d}y}$ on each side to obtain the nonlinear Schrödinger equation:

$$\boxed{\frac{\partial A(z,t)}{\partial z} = \mathrm{i}\sum_{k\geq 1} \frac{\mathrm{i}^k \beta_k}{k!} \frac{\partial^k}{\partial t^k} A + \mathrm{i}\gamma_0 |A|^2 A} \tag{2.31}$$

where γ_0 is the nonlinear parameter at the reference frequency:

$$\gamma_0 = \frac{\omega_0 n_2(\omega_0)}{c A_{\text{eff}}(\omega_0)} \tag{2.32}$$

The effective mode area A_{eff} is obtained with the final normalization, it is defined as:

$$A_{\text{eff}} = \frac{\left(\int \int |F(x,y)|^2 \mathrm{d}x\mathrm{d}y \right)^2}{\int \int |F(x,y)|^4 \mathrm{d}x\mathrm{d}y} \tag{2.33}$$

Two of the more limiting approximations made in the derivation of the nonlinear Schrödinger equation are the omission of the delayed Raman response in the nonlinear polarization term and the omission of all frequency dependence in the nonlinear perturbation $\Delta\beta$. Those limit the validity of this propagation model to cases for which the pulse bandwidth is much smaller than the reference frequency ($\Delta\omega << \omega_0$). In the next subsection, as the first of the three propagation models, the *generalized* version of the nonlinear Schrödinger equation is introduced. It is valid for much shorter pulses (<1 ps) and accurately models significant spectral broadening.

2.2 The Generalized Nonlinear Schrödinger Equation

Building upon the model derived in the previous section, the GNLSE is now introduced. The GNLSE has two essential additions that enable a more accurate modeling of short pulses and large bandwidth dynamics [17]: the Raman term and the nonlinear shock term. The Raman term is first added.

In deriving the standard nonlinear Schrödinger equation, it is assumed that the nonlinear polarization consists exclusively of instantaneous electronic response. The total nonlinear response function $R(t)$, which takes into account both the instantaneous electronic response (Kerr nonlinearity) and the delayed molecular response (Raman effect) is now introduced. With the inclusion of this delayed response, the nonlinear polarization tensor product (equation 2.8) has to be described as a time convolution:

$$P_{NL} = \frac{3\epsilon_0}{4} \chi^{(3)}_{xxxx} \int_{-\infty}^{t} R(t-t') E^*(t-t') E(t-t') \mathrm{d}t' \tag{2.34}$$

where the upper integral bound t ensures causality. Following the same perturbation theory development used in the previous section, it can be shown [17] that the inclusion of the Raman effect with $R(t)$ leads to the following propagation equation:

$$\frac{\partial A(z,t)}{\partial z} = \mathrm{i}\sum_{k\geq 1}\frac{\mathrm{i}^k\beta_k}{k!}\frac{\partial^k}{\partial t^k}A + \mathrm{i}\gamma_0\left[A\int_0^\infty R(t')|A(z,t-t')|^2\mathrm{d}t'\right] \tag{2.35}$$

where it is assumed that $R(t)$ is normalized such that $\int_{-\infty}^{\infty} R(t)\mathrm{d}t = 1$. Analytical forms of the full response function $R(t)$ are generally not known for isotropic glass materials. $R(t)$ is therefore often separated into an instantaneous electronic response modeled with a Dirac delta function $\delta(t)$, and a delayed molecular response $h_R(t)$:

$$R(t) = (1-f_R)\delta(t) + f_R h_R(t) \tag{2.36}$$

where f_R is the fraction of the Raman contribution to the total nonlinear response. If the Raman gain spectrum contains a single peak, the Raman response function $h_R(t)$ is often modeled in the following way [17]:

$$h_R(t) = (\tau_1^{-2} + \tau_2^{-2})\tau_1 \exp(-t/\tau_2)\sin(t/\tau_1) \tag{2.37}$$

where τ_1 is the inverse of the phonon frequency in the material and τ_2 is related to the bandwidth of the Raman gain peak. Figure 2.1 shows $h_R(t)$ extracted from experimental measurements for a silica fiber. The corresponding characteristic timescales are $\tau_1 = 12.2$ fs and $\tau_2 = 32$ fs.

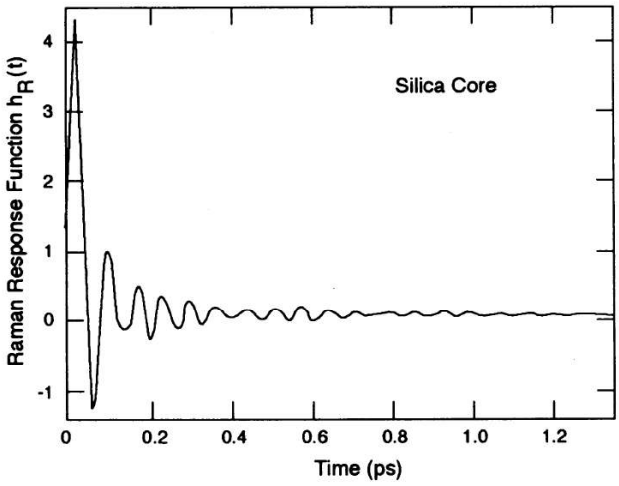

Figure 2.1: $h_R(t)$ for a silica fiber, taken from [2].

Alternatively, if the Raman gain spectrum $g_R(\Omega)$ is known, it can be fitted with a sum of Gaussian functions and $h_R(t)$ can be extracted with [18]:

$$h_R(t>0) = C \cdot \int_0^\infty g_R(\Omega)\sin(\Omega t)\mathrm{d}\Omega \tag{2.38}$$

where C is a normalization constant chosen such that $\int_{-\infty}^{\infty} h_R(t)\mathrm{d}t = 1$. With this definition of $R(t)$, the total nonlinear convolution is equivalent to:

$$\int_0^\infty R(t')|A(z,t-t')|^2\mathrm{d}t' = (1-f_R)|A|^2 + f_R(h_R \circledast |A|^2) \tag{2.39}$$

where $\circledast$ denotes convolution.

The nonlinear shock term is now added to the propagation equation to obtain the GNLSE. The nonlinear shock term is a first-order correction on γ_0 to account for the frequency dependence of γ:

$$\gamma(\omega) = \frac{\omega n_2(\omega)}{cA_{\text{eff}}(\omega)} \tag{2.40}$$

This amounts to expanding $\gamma(\omega)$ as a Taylor series around the reference frequency, keeping only the first two terms, and transferring back to the time domain:

$$\gamma(\Omega) \approx \gamma_0 + \gamma_1\Omega \xrightarrow{\mathcal{F}^{-1}} \gamma_0 + \mathrm{i}\gamma_1\frac{\partial}{\partial t} \tag{2.41}$$

with $\gamma_1 = \frac{\partial\gamma}{\partial\omega}$ evaluated at ω_0. Adding this to the propagation equation, the GNLSE is obtained:

$$\boxed{\frac{\partial A(z,T)}{\partial z} = \mathrm{i}\sum_{k\geq 2}\frac{\mathrm{i}^k\beta_k}{k!}\frac{\partial^k}{\partial T^k}A + \mathrm{i}\gamma_0\left(1+\mathrm{i}\tau_0\frac{\partial}{\partial T}\right)\left[A\cdot R(T)\circledast|A|^2\right]} \tag{2.42}$$

where $\tau_0 = \gamma_1/\gamma_0$ is referred to as the shock time-scale, often approximated by $\tau_0 \approx 1/\omega_0$. It can be calculated to also contain the dispersion of both $n_2(\omega)$ and $A_{\text{eff}}(\omega)$ [19]:

$$\tau_0 = \frac{1}{\omega_0} - \left[\frac{1}{A_{\text{eff}}(\omega)}\frac{\mathrm{d}A_{\text{eff}}}{\mathrm{d}\omega}\right]_{\omega_0} + \left[\frac{1}{n_2(\omega)}\frac{\mathrm{d}n_2}{\mathrm{d}\omega}\right]_{\omega_0} \tag{2.43}$$

In the numerical examples presented in this work, n_2 will be considered constant either because of its negligible contribution to the dispersion of $\gamma(\lambda)$ or because of a lack of experimental $n_2(\lambda)$ data for materials such as ZBLAN or F2 glass. For example, in silica glass

pumped at 850 nm, the n_2 contribution (3rd term in equation 2.43) is $3.5 \cdot 10^{-17}$ s according to data from [20]. In comparison, the contribution from the $1/\omega_0$ term is more than ten times larger at $4.5 \cdot 10^{-16}$ s. As will be seen in the numerical examples, the A_{eff} contribution can range from negligible to significant depending on the waveguide properties.

This shock term is responsible for what is known as pulse *self-steepening*, where group velocity becomes intensity-dependent [2],[21]. In equation 2.42, the time t is transferred to a frame of reference moving with the group velocity of the pulse: $T = t - \beta_1 z$. The Raman convolution (shown equation 2.35) is represented with the symbol $\circledast$ on the right side. It is important to stress two limitations regarding the shock term. First, τ_0 is only a first-order correction to γ_0 and therefore does not account for the full frequency dependence of $A_{\text{eff}(\omega)}$ and $n_2(\omega)$. Second, the inclusion of the frequency dependence of γ and its expansion into a Taylor series are performed *a posteriori*, which is not perfectly well founded in light of the derivation presented in the previous section, where the frequency dependence of $\Delta\beta$ is dropped all together before converting back to the time domain and normalizing to extract γ_0. In other words, the frequency dependence of γ has to be neglected to obtain the time-domain nonlinear Schrödinger equation (2.31), but it is then introduced in the GNLSE without mathematical basis. That being said, as will be seen with different numerical examples in chapters 5 and 6, this approximation (equation 2.43) is sufficient in most situations. With the inclusion of the shock term and the Raman effect, the GNLSE is adequate for broadband propagation, with pulse duration approaching the single-cycle regime and bandwidths up to $\sim \omega_0/3$ [17],[19]. It is important to note that this bandwidth limitation applies to coherent pulses, the GNLSE still accurately models incoherent spectral broadening over multiple octaves. Moreover, the GNLSE can be readily implemented for numerical simulations with the split-step Fourier method, which is described in section 4.1.1. For those reasons, the GNLSE is generally seen as the workhorse of nonlinear optics simulations.

2.3 The Fourier-Domain Generalized Schrödinger Equation

The second of the three propagation equation models presented in this work is the Fourier-domain GNLSE (FD-GNLSE). The main motivation for this model is to preserve the full

frequency dependence of the nonlinear perturbation $\Delta\beta$ (equation 2.25), so that the dispersion of fiber parameters A_{eff}, n_{eff}, and n_2 are accurately modeled over large bandwidths. This leads to a different definition of the nonlinear parameter γ. In this work, we simply introduce the FD-GNLSE without derivation. The reader is referred to Laegsgaard's paper [12] and Koleski *et al.* [22] for a detailed derivation. It is important to note, however, that as with the GNLSE, this derivation still relies on the SVEA. As presented in [1], the FD-GNLSE is written as:

$$\boxed{\frac{\partial \tilde{A}'(z,\Omega)}{\partial z} = \mathrm{i}\cdot\bar{\gamma}\cdot\exp[-\tilde{D}z]\mathcal{F}\left\{\bar{A}\cdot R \circledast |\bar{A}|^2\right\}} \tag{2.44}$$

In this model, the pulse evolution is described as an ordinary differential equation in the Fourier domain. As with the GNLSE, the Raman effect is included in the nonlinear response convolution denoted with $\circledast$. The Fourier-domain pulse envelope $\tilde{A}$ is moved into what is called the *interaction picture* with the following change of variable:

$$\tilde{A}'(z,\Omega) = \tilde{A}(z,\Omega)\exp(-\tilde{D}(\Omega)z) \tag{2.45}$$

where $\tilde{D}(\Omega) = \mathrm{i}(\beta(\Omega) - \beta_1\Omega - \beta_0)$ is the dispersion operator, equivalent to time-domain dispersion operator $\mathrm{i}\sum_{k>2}\frac{\mathrm{i}^k\beta_k}{k!}\frac{\partial^k}{\partial T^k}$ in the GNLSE (equation 2.42) transferred to the Fourier space. As previously mentioned, the derivation of this equation leads to a different definition of the nonlinear parameter:

$$\bar{\gamma}(\Omega) = \frac{\omega n_2 n_{\text{eff}}(\omega_0)}{c n_{\text{eff}} A_{\text{eff}}^{1/4}} \tag{2.46}$$

Moreover, the nonlinear response convolution is evaluated with the time-domain pulse envelope normalized in the following way:

$$\bar{A}(z,T) = \mathcal{F}^{-1}\left\{\frac{\tilde{A}(z,\Omega)}{A_{\text{eff}}^{1/4}(\Omega)}\right\} \tag{2.47}$$

In addition to correctly modeling the dispersion of nonlinearity, equation 2.44 has the advantage of being a *non-stiff* differential equation thanks to the interaction-picture change of variable, which removed the stiff dispersive part [1], *i.e.* the dispersion operator. The stiffness of a differential equation refers to its tendency to produce rapid variations in the numerical solution with small changes to the initial conditions [23]. The removal of the stiff term makes the FD-GNLSE suitable for numerical integration with Runge-Kutta methods.

2.4 The Generalized Nonlinear Envelope Equation Model

The third propagation model presented in this work is the generalized nonlinear envelope equation model (GNEE). Both the GNLSE and the FD-GNLSE rely on the SVEA, which limits their validity in situations where the pulse bandwidth exceeds $\sim \omega_0/3$ (*i.e.* ultrashort pulses with durations <5 fs). In ref. [13], Genty *et al.* bypass the SVEA and obtain a first order propagation equation by separating the backward and forward propagating fields (see [24] for details). The motivation for this model is to obtain a propagation equation with the same simple GNLSE formalism, but with no bandwidth constraint. The resulting GNEE is as follows [13]:

$$\boxed{\frac{\partial A(z,T)}{\partial z} = \mathrm{i}\sum_{k\geq 2}\frac{\mathrm{i}^k\beta_k}{k!}\frac{\partial^k}{\partial T^k}A + \mathrm{i}\gamma_0\left(1+\mathrm{i}\tau_0\frac{\partial}{\partial T}\right)\left((1-f_R)\left[|A|^2+\frac{1}{3}A^2\mathrm{e}^{-\mathrm{i}2\omega_0 T}\right]A + f_R g(z,T,A)\right)} \tag{2.48}$$

where $g(z,T,A)$ is the Raman convolution term:

$$g(z,T,A) = \frac{2}{3}\left[h_R(T)\circledast|A|^2\right]A + \frac{2}{3}\mathrm{e}^{-\mathrm{i}\omega_0 T}\left[h'_R(T)\circledast|A|^2\right]\mathrm{Re}(\mathrm{e}^{-\mathrm{i}\omega_0 T}A) \tag{2.49}$$

with $h'_R(T) = h_R(T)\exp(-\mathrm{i}2\omega_0 T)$. As mentioned, the GNEE has the same structure as the GNLSE: the first term on the right models dispersion in the same way, and nonlinearity is modeled through γ_0 and the shock term, which can be corrected to account for the dispersion of A_{eff} and n_2 (equation 2.43). The difference lies in the nonlinear response convolution. For the instantaneous electronic contribution ($1-f_R$ term), there is an added term: $\frac{1}{3}A^2\mathrm{e}^{-\mathrm{i}2\omega_0 T}$ which models the contribution of THG (THG is neglected in the derivation of the GNLSE). Although THG is usually non-phase-matched in single-mode optical fibers, this higher harmonic term can have a significant contribution to the blue-shifted spectral broadening in highly-nonlinear fibers ([13], [25], [26]). For the delayed Raman response (f_R term), the model used here is derived from [27] and contains rapidly oscillating terms from the sub-cycle interactions of the Raman frequency components. Having the same structure as the GNLSE, equation 2.48 is also numerically solvable with the split-step Fourier method.

2.5 Assumptions and Approximations

In this subsection, the major assumptions and approximations on which the three propagation equation models rely (the GNLSE, FD-GNLSE, and GNEE) are discussed.

- **The weak-guidance approximation**

  All three propagation models are derived from Maxwell's equations by approximating $\nabla \cdot E = 0$ (see equation 2.10). This amounts to assuming that susceptibility $\varepsilon(x, y)$ is homogeneous in space, which is only valid if the fiber has a simple step-index geometry and is *weakly guiding*, that is if the refractive index difference between core and cladding is very small (see [15] for more details). This allows to treat the guided field as a *scalar* mode with no component in the z direction (*i.e.* completely transverse) and ultimately obtain unidirectional propagation equations for the pulse envelope. This approximation is sufficient in most cases for a qualitative assessment of SC dynamics, even in different non-weakly-guiding fibers (*e.g.* step index with high index contrast, microwires, and photonic-crystal fibers) [1],[28],[25]. However, it has been shown [29] that a full vectorial approach for deriving a propagation equation leads to a different definition of γ and an effective nonlinearity up to $\sim$2 times stronger than with the scalar definition in *strongly-guiding* fibers. Despite this, most models used in simulations for *strongly-guideing* fibers in the litterature rely on the scalar approximation [1].

- **The SVEA**

  Both the GNLSE and the FD-GNLSE rely on the SVEA. As mentioned earlier, this limits their validity to cases where the pulse bandwidth does not exceed $\omega_0/3$. This condition is satisfied most of the time, unless extremely short pulse durations are involved [13]. For example, the GNLSE and FD-GNLSE are still valid for pulses as short as 10 fs at 1060 nm under this condition. However, if significant spectral broadening occurs on the blue-shifted side of the pump, the higher-harmonics terms in the GNEE could provide more accurate modeling.

- **Single-mode propagation**

  All three equations presented in this work are simplified to model single-mode propaga-

tion, *i.e.* propagation of the fundamental mode. For SC generation, even when pumping in the single-mode regime, blue-shifted spectral broadening can excite higher-order modes which have different dispersion and nonlinear properties [15]. Multi-mode pumping has been shown to lead to complex spatio-temporal nonlinear dynamics [30],[31], and generalized multi-mode propagation models have been presented in the literature [32],[33]. In this work, we focus on fundamental mode pumping with the GNLSE, FD-GNLSE, and GNEE, and therefore neglect excitation of higher-order modes.

- **Birefringence**

  Fiber birefringence is neglected for all three propagation models. With the GNLSE, the effects of birefringence can be easily accounted for by considering two coupled equations (one for each polarization state) with an added cross-phase modulation term in the nonlinear part [2].

- **Losses**

  Losses are omitted in the three propagation equations for conciseness. In each case, linear losses can be added directly to the dispersion operator in the frequency domain: $\tilde{D}(\Omega) = \mathrm{i}(\beta(\Omega) - \beta_1\Omega - \beta_0) - \alpha(\Omega)/2$, where $\alpha(\Omega)$ is the linear loss coefficient in m^{-1}. Nonlinear loss from two-photon absorption is ignored here as it is often negligible in the transparency windows of fibers [2].

Chapter 3: Theory of Supercontinuum Generation in Optical Fibers

This section presents an overview of the key physical mechanisms involved in SC generation for three different pumping regimes of dispersion and pulse duration. Concepts of nonlinear fiber optics are used here without introduction, namely self-phase modulation (SPM), four-wave mixing (FWM), solitons, and Raman-induced frequency shifts (RIFS). The reader is referred to [2] and[14] for a thorough description of these phenomena, and to [1] for a detailed account of the history of SC sources.

3.1 Ultrashort Pulses in the Anomalous Dispersion Regime

SC generation can be achieved by pumping with ultrashort pulses (typically below $\sim$ 1 ps) in the anomalous dispersion regime of an optical fiber [34],[35],[36]. For example Ranka *et al.* [35] obtained a SC spanning from 400 to 1400 nm by pumping a microstructured silica fiber at wavelength of 790 nm (anomalous dispersion) with pulses of 100 fs duration and $\sim$8 kW peak power. The main physical mechanism that initiates large spectral broadening in this regime is known as *soliton fission* [28],[37]. As a reminder, the soliton order N is given by:

$$N^2 = \frac{\gamma_0 P_0 T_0^2}{|\beta_2|} \tag{3.1}$$

Where T_0 is the soliton duration and P_0 is the peak power. When a high-order soliton (N>1) is excited in a fiber it, initially compresses its duration until it reaches a point where the perturbative effects of higher-order dispersion (β_3, β_4,...) and self-steepening are significant. At this point, the N^{th}-order soliton breaks into a collection of N fundamental solitons of deterministic duration and peak power given by [2]:

$$T_k = \frac{T_0}{2N + 1 - 2k} \tag{3.2}$$

$$P_k = \frac{(2N + 1 - 2k)^2}{N^2} P_0 \tag{3.3}$$

where k goes from 1 to N. T_k is the duration of the kth fundamental soliton, and P_k is its peak power. After this point, further spectral broadening occurs with the propagation of

the N fundamental solitons. On the red-shifted side, spectral broadening occurs through the continuous red-shift $\Delta\nu$ of each soliton induced by RIFS:

$$\Delta\nu(z) = -\frac{4T_R|\beta_2|}{15\pi T_0^4}z \tag{3.4}$$

where T_0 is the soliton duration and $T_R = \int_0^\infty \mathrm{R(t)tdt}$. As the fundamental solitons propagate in the fiber, they are perturbed by higher-order dispersion, losses, and self-steepening. To compensate for this, the solitons continuously adjust their parameters by shedding part of their energy in the form of dispersive waves [1],[2]. A soliton at a given frequency ω_s will emit a dispersive wave at a frequency ω_d for which the phase velocity is the same as the nonlinearly propagating soliton. For fibers with a single zero-dispersion wavelength (ZDW) and red-shifted solitons, ω_d lies on the short-wavelength side of the pump. The dispersive wave frequency is approximated by [2] :

$$\omega_d \approx -\frac{3\beta_2}{\beta_3} + \frac{\gamma P_s \beta_3}{3\beta_2^2} + \omega_s \tag{3.5}$$

As a result, further spectral broadening occurs on the blue-shifted side as the soliton frequency ω_s continuously decreases from RIFS.

3.2 Quasi-CW Pulses in the Anomalous Dispersion Regime

SC generation can also be achieved by pumping with quasi-CW or continuous-wave (CW) light in the anomalous dispersion regime [38],[39],[40]. In terms of SC generation mechanisms, pump pulses with durations longer than ∼10 ps can be considered quasi-CW: the process of SC generation with such pulses is identical to the CW case. Unlike the mechanisms of soliton fission that drives SC generation with ultrashort pulses, *modulation instability* (MI) is the main phenomenon that initiates large spectral broadening for quasi-CW pulses and CW pumps. MI is a nonlinear phenomenon that occurs in the anomalous dispersion regime. It is analogous to a FWM process that is phase-matched by the nonlinear phase shift of SPM. When a CW or quasi-CW pump is injected in the anomalous dispersion regime, MI will amplify certain frequencies from quantum noise or amplitude fluctuations of the pump. This leads to the apparition of two sidebands around the pump frequency. Their specific

frequencies relative to the pump (Ω_{MI}) are given by the phase matching condition [2]:

$$\beta_2\Omega_{\mathrm{MI}}^2 + \frac{\beta_4}{12}\Omega_{\mathrm{MI}}^4 + 2\gamma_0 P_0 = 0 \tag{3.6}$$

MI also enables Raman amplification of noise both on the Stokes and anti-Stokes side via FWM (see [41] for more details). This amplification of noise and amplitude fluctuations from MI and Raman gain eventually breaks up the quasi-CW pump into a chaotic train of thousands of ultrashort femtosecond pulses, which evolve into fundamental solitons. Since this process is seeded by random noise and both MI and Raman gain have a certain bandwidth, solitons with a wide range of durations and peak powers are formed within the initial quasi-CW pulse envelope. This contributes to the initial broadening of the spectrum. After the train of solitons has been formed, the main mechanism that contributes to large spectral broadening on the long-wavelength side is the RIFS of each individual soliton. As seen with equation 3.4, the RIFS of an individual soliton strongly depends on its duration T_0. For a train of thousands of solitons with variable durations T_0, this will therefore generate a smooth continuum on the long-wavelength side because each one experiences a different RIFS over the total propagation length. Another mechanism that further extends the continuum on the long-wavelength side is called *soliton collision*. If at any point during propagation there is a coherent temporal overlap between one soliton and a more red-shifted soliton, the first soliton can act as a pump for Raman amplification of the more red-shifted soliton. After amplification, the red-shifted soliton compresses its duration T_0 to conserve its fundamental soliton number $N = 1$. This compression then leads to greater RIFS upon propagation, thus further broadening the long-wavelength side of the continuum. Broadening on the blue-shifted side again produced by the dispersive waves emitted by the perturbed soliton propagation.

3.3 Normal Dispersion Regime

SC generation has also been achieved in the normal dispersion regime without the involvement of solitons and dispersive waves [40],[42],[3]. The physical mechanisms at play in this regime are not as straightforward as in the anomalous dispersion regime, but usually involve SPM, FWM, and Raman amplification. For example, Abeeluck *et al.* [40] have shown that cascaded Raman amplification is the main phenomenon that seeds SC generation with

CW pumping in highly nonlinear fibers. Yuan *et al.* [42] have shown that pumping photonic crystal fibers (PCF) with ultra short pulses produces SC by SPM and phenomenon called *optical wave-breaking*. Wave-breaking can be simply seen as FWM between different frequency components of a single pulse [2],[43]. On the other hand, Hudson *et al.* [3] have achieved broadband mid-infrared SC generation by pumping ultrashort pulses in an all-normal dispersion chalcogenide microwire. The extreme nonlinearity involved in their experiment make it difficult to isolate the mechanisms at play. It can be interpreted as a chaotic mix of SPM, wave-breaking, cascaded FWM, and cascaded Raman amplification.

Chapter 4: Numerical Methods

As one might expect from the nonlinear nature of the three propagation equations studied here, the GNLSE, FD-GNLSE, and GNEE do not lend themselves to analytical treatment. This section presents the numerical methods used to solve these equations and discuss the important practical details of implementing such numerical schemes in Matlab. Example codes for the three propagation models are presented in the appendix.

4.1 The Split-Step Fourier Method

4.1.1 Overview of the Algorithm

The split-step Fourier Method (SSFM) is the most widely used numerical method to solve the GNLSE [2],[44]. As mentioned before, the GNEE also lends itself to the SSFM in the exact same manner. To make matters more simple, the GNLSE is used as the example to introduce the SSFM. To begin, the GNLSE (equation 2.42) is rewritten in the following way:

$$\frac{\partial A(z,T)}{\partial z} = \left(\hat{D} + \hat{N}\right)A \tag{4.7}$$

where $\hat{D}$ is what is called the dispersion operator, and $\hat{N}$, the nonlinear operator. Following equation 2.42 $\hat{D}$ is given by:

$$\hat{D} = \mathrm{i}\sum_{k\geq 2}\frac{\mathrm{i}^k\beta_k}{k!}\frac{\partial^k}{\partial T^k} - \frac{\alpha}{2} \tag{4.8}$$

As a reminder, $\hat{D}$ can be converted to the Fourier domain to obtain a simpler form:

$$\tilde{D}(\Omega) = \mathrm{i}\left[\frac{\beta_2}{2!}\Omega^2 + \frac{\beta_3}{3!}\Omega^3 + \frac{\beta_4}{4!}\Omega^4 + ...\right] - \frac{\alpha(\Omega)}{2} = \mathrm{i}[\beta(\Omega) - \beta_0 - \beta_1\Omega] - \frac{\alpha(\Omega)}{2} \tag{4.9}$$

where the frequency dependence of losses can be directly included. The nonlinear operator has the following form:

$$\hat{N} = \frac{1}{A}\cdot \mathrm{i}\gamma_0\left(1 + \mathrm{i}\tau_0\frac{\partial}{\partial T}\right)\left[A\cdot R \circledast |A|^2\right] \tag{4.10}$$

Notice that the $1/A$ factor appears because A cannot be factored out of the square brackets when the time derivative from the shock term is considered. The idea behind the SSFM is to divide the total propagation length L into small z-steps of size h and to approximately

solve equation 4.7 over each small step by treating dispersion ($\hat{D}$) and nonlinearity ($\hat{N}$) independently, *i.e.* by successively setting $\hat{D} = 0$ and evaluating $\hat{N}$, then setting $\hat{N} = 0$ and evaluating $\hat{D}$, and so on. This is schematized in figure 4.1.

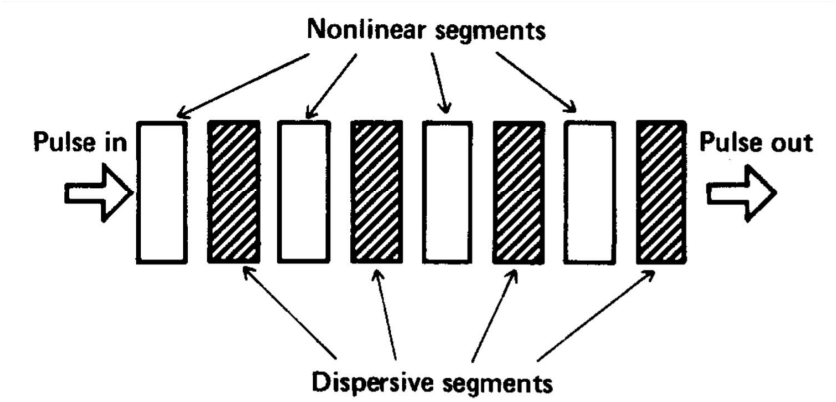

Figure 4.1: Schematic of the SSFM algorithm, taken from [44]

For a small step in z, starting at an arbitrary point z_0, the nonlinear part of the equation is first solved:

$$\frac{\partial A(z,T)}{\partial z} = \mathrm{i}\gamma_0 \left(1 + \mathrm{i}\tau_0 \frac{\partial}{\partial T}\right) \left[A \cdot R \circledast |A|^2\right] \tag{4.11}$$

when the shock term is ignored (in which case $\hat{N} = \mathrm{i}\gamma_0 R \circledast |A|^2$) the solution at $z = z_0 + h$ is found in a straightforward manner by approximating $|A|^2$ as constant over the small step h, *i.e.* $|A(z,T)|^2 \to |A_0|^2 = |A(z_0,T)|^2$ and simply integrating from z_0 to z . We call the solution to the nonlinear step A_{NL}:

$$A_{\mathrm{NL}} = A(z,T) \cdot \exp[\hat{N}_0(z - z_0)] \tag{4.12}$$

where $\hat{N}_0 = \mathrm{i}\gamma_0 R \circledast |A_0|^2$. When the shock term is considered, however, the integration of equation 4.11 is more involved. Theoretically, one could use the same technique, but with the full definition of the nonlinear operator (equation 4.10). However, this approach is numerically unstable in practice because of the $1/A$ factor. To include the shock term, the approach presented by Blow and Wood [17] is followed here. The shock term is treated as a perturbation and the following change of variables is used:

$$V(z,T) = A(z,T) \cdot \exp[-\hat{N}_0 \cdot (z - z_0)] \tag{4.13}$$

Where $\hat{N}_0 = \mathrm{i}\gamma_0 R \circledast |A_0|^2$ is the unperturbed nonlinear operator. From equation 4.11, this yields:

$$\frac{\partial V}{\partial z} = \mathrm{i}\gamma_0 R \circledast \left[|V|^2 - |V_0|^2\right] - \gamma_0 \tau_0 \frac{\partial}{\partial T}\left[V \cdot R \circledast |V|^2\right] \tag{4.14}$$

where $V_0 = A_0 = A(z = z_0, T)$. Treating the shock term as a perturbation, the approximation $\frac{\partial}{\partial T}\left[A \cdot R(T) \circledast |V|^2\right] \approx \frac{\partial}{\partial T}\left[V \cdot R(T) \circledast |V|^2\right]$ is used. A second-order Runge-Kutta scheme is now used to integrate equation 4.14 over the step size h. The variation of V at $z = z_0$ is:

$$k_1 = \left.\frac{\partial V}{\partial z}\right|_{z=z_0} = -\gamma_0 \tau_0 \frac{\partial}{\partial T}\left[V_0 \cdot R \circledast |V_0|^2\right] \tag{4.15}$$

A first estimate of $V(z_0 + h/2, T)$ is then found with:

$$V_1 = V(z_0 + h/2, T) = V_0 + k1\frac{h}{2} \tag{4.16}$$

The variation of V at $z = z_0 + h/2$ is now estimated by:

$$k_2 = \left.\frac{\partial V}{\partial z}\right|_{z=z_0+h/2} = \mathrm{i}\gamma_0 R \circledast \left[|V_1|^2 - |V_0|^2\right] - \gamma_0 \tau_0 \frac{\partial}{\partial T}\left[V_1 \cdot R \circledast |V_1|^2\right] \tag{4.17}$$

An estimate of V at $z = z_0 + h$ is then found:

$$V(z_0 + h, T) = V_0 + k_2 h \tag{4.18}$$

Inverting the change of variables, the solution for the nonlinear step with the shock term included is

$$A_{\mathrm{NL}} = V(z_0 + h, T) \cdot \exp[\hat{N}_0 h] \tag{4.19}$$

The solution of the nonlinear step A_{NL} is now used as the input for the dispersive step. For the dispersive step, $\hat{N} = 0$ is assumed and the dispersive part of the GNLSE is solved independently:

$$\frac{\partial A(z,T)}{\partial z} = \hat{D}A = \mathrm{i}\sum_{k\geq 2} \frac{\mathrm{i}^k \beta_k}{k!} \frac{\partial^k}{\partial T^k} A - \frac{\alpha}{2} A \tag{4.20}$$

To solve this, it is transferred to the Fourier domain using equation 4.9:

$$\frac{\partial \tilde{A}(z,\Omega)}{\partial z} = \tilde{D}A = \mathrm{i}\left[\beta(\Omega) - \beta_0 - \beta_1 \Omega\right]\tilde{A} - \frac{\alpha(\Omega)}{2}\tilde{A} \tag{4.21}$$

This equation is solved by direct integration: $\tilde{A}(z_0 + h, \Omega) = \tilde{A}(z_0, \Omega) \cdot \exp[\tilde{D}h]$. To get the full estimate (nonlinearity and dispersion included) of the solution after one step, the dispersion step is applied on the solution to the nonlinear part A_{NL} in the Fourier domain and then transferred back to the time domain:

$$A(z_0 + h, T) = \mathcal{F}^{-1}\Big(\mathcal{F}\big(A_{\mathrm{NL}}\big) \cdot \exp[\tilde{D}h]\Big) \tag{4.22}$$

This solution is then used as the input for the next step, and the process is repeated until the total propagation length L is reached.

4.1.2 Error Analysis for the SSFM Algorithm

We now focus on the error of the SSFM algorithm relative to the step size h. The two sources of error in this algorithm are the second-order Runge-Kutta integration of the nonlinear part and the independent treatment of the effects of $\hat{D}$ and $\hat{N}$. By definition, the second-order Runge-Kutta integration has a local error that is third-order with step size $\mathcal{O}(h^3)$ [17]. The dominant error term comes from the independent treatment of $\hat{D}$ and $\hat{N}$. Treating the two operators independently amounts to approximating them as commutative (*i.e.* $\hat{D}\hat{N}A \approx \hat{N}\hat{D}A$), which is not the case [2]. A more formal solution to equation 4.7 should be written as:

$$A(z_0 + h, T) = \exp\big[(\hat{D} + \hat{N})h\big]A(z_0, T) \tag{4.23}$$

However, the SSFM algorithm approximates this solution in the following way:

$$\exp\big[(\hat{D} + \hat{N})h\big]A(z_0, T) \approx \exp[\hat{D}h]\exp[\hat{N}h]A(z_0, T) \tag{4.24}$$

Using the following relation for two non-commutative operators [2]:

$$\exp[\hat{D}h]\exp[\hat{N}h] = \exp\left[(\hat{D} + \hat{N})h + \frac{h^2}{2}[\hat{D}, \hat{N}] + \mathcal{O}(h^3)\right] \tag{4.25}$$

where $[\hat{D}, \hat{N}] = \hat{D}\hat{N} - \hat{N}\hat{D}$ is the commutator for $\hat{D}$ and $\hat{N}$. The dominant error term is $\frac{h^2}{2}[\hat{D}, \hat{N}]$ and thus second-order with step size $\mathcal{O}(h^2)$. Therefore, the local error for the SSFM algorithm follows $\mathcal{O}(h^2)$ and the global error follows $\mathcal{O}(h)$. A symmetrized version of the SSFM algorithm can be easily implemented to improve on this and achieve second-order

global accuracy $\mathcal{O}(h^2)$ [45]. The idea for each step is to propagate through half a dispersion step, then a full nonlinear step, and finally the remaining half of the dispersion step:

$$A(z_0 + h, T) = \exp[\hat{D}\frac{h}{2}] \exp[\hat{N}h] \exp[\hat{D}\frac{h}{2}] A(z_0, T) \tag{4.26}$$

When the shock term is involved, the nonlinear step should be carried out with the Runge-Kutta scheme presented in section 4.1.1.

4.2 The Fourth-Order Runge-Kutta Method

The FD-GNLSE (equation 2.44) can be solved numerically with any explicit Runge-Kutta method. Following [46], the fourth-order Runge-Kutta (RK4) method is presented here. From equation 2.44, the four slope estimates k_1 through k_4 are given by:

$$k_1 = \mathrm{i}\bar{\gamma} \cdot \exp[-\tilde{D}z_0]\mathcal{F}\left\{ \bar{A}(z_0, T) \cdot R \circledast |\bar{A}(z_0, T)|^2 \right\} \tag{4.27}$$

$$\tilde{A}'_1 = \tilde{A}'(z_0, T) + k_1 \tfrac{h}{2} \tag{4.28}$$

$$k_2 = \mathrm{i}\bar{\gamma} \cdot \exp[-\tilde{D}(z_0 + \tfrac{h}{2})]\mathcal{F}\left\{ \bar{A}_1 \cdot R \circledast |\bar{A}_1|^2 \right\} \tag{4.29}$$

$$\tilde{A}'_2 = \tilde{A}'(z_0, \Omega) + k_2 \tfrac{h}{2} \tag{4.30}$$

$$k_3 = \mathrm{i}\bar{\gamma} \cdot \exp[-\tilde{D}(z_0 + \tfrac{h}{2})]\mathcal{F}\left\{ \bar{A}_2 \cdot R \circledast |\bar{A}_2|^2 \right\} \tag{4.31}$$

$$\tilde{A}'_3 = \tilde{A}'(z_0, \Omega) + k_3 h \tag{4.32}$$

$$k_4 = \mathrm{i}\bar{\gamma} \cdot \exp[-\tilde{D}z_0 + h]\mathcal{F}\left\{ \bar{A}_3 \cdot R \circledast |\bar{A}_3|^2 \right\} \tag{4.33}$$

where A'_n is related to $\bar{A}_n$ through equation 2.47. The approximate solution for one step is given by:

$$\tilde{A}'(z_0 + h, \Omega) = \tilde{A}'(z_0, \Omega) + \left(\frac{k_1}{6} + \frac{k_2}{3} + \frac{k_3}{3} + \frac{k_4}{6} \right) h \tag{4.34}$$

The global accuracy of this method is of fourth-order with step size $\mathcal{O}(h^4)$. This gain of accuracy over the symmetrized SSFM comes at the cost of a more involved algorithm. Moreover, a practical implementation of this algorithm necessitates at least 16 discrete Fourier transform operations per iteration (as seen in the Matlab code in Appendix B), which introduces

round-off errors. As will be seen in the numerical results, this hinders the RK4 algorithm's convergence rate in certain cases. In comparison, the SSFM algorithm for the GNLSE requires only 6 discrete Fourier transform operations per iteration. On the other hand, the RK4 method has the advantage of being easily implemented in Matlab with the built-in ordinary differential equation solver `ODE45` [47].

4.3 Practical Implementation in Matlab

In this subsection, we elaborate on a few key concepts for a practical implementation of the SSFM and the RK4 method in Matlab.

4.3.1 Time and Frequency Discretization

The windowing and discretization of time (T) and frequency (Ω) is a crucial step in nonlinear pulse propagation modeling: it must be carefully accomplished so that both time and frequency-domain interactions are accurately captured when numerically solving a propagation equation. The following parameters define the time and relative frequency $\Omega/2\pi$ windows and increment size. They are all related in the following way:

$$\begin{cases} \texttt{Nt} \rightarrow \text{Number of sampling points in time and frequency} \\ \texttt{dT} \rightarrow \text{Time increment size} \\ \texttt{Tmax} = \texttt{Nt} \cdot \texttt{dT}/2 \rightarrow \text{Time window defined from } \texttt{-Tmax} \text{ to } \texttt{Tmax} \\ \texttt{fmax} = 0.5/\texttt{dT} \rightarrow \text{Frequency window defined from } \texttt{-fmax} \text{ to } \texttt{fmax} \\ \texttt{df} = 1/(\texttt{Nt} \cdot \texttt{dT}) \rightarrow \text{Frequency increment size} \end{cases}$$

Using these definitions, the time window actually represents time delay centered at the peak of the pulse, such that the leading edge of the pulse is situated in *negative* time and the trailing edge in positive time. Also, the frequency window actually represents frequency difference centered at the reference frequency of the pulse, such that blue-shifted components

have positive frequency and red-shifted components have *negative* frequency.

In the simulations, the number of sampling points `Nt` and the time window size `Tmax` are defined first. The other parameters are then based on the values chosen for `Nt` and `Tmax`. The first consideration for this choice is that the time window size `Tmax` must be large enough so that throughout the propagation length, the field intensity stays effectively 0 at the edges of the time window. This ensures that the signal does not fold over the sampling window during fast Fourier transform (FFT) conversions. The choice of `Nt` also requires careful attention. `Nt` should be a power of 2 (e.g. 2^{19}) to optimize computation time: the fast-Fourier transform algorithm in Matlab is optimized for vectors with lengths that are powers of 2. More importantly, `Nt` must be large enough so that the frequency window size `fmax` can contain the entire spectrum at each point along the propagation length.

4.3.2 The Fast Fourier Transform in Matlab

The FFT function in Matlab (`fft`) and its inverse (`ifft`) are built-in functions that calculate the discrete Fourier transform. Throughout this work, the following definitions for the analytical Fourier transform are used:

$$\tilde{A}(z,\Omega) = \mathcal{F}\{A(z,T)\} = \int_{-\infty}^{\infty} A(z,T)\exp[\mathrm{i}\Omega T]\mathrm{d}T \tag{4.35}$$

$$A(z,T) = \mathcal{F}^{-1}\{\tilde{A}(z,\Omega)\} = \frac{1}{2\pi}\int_{-\infty}^{\infty} \tilde{A}(z,\Omega)\exp[-\mathrm{i}\Omega T]\mathrm{d}\Omega \tag{4.36}$$

The built-in `fft` and `ifft` functions in Matlab use the inverse sign convention for the exponential term and a different scaling [48]. To obtain the correct scaling and the same sign convention, one could define the following compound functions and use them when transferring back and forth between time and Fourier domains:

$$\texttt{Af} = \texttt{FT(A,Nt,dT)} := \texttt{Nt}\cdot\texttt{dT}\cdot\texttt{fftshift(ifft(ifftshift(A)))} \tag{4.37}$$

$$\texttt{A} = \texttt{IFT(Af,df)} := \texttt{df}\cdot\texttt{fftshift(fft(ifftshift(Af)))} \tag{4.38}$$

where `Af` is the discretized frequency-domain envelope and `A` is the discretized time-domain envelope. Here the `fftshift` and `ifftshift` functions are built-in Matlab functions that

are used to shift vectors to and from the *shifted* space, where their zero component ($T = 0$ and $\Omega = 0$) are shifted to the first element of the vector. For example, in the *normal* space, `A` is the pulse envelope vector with its maximum value (the pulse peak at $T = 0$) at the center of the vector. To obtain the discrete Fourier transform 4.37 with a definition coherent with 4.35, it is transferred to the shifted space, which is the natural way that the `ifft` and `fft` functions interpret their input vector. The `ifft` is then applied to account for the different sign convention. The vector is then shifted back to normal space and scaled with $\texttt{Nt} \cdot \texttt{dT}$. These compound functions are useful for writing more understandable code, however they come at the cost of more computing time. A more optimized way to transfer to and from the Fourier domain is to perform all calculations in the shifted space and shift back to normal space only for data visualization.

4.3.3 Adjusting the Frequency Window

In some situations, the frequency windows requires to be adjusted to avoid negative values in absolute frequency and wavelength. Let `Omega` be the angular frequency difference vector ranging from $-2\pi \cdot \texttt{fmax}$ to $2\pi \cdot \texttt{fmax}$. The absolute frequency vector `w` is then given by $\texttt{w} = \texttt{Omega} + \texttt{w0}$, where `w0` is the reference angular frequency. In some cases, the spectral broadening on the short wavelength side of a SC is large enough that new spectral components are separated from `w0` by a frequency difference larger than `w0` (*i.e.* the bandwidth of a SC may be larger than the reference frequency ω_0). This requires that $2\pi \cdot \texttt{fmax} > \texttt{w0}$, which creates negative values in the absolute frequency vector `w`. This is generally undesirable as it can create problems such as negative values for the propagation constant or the nonlinear parameter. This problem can be bypassed by shifting the center of the frequency window vector `f`. The following shows an example of how this can be implemented with the built-in `circshift` function.

```
%% Time and Frequency Discretization

Nt = 2^14;                          % Number of sampling points
Tmax = 10e-12;                      % Time window limit [s]
T = linspace(-Tmax,Tmax,Nt);        % Time delay vector [s]
dT = 2*Tmax/Nt;                     % Time increment [s]
fmax = 0.5/dT;                      % Frequency window limt [Hz]
df = (2*fmax)/Nt;                   % Frequency increment [Hz]
f = linspace(-fmax,fmax,Nt);        % Unshifted frequency vector [Hz]

f_shift = linspace(-(fmax-0.4*fmax),fmax+0.4*fmax,Nt);  % Shifted frequency vector [Hz]
shift = -round(Nt*0.4/2);                               % Shift for pulse spectrum

Omega_shift = 2.*pi.*f_shift;       % Angular frequency vector [rad/s]
dOmega = 2*pi*df;                   % Angular frequency increment [rad/s]
lam0 = 850e-9;                      % Central wavelength [m]
c = 299792458;                      % Speed of light [m/s]
w0 = 2*pi*c/lam0;                   % Central angular frequency [rad/s]
w = Omega_shift+w0;                 % Absolute angular frequency vector [rad/s]
lam = 2.*pi.*c./w;                  % Wavelength vector [m]

T_FWHM = 200e-15;                   % Pulse FWHM duration [s]
T0 = T_FWHM/1.7627;                 % Pulse 1/e duration [s]
P0 = 1e3;                           % Peak power [W]

A0 = sqrt(P0).*sech(T./T0);         % Initial pulse profile
Af0 = FT(A0,Nt,dT);                 % Initial unshifted pulse spectrum
Af0_shift = circshift(Af0,shift);       % Initial shifted pulse spectrum
```

In this example, a 200 fs pulse centered at 850 nm is considered, and the desired wavelength window is from 350 nm to 2 microns. Here, `Nt` and `Tmax` are defined first and the other parameters are computed from those values. The values for `Nt` and `Tmax` are chosen so that `fmax` is sufficiently large to include short wavelengths (high frequencies) down to 350 nm in the frequency vector `f`. However, in this case, if the frequency vector `f` is not shifted, the large negative frequency limit `-fmax` will cause negative values in the absolute frequency vector `w`. Here, the shifted frequency vector `f_shift` is shifted by `0.4*fmax` *i.e.* the negative limit is reduced by `0.4*fmax` and the positive limit is increased by the same amount. It is crucial that the shift is symmetric to preserve the equivalences between `df` and `Nt`. Using `f_shift`, wavelength values ranging from 324 nm to 2.8 microns are obtained in the wavelength vector `lam`, which covers the desired window. With this shifted frequency window, the pulse spectrum is computed in two steps. First the Fourier transform of the

time-domain pulse profile (`A0`) is computed with the `FT` compound function described the previous section. Second, the resulting vector is shifted with the built-in `circshift` function so that the position of the peak of the spectrum in the vector corresponds to the position of the zero in the shifted frequency vector `f_shift`. The value of `shift` depends on the amount by which the frequency limits are modified. The resulting shifted spectrum is shown with the time-domain profile in figure 4.2.

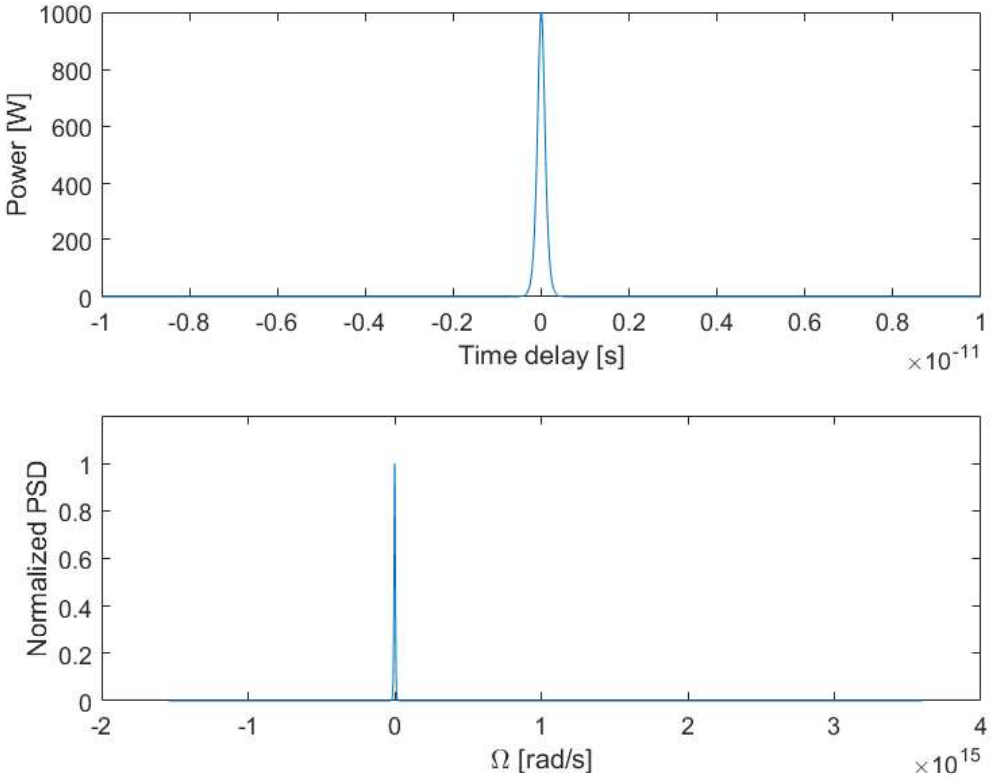

Figure 4.2: Time-domain profile and shifted spectrum for a 1 kW 200 fs pulse centered at 850 nm.

It is important to note that a shifted spectrum must be shifted back by an amount `-shift` before being converted to the time domain with the `IFT` function so that the correct phase and scaling are preserved: `A0 = IFT(circshift(Af0_shift,-shift),df)`.

4.4 The Adaptive Step Size Method and Convergence Criterion

A crucial step in modeling nonlinear pulse propagation is defining the longitudinal step size h. To accurately model the effects of nonlinearity and dispersion, h must be much smaller than both the dispersion length and the nonlinear length:

$$h << L_{\mathrm{NL}} = \frac{1}{\gamma P_0}$$
$$h << L_{\mathrm{D}} = \frac{T_0^2}{|\beta_2|}$$

where P_0 is the peak power, and T_0 is the $1/e$ pulse width. These two conditions must hold throughout the propagation length. As discussed in the theory section (section 2.5), pumping with a quasi-CW laser, for example, leads to the break-up of the pulse into fundamental solitons with variable peak powers P_0 and durations T_0. The choice of h is therefore not as straightforward in this case. Typically, L_{NL} is a much more limiting factor than L_{D} for the step size h because of the high peak powers reached in the different SC generation regime. When the soliton train starts propagating, the maximal peak power varies significantly along the propagation distance z because of randomly occurring soliton collisions. This means that the condition $h << L_{\mathrm{NL}}$ can change drastically along z. This is also true for soliton fission, where the higher-order input soliton is initially compressed. To account for this, an adaptive step size method for is used in our algorithms: the nonlinear phase-rotation method (see [49] for more details). This method consists of limiting the nonlinear phase-shift $\phi_{\mathrm{NL}} = \gamma_0 P_0 h$ to a sufficiently small value at each iteration, *i.e.* the step size h is adapted at each iteration to optimize computing time and accuracy. For a train of soliton pulses, the maximal phase-shift is calculated from the maximal soliton peak power P_0^{max}. Every iteration i, the step size $h(i)$ is determined by :

$$h(i) = \frac{\phi_{max}}{\gamma_0 P_0^{max}(i)} \tag{4.39}$$

A convergence criterion is now defined to allow to find suitable values for ϕ_{max} for the

simulations. Following reference [45], a normalized global simulation error is defined as:

$$\text{Error} = \frac{||\tilde{A}_{fine} - \tilde{A}_{coarse}||}{||\tilde{A}_0||} \tag{4.40}$$

where $||\tilde{A}|| = \sqrt{\int |\tilde{A}|^2 \mathrm{d}\omega}$. $\tilde{A}_{fine}$ is the output spectrum simulated with a very *fine* step size (*i.e.* a very low value for ϕ_{max}), $\tilde{A}_{coarse}$ is the output spectrum simulated with a more coarse step size (*i.e* with the chosen value for ϕ_{max}), and $\tilde{A}_0$ is the input spectrum. For convergence analysis, ϕ_{max} is at least two times less for the fine *reference* solution $\tilde{A}_{fine}$. An error of 10^{-1} or less is sufficient for convergence: further refining the step size to obtain a lower error does not produce any visible difference in the output spectrum. This convergence criterion of Error $< 10^{-1}$ allows for a more complete comparison of the three models in terms of precision and computing time.

In this work, the value of ϕ_{max} necessary for convergence will be referred to as the *convergence rate*. This value is used in parallel with the computing time and the goodness of fit criterion defined in the next subsection to quantify the performance of each model for a particular simulation. Although the convergence rate for a simulation strongly depends on the accuracy of the numerical integration scheme (SSFM or RK4 method), a convergence analysis allows to compare the numerical accuracy of different models solved with the same integration scheme, *i.e.* the GNLSE and the GNEE sovled with the SSFM. It also allows to put into perspective the numerical precision and computing time for the FD-GNLSE solved with the RK4 scheme, which is mathematically more precise than the SSFM ($\mathcal{O}(h^4)$ versus $\mathcal{O}(h)$ globally).

4.5 The Goodness of Fit Criterion

As discussed in section 2.5, all three propagation models rely on several important approximations and assumptions. Moreover, the exact experimental conditions for a particular experiment cannot be retrieved and used in simulations. For these reason, the propagation models are generally used for a qualitative comparison with experimental measurements, *i.e.* to interpret the underlying physical mechanisms, compare total spectral bandwidth and

temporal profile, and estimate coherence degradation. In this work, however, the coefficient of determination R^2 is used to quantify and compare the performance of the three propagation models in their ability to accurately predict experimental output spectra. R^2 is a number between 0 and 1 that gives information about the goodness of a fit, with $R^2 = 1$ corresponding to a perfect match between experimental and simulated data. R^2 is defined as [50]:

$$R^2 = 1 - \frac{\sum_i (y_i - \bar{y})^2}{\sum_i (y_i - f_i)^2} \tag{4.41}$$

where y_i is the ith numerical data point $\bar{y}$ is the mean of all numerical data points, and f_i is the ith experimental data point. In the context of optical pulse propagation, the numerical data corresponds to the simulated output spectra, and the experimental data corresponds to the measured output spectra. As will be seen in the next section, the SC generation process can produce heavy and chaotic modulations in the output spectrum, which are impossible to precisely recreate via simulation due to a lack of knowledge of the exact experimental conditions and the model approximations. For this reason, the goodness-of-fit coefficient R^2 is expected to be low in some cases (<0.5), even if the overall behaviour is well reproduced. It is nonetheless a useful tool to compare and quantify the performance of the three models in terms of total bandwidth and general spectral dynamics.

Chapter 5: Comparison of the Three Envelope Equation Models

This chapter reports the investigation of the performance of the three envelope equation models presented in this work: the GNLSE, the FD-GNLSE, and the GNEE. To achieve this aim, the three models are used to simulate pulse propagation and SC generation in four different fibers reported in the literature and the results are compared with the experiment. The four examples are strategically chosen to represent typical experimental settings for SC generation or to showcase the differences between the three simulation models. Various types of fibers are studied in the four examples to show the extent of the propagation models. The first is a chalcogenide glass fiber, the second is a F2 glass PCF, the third is a Fluorine-doped silica fiber, and the fourth is a silica microwire. For each example, performance is quantified via the three criteria discussed in the previous chapter: the goodness of fit (R^2 parameter), the convergence rate ($\phi_{\max}$ necessary for convergence), and the resulting computing time. As a reference, the computing times are measured on a core i5-8350U processor at 1.7 GHz.

5.1 Example 1: Large Bandwidth Mid-Infrared SC

In this example, simulations are carried out with the experimental conditions reported in reference [36]. In their article, Petersen *et al.* report on the generation of SC spanning the 2 to 12 μm region by pumping in the normal dispersion regime of a high-numerical-aperture chalcogenide step-index fiber. The experimental conditions for the pump pulse are shown in table 1

Table 1: Experimental pump parameter

Pump Parameter	P_0 [kW]	T_{FWHM} [fs]	λ_0 [μm]
Value	691.9	100	4.5

The fiber used in this experiment is a high-index-contrast step-index chalcogenide fiber. The core is made of $As_{40}Se_{60}$ glass and has a diameter of 16 μm. The cladding is made of a lower index germanium-based chalcogenide glass. The dispersion curve of the fiber

is shown in figure 5.1 (a). The dispersion and the loss data are taken directly from [36]. The zero-dispersion wavelength (ZDW) of the fiber is 5.83 μm. Figure 5.1 (b) shows the calculated effective mode area and the resulting nonlinear coefficient γ over the bandwidth of interest. The effective mode area is calculated by solving the characteristic equation for the fundamental mode of a step-index geometry with the wavelength dependent core and cladding indices provided in [36] (see [15] and [2] for more details). The nonlinear index $n_2 = 4.893 \cdot 10^{-18}$ m^{2}W^{-1} is taken from [51] and is assumed constant over the entire bandwidth. From this, the nonlinear parameter $\gamma(\lambda)$ (equation 2.40) is calculated and shown in figure 5.1. The Raman response for this chalcogenide glass is modeled with equation 2.37. The characteristic timescales τ_1 and τ_2 are taken from [52]. They are shown in table 2 along with the other fiber parameters. The fiber losses used in the simulations are shown in figure 5.2.

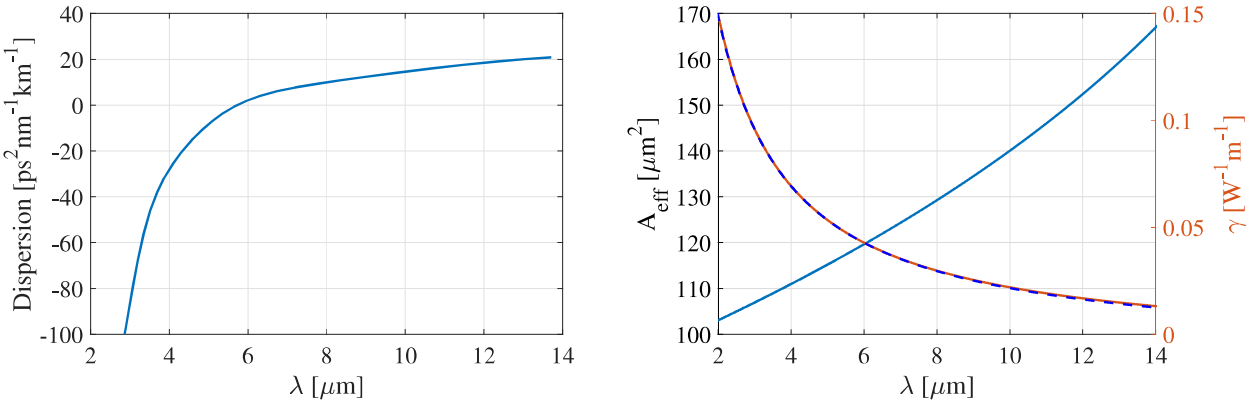

(a) (b)

Figure 5.1: (a) Dispersion curve of the step-index chalcogenide fiber with a ZDW of 5.83 μm. (b) Calculated effective mode area (blue), nonlinear parameter (orange), and approximation of the nonlinear parameter with a corrected shock term: $\gamma \approx \gamma_0 + \gamma_0\tau_0\Omega$ (dotted line).

Table 2: Parameters of the chalcogenide step-index fiber

Parameter	L [cm]	n_2 [m^2/W]	A$_{\text{eff}}(\lambda_0)$ [μm^2]	γ_0 [km^{-1}W^{-1}]	f_R	τ_1 [fs]	τ_2 [fs]
Value	8.5	$4.893{\cdot}10^{-18}$	113	60	0.1	23.2	195

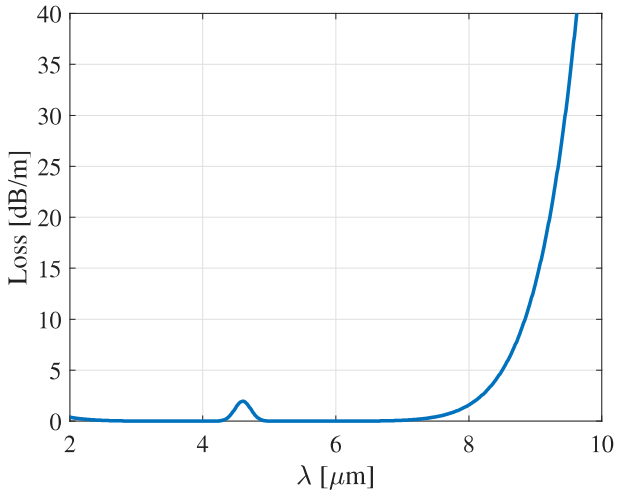

Figure 5.2: Loss coefficient used in the simulations, modeled after [36].

The numerical results of simulations carried out with all three propagation models are now presented. To begin, the models are tested with lower peak power against the experimental output spectrum for 67 kW coupled peak power provided by Petersen *et. al.*. This allows to introduce the performance comparison scheme with a simpler example. The numerical results are shown in figure 5.3 along with the experimental output spectrum. All three models show good agreement with the experimental total bandwidth and replicate the dip in the spectrum around 5.83 μm caused by the transition from normal to anomalous dispersion. This similarity in the numerical results is expected, because the three models are almost equivalent for these experimental conditions. For the FD-GNLSE, the dispersion of effective mode area is slow relative to wavelength: less than 70 μm^2 in the total 12 μm of bandwidth. Consequently, the corrected shock term is sufficient to model the dispersion of γ (as seen in figure 5.1 (b) with the dotted line), so the FD-GNLSE is equivalent to the GNLSE. For the GNEE, higher-harmonic dynamics would occur outside the transparency window of the fiber, below 2 μm, this means that it is also equivalent to the GNLSE.

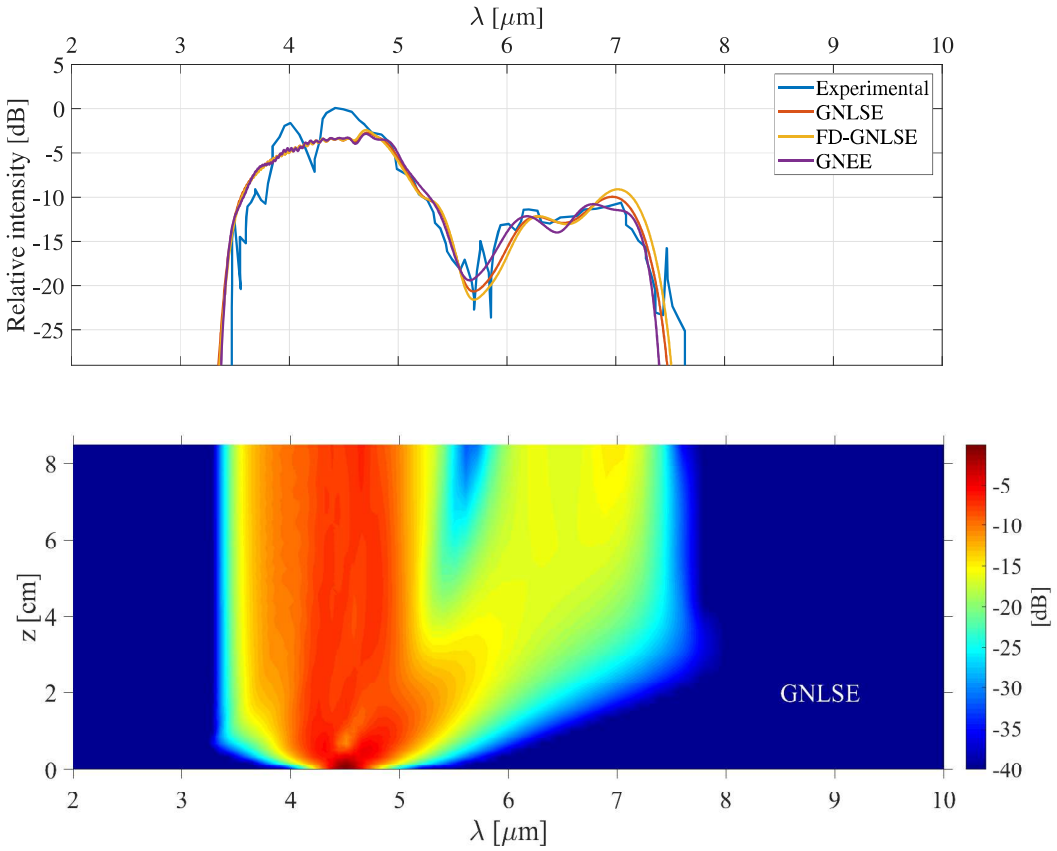

Figure 5.3: Simulated spectral evolution along the fiber with the GNLSE (bottom) and comparison of the three numerical output spectra with the experimental output spectrum (top) for 67 kW coupled peak power (simulated with 13.4 kW peak power).

Table 3 shows the performance comparison of the three models with the R^2 parameter, the convergence rate, and the computing time. The peak power used in the simulations is 13.4 kW, which is 20% of the experimental peak power. This is a common phenomenon in SC simulations: lower peak power is required in simulations to achieve spectral broadening and dynamics similar to the experimental case. This is mainly attributed to experimental conditions which are not accounted for in the propagation models: measurement uncertainty, coupling to an orthogonal polarization, and coupling to higher-order modes of the fiber [36]. As expected from figure 5.3, the fit is good and R^2 is high for all three models. The only differentiating factors are computing time and the convergence criterion (Error$< 10^{-1}$) for the maximum nonlinear phase shift ϕ_{max}. The convergence analysis is presented in figure 5.4. The RK4 method used with the FD-GNLSE converges faster to Error$= 10^{-1}$, which

is expected because the algorithm has higher accuracy ($\mathcal{O}(h^4)$). For the same ϕ_{max} as the GNLSE, computing time is significantly higher for the GNEE due to the more involved calculations the model requires.

Table 3: Numerical results with Nt= 2^{16}, P_0 = 13.4 kW

Model	GNLSE	FD-GNLSE	GNEE
R^2	0.71	0.72	0.73
$1/\phi_{\max}$	50	12.5	50
CPU time [s]	14	12	24

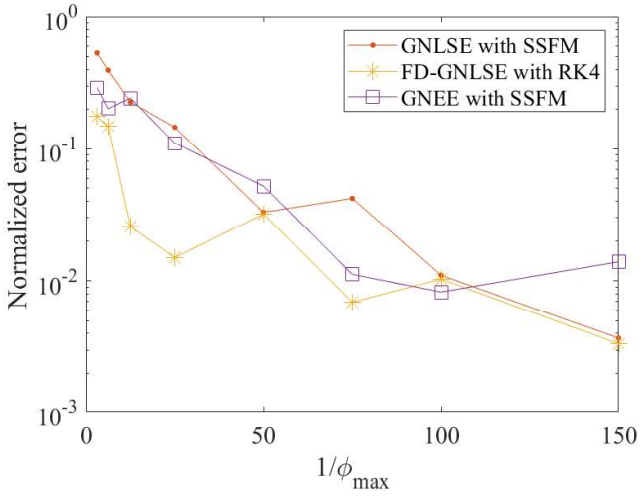

Figure 5.4: Convergence analysis for the three numerical methods with 13.4 kW (simulated) peak power

The focus is now shifted on one of the main results from Petersen *et al.*: the large bandwidth SC generated by pumping the same fiber with 692 kW peak power. The results are presented in figure 5.5. Heavy and chaotic modulations can be seen in the output spectrum due to large SPM and soliton interactions in the anomalous dispersion regime (above 5.83 μm) [36]. Qualitatively, the overall spectral dynamics and total SC bandwidth are relatively well reproduced by all three simulation models. The red-shifted edge of the SC is limited by the transmission window of the fiber, which ends around 12 μm. The main differ-

ence lies in the heavy spectral modulations, which are significantly stronger in the simulated spectra than in the experiment. This is also a recurring phenomenon in SC simulation and is attributed to the spectral resolution being much higher in simulations than what is possible to measure experimentally with a spectrometer [3]. For the same reasons mentioned for the low coupled peak power case, the three models perform almost equally in terms of the goodness of fit parameter R^2. The values achieved for R^2 are relatively low because of the heavy spectral modulations. The convergence analysis is shown in figure 5.6. The GNLSE with the SSFM has the highest convergence rate in this case. This is most likely due to the fact that the SSFM algorithm is more *stable* for this case with chaotic spectral modulations because it has less FFTs per step than the RK4 FD-GNLSE and the GNEE. The GNLSE algorithm contains 6 FFT operations per step, compared to 16 for the FD-GNLSE with the RK4 method and 10 for the GNEE with the SSFM. The discrete nature of the FFT introduces a round-off error, which accumulates as numerical noise over all the FFT operations [53]. This phenomenon is illustrated in figure 5.7, where the 10000 FFT operations are performed on the initial spectrum and the noise floor rises by 75 dB as a consequence. This does not affect the overall SC behaviour, but is seen to have an effect on the evolution of noise-sensitive fine spectral modulations. Furthermore, the high-frequency terms in the GNEE add to the noise sensitivity of the spectral modulations in this case. As a consequence, the GNEE has the slowest convergence rate. This noise sensitivity is significant enough that the convergence criterion (Error $< 10^{-1}$) cannot quite be achieved with reasonable computing time for the FD-GNLSE with RK4 and the GNEE with the SSFM. However, the simulations show that the overall behaviour is stable at the chosen maximal phase shift value of $1/\phi_{\max} = 200$ for the FD-GNLSE and the GNEE.

From these results, it is clear that the GNLSE is the most effective simulation model for these experimental conditions as it requires much less computing time and has a better convergence rate than the FD-GNLSE and GNEE for qualitatively identical output spectra.

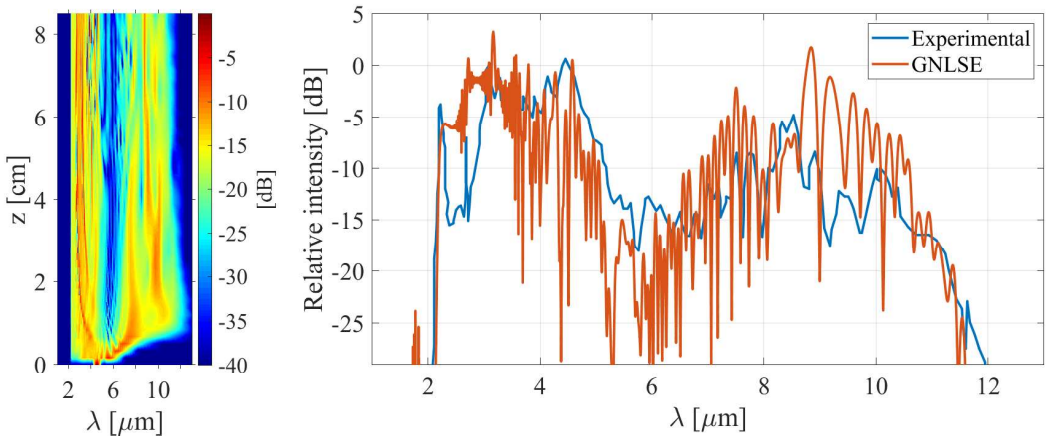

(a)

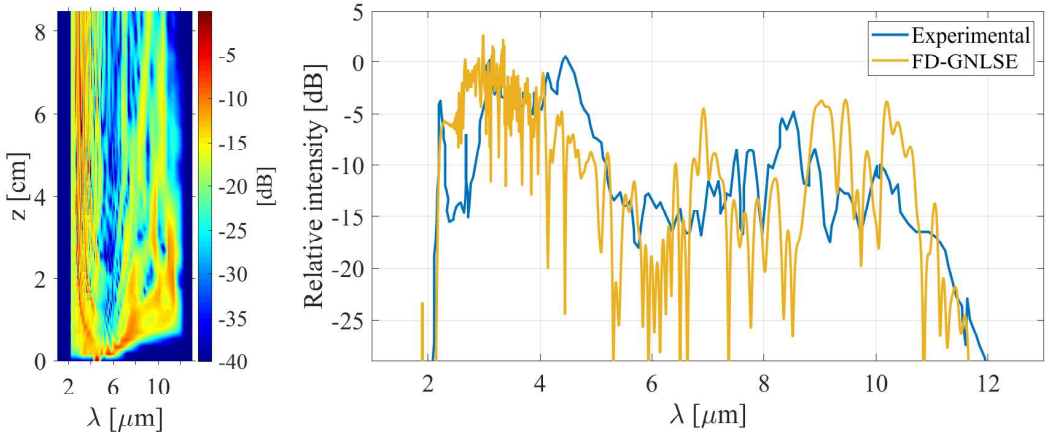

(b)

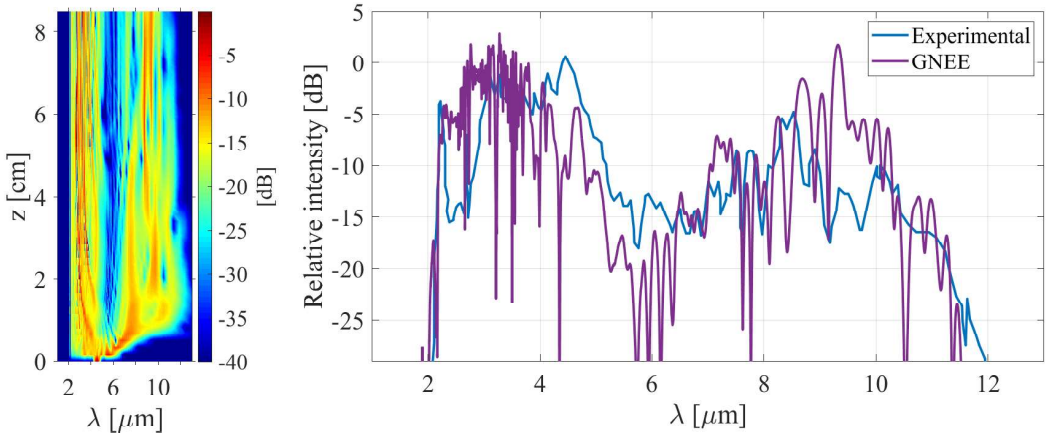

(c)

Figure 5.5: Numerical results for the GNLSE (a), the FD-GNLSE (b), and the GNEE (c) with 692 kW experimental coupled peak power (simulated with 180 kW peak power). Spectral evolution is shown on the left and the output spectra are shown on the right.

Table 4: Numerical results with Nt= 2^{16}, P_0 = 180 kW

Model	GNLSE	FD-GNLSE	GNEE
R^2	0.36	0.34	0.31
$1/\phi_{max}$	100	200	200
CPU time [s]	216	1444	790

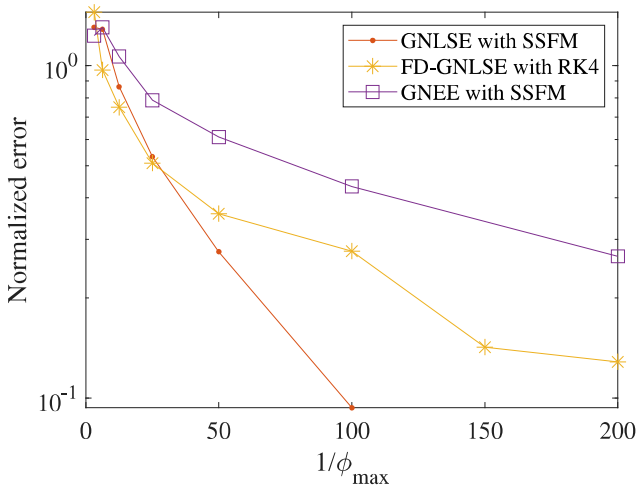

Figure 5.6: Convergence analysis for the three numerical methods with 180 kW (simulated) peak power

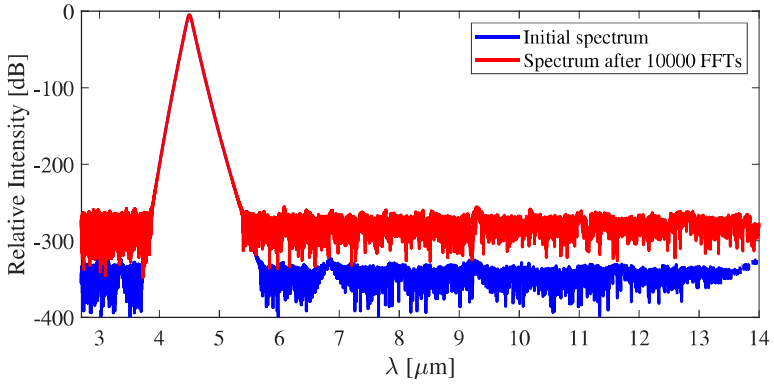

Figure 5.7: Numerical noise accumulation through the FFT operations.

5.2 Example 2: Near-Infrared SC Generation with a PCF

In this example, simulations are carried out with the experimental results reported in reference [54]. In their experiment, Klimczak *et al.* use a dispersion-engineered PCF made of F2 glass and high-energy pulses to generate SC in the 1 to 2.5 μm region in the all-normal-dispersion regime. The experimental conditions for the pump are shown in table 5:

Table 5: Experimental pump parameters from [54]

Pump Parameter	P_0 [MW] (before coupling lens)	T_{FWHM} [fs]	λ_0 [μm]
Value	37	60	2.16

The fiber used in this experiment is a hexagonal lattice PCF with a core of 2.46 μm. A scanning electron microscope image of the fiber facet is shown in figure 5.8.

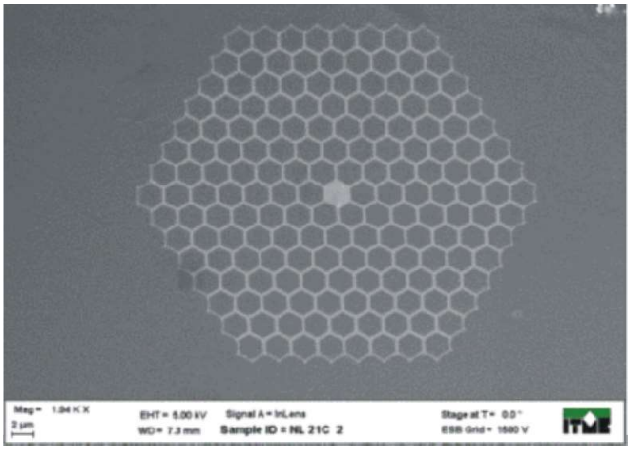

Figure 5.8: scanning electron microscope image of the PCF used in [54].

The dispersion curve of the fiber is shown in figure 5.9 (a). The ZDW is located at 2.82 μm. Figure 5.9 (b) shows the wavelength dependence of the effective mode area and the resulting nonlinear parameter. The value for $n_2 = 2.9 \cdot 10^{-20}$ m^{2}W^{-1} is taken from [55] and is considered constant over the total bandwidth. This fiber is a good example of strong wavelength dependence of effective area and its effect on nonlinearity. It is clear from figure 5.9 (b) that the shock term approximation (dotted line) is not quite sufficient to model the

full wavelength dependence of γ in this case. It is therefore expected that the FD-GNLSE is more suitable to simulate pulse propagation in this fiber. Other fiber parameters are shown in table 6. Raman scattering is neglected in the simulations because most of the spectral broadening occurs on the blue-shifted side and its effects are expected to be suppressed by SPM and wave-breaking [54]. The fiber losses considered in the simulations are shown in figure 5.10.

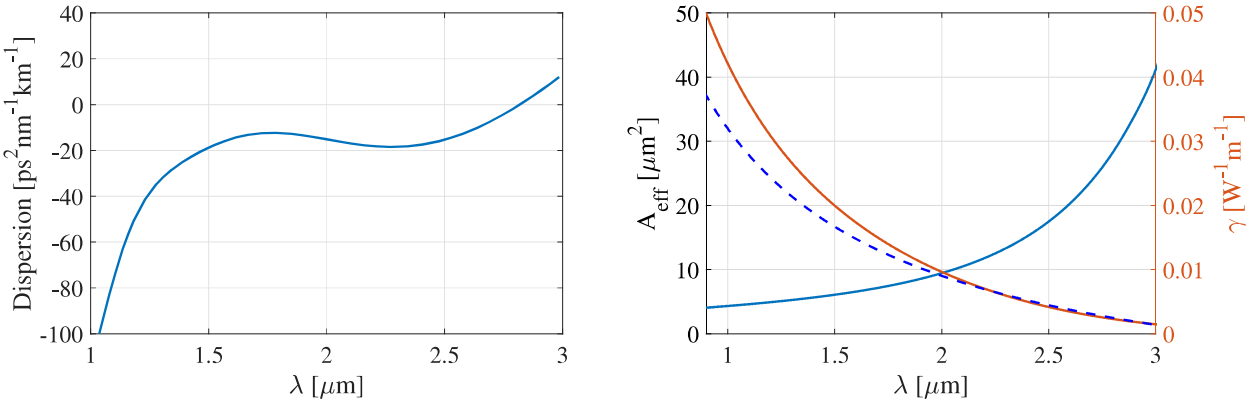

(a) (b)

Figure 5.9: (a) Dispersion curve of the F2 glass PCF with a ZDW of 2.82 μm. (b) Effective mode area (blue) from [54], nonlinear parameter (orange), and approximation of the nonlinear parameter with a corrected shock term: $\gamma \approx \gamma_0 + \gamma_0\tau_0\Omega$ (dotted line).

Table 6: Parameters for the F2 glass PCF

Parameter	L [cm]	n_2 [m^2/W]	A$_{\text{eff}}(\lambda_0)$ [μm^2]	γ_0 [km^{-1}W^{-1}]	f_R	τ_1 [fs]	τ_2 [fs]
Value	30	$2.9{\cdot}10^{-20}$	11.5	7.6	0	-	-

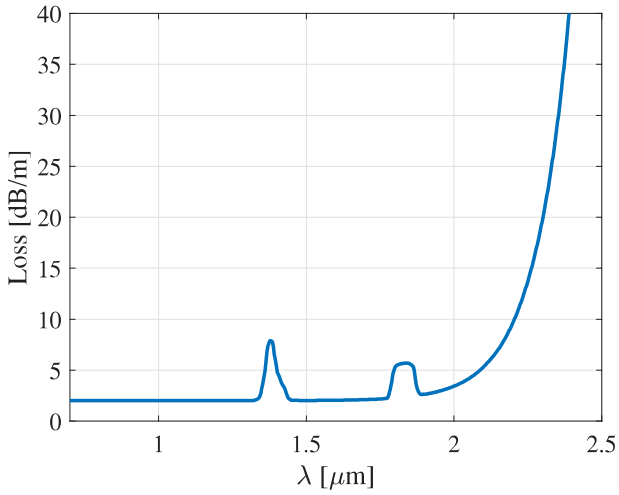

Figure 5.10: Fiber losses considered in the simulations for the F2 glass PCF.

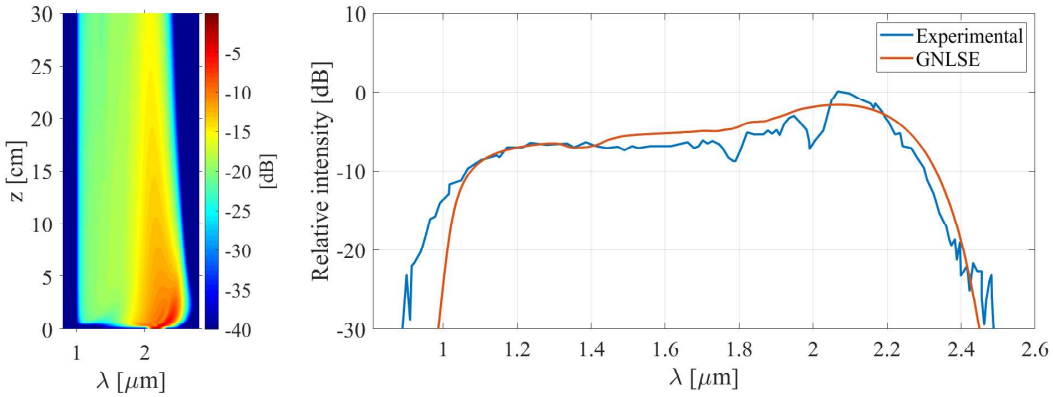

(a)

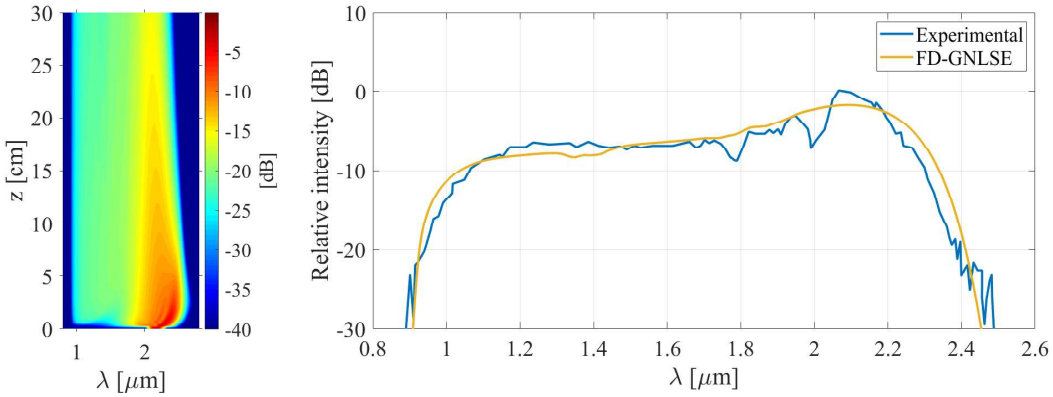

(b)

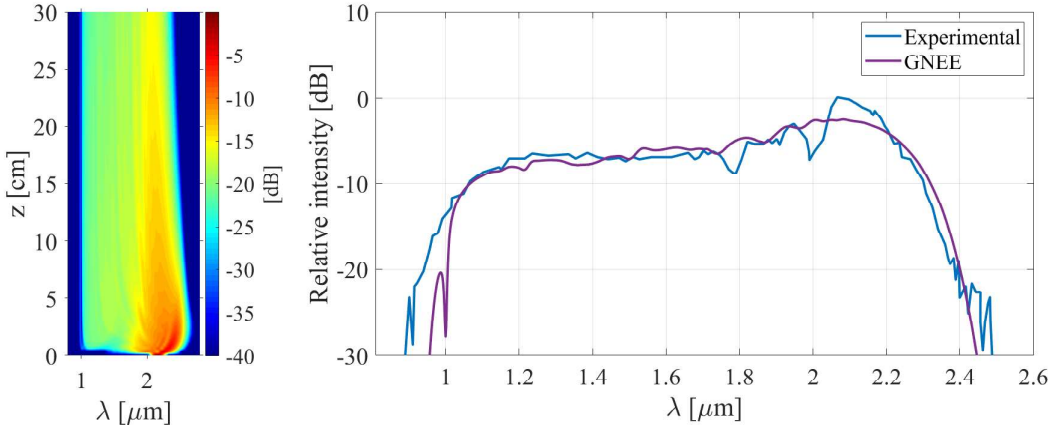

(c)

Figure 5.11: Numerical results for the GNLSE (a), the FD-GNLSE (b), and the GNEE (c) with 250 kW peak power (simulated); comparison with the experimental output spectrum. Spectral evolution is shown on the left and the output spectra are shown on the right.

The simulation results are shown in Figure 5.11. Qualitatively, it is clear that the FD-

GNLSE simulation provides a better fit to the experimental spectrum, especially on the blue-shifted edge of the SC. This is expected, because the FD-GNLSE accurately models higher nonlinearity at blue-shifted wavelengths, which pushes the blue-shifted edge of the SC further than with the GNLSE. In the case of the GNEE (figure 5.11 (c)), harmonic generation does not play a significant role in this experiment. As mentioned before, most of the spectral broadening occurs on the blue-shifted side due to SPM and wave-breaking, while the red-shifted broadening is limited by significant transmission losses above 2.5 μm. In terms of goodness of fit, the FD-GNLSE clearly exhibits better performance with its high R^2 of 0.84. The convergence analysis is shown in figure 5.12 and reveals that the GNLSE with the SSFM still has the fastest convergence rate in this case. This is again explained by the fewer FFTs per iteration of the SSFM algorithm and the higher sensitivity to numerical noise of the FD-GNLSE and GNEE.

This is a clear example of a case where the fundamental mode of the fiber exhibits very large frequency dependence of effective area and where the shock term approximation in the GNLSE starts to break down. For this type of experimental conditions, it is clear from the results that the FD-GNLSE is the better suited pulse propagation model.

Table 7: Numerical results with `Nt` $= 2^{15}$, $P_0 = 250$ kW

Model	GNLSE	FD-GNLSE	GNEE
R^2	0.40	0.84	0.69
$1/\phi_{\max}$	50	100	200
CPU time [s]	10	62	80

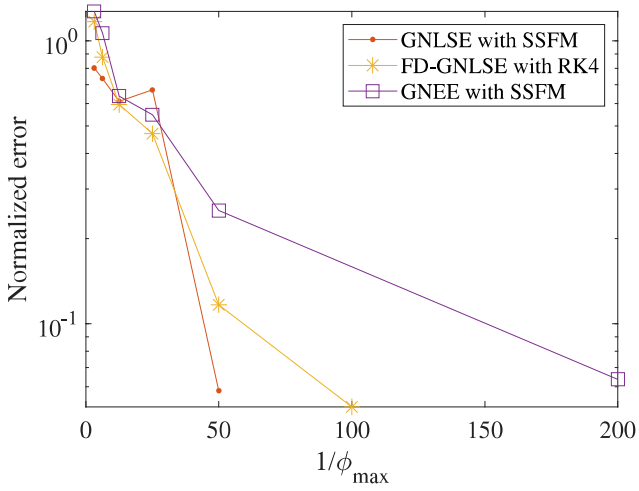

Figure 5.12: Convergence analysis for the three numerical methods with 250 kW (simulated) peak power

5.3 Example 3: THG with Near-Infrared Pumping

In this third example, simulations are carried out with the experimental conditions reported in reference [56]. In their paper, Kibler *et al.* report on the generation of non-phase-matched single mode THG in a highly nonlinear fiber made of Fluorine-doped silica. The pump lies in the anomalous dispersion regime of the fiber, at 1560 nm. Experimental parameters for the pump are shown in table 8:

Table 8: Experimental pump parameters from [56]

Pump Parameter	P_0 [kW]	T_{FWHM} [fs]	λ_0 [μm]
Value	16	90	1.56

The highly nonlinear fiber used in this experiment is a commercially available fiber from OFS Danemark [57]. Its core is made of Fluorine-doped silica, which produces a high index contrast with the pure silica cladding and ensures tight modal confinement for higher nonlinearity. The dispersion curve of the fiber is shown in figure 5.13 (a), the ZDW is located at 1410 nm. Figure 5.13 (b) shows the nonlinear parameter $\gamma(\lambda)$. The nonlinear index is

$n_2 = 2.7 \cdot 10^{-20}$ $\mathrm{m^2W^{-1}}$ and is considered constant in the simulations. For this fiber, the wavelength dependence of effective mode area is not specified. It is thus considered constant at 11.6 $\mu\mathrm{m}^2$ (from [56]) in the simulations. As a consequence, the shock term is exact in modeling the frequency dependence of γ, which is simply linear with ω. This can be seen in figure 5.13 (b). The GNLSE and the FD-GNLSE are therefore expected to yield the same output spectrum in this example. The other fiber parameters used in the simulations are presented in table 9. The Raman parameters for non-doped fused silica [2] are used as an approximation, and losses are neglected.

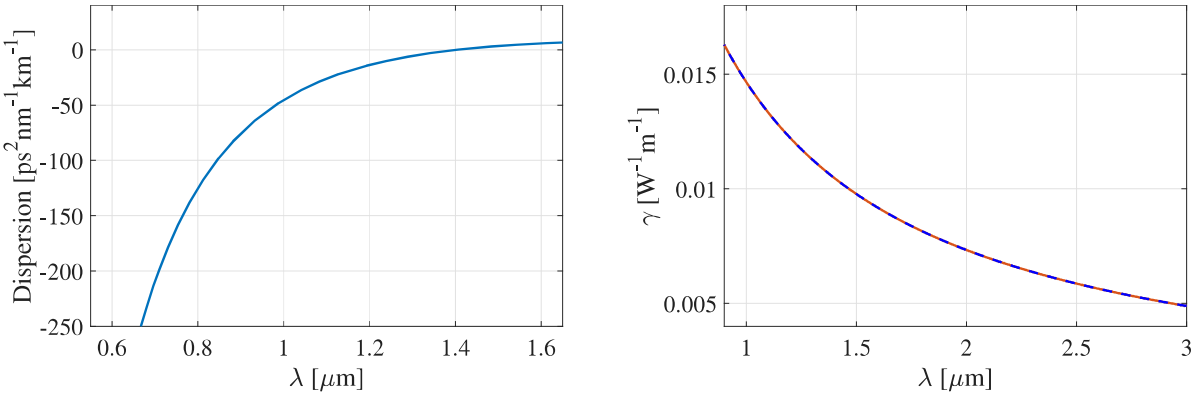

Figure 5.13: (a) Dispersion curve of the highly nonlinear fiber with a ZDW of 1410 nm. (b) Nonlinear parameter (orange) and shock term: $\gamma \approx \gamma_0 + \gamma_0\tau_0\Omega$ (dotted line). In this case, A_{eff} is considered constant, so the shock term is exact in modeling the frequency dependence of γ.

Table 9: Parameters for the highly nonlinear fiber

Parameter	L [cm]	n_2 [$\mathrm{m^2/W}$]	$\mathrm{A_{eff}}(\lambda_0)$ [$\mu\mathrm{m}^2$]	γ_0 [$\mathrm{km^{-1}W^{-1}}$]	f_R	τ_1 [fs]	τ_2 [fs]
Value	4.5	$2.7{\cdot}10^{-20}$	11.6	9.4	0.18	12.2	32

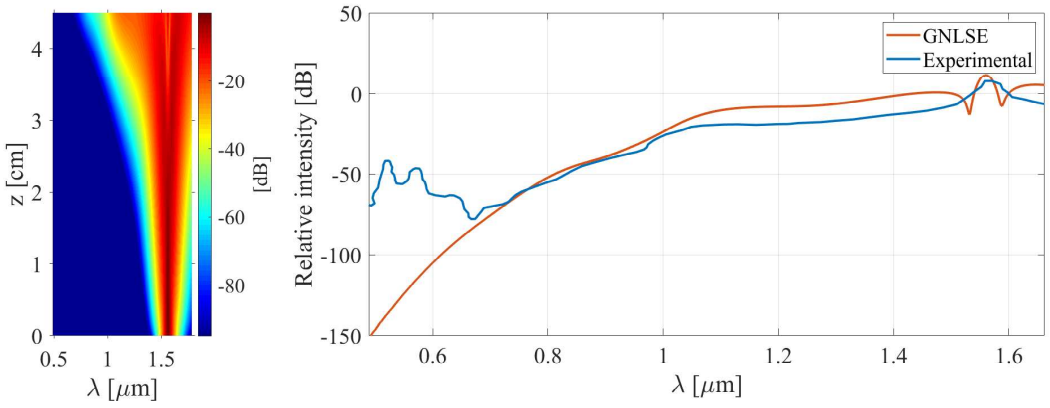

(a)

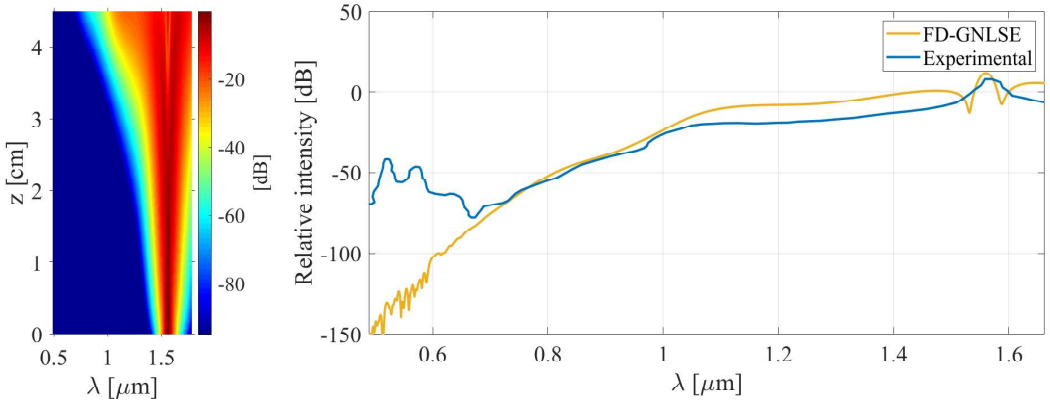

(b)

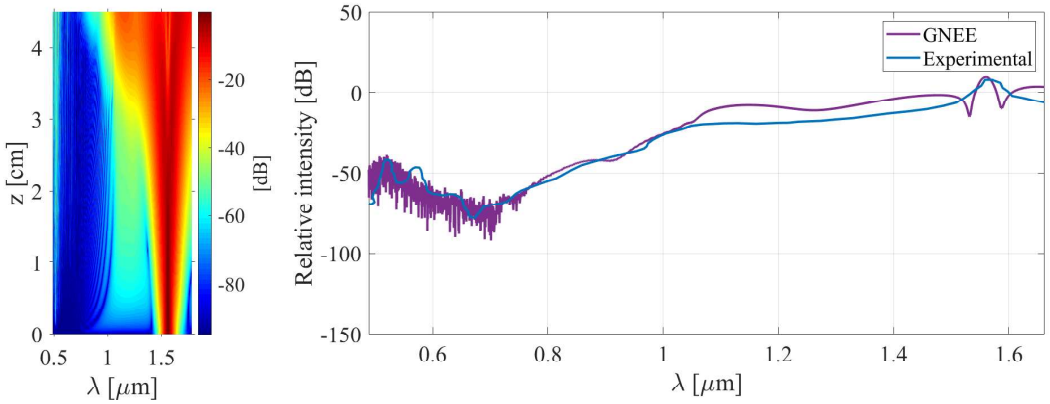

(c)

Figure 5.14: Numerical results for the GNLSE (a), the FD-GNLSE (b), and the GNEE (c) with 12 kW peak power, comparison with the experimental output spectrum with THG around 520 nm. Spectral evolution is shown on the left and the output spectra are shown on the right.

The simulation results for 4.5 cm of propagation with 12 kW are shown in figure 5.14. As expected, the GNLSE (a) and the FD-GNLSE (b) yield the same result down to the -100 dB point, where numerical noise becomes more important in the FD-GNLSE spectrum. This is again explained by the higher number of FFT operations per step in the FD-GNLSE algoritm. Both the GNLSE and FD-GNLSE fail to replicate the experimental THG peak around 520 nm. On the other hand, the GNEE (figure [56] (c)) does replicate the 520 nm THG peak fairly precisely. According to Kibler *et al.*, the second peak around 575 nm seen in the experimental spectrum is thought to be the result of spectral broadening of the pump and pump-THG group velocity mismatch. This peak is not reproduced in simulations. Rapid spectral modulations can be seen around the THG peak in the simulated GNEE spectrum. This is most likely due to THG amplification of numerical noise and the very fine spectral resolution at shorter wavelengths. The quantitative performance analysis is presented in table 10. As expected, the goodness of fit parameter R^2 is low for the GNLSE and FD-GNLSE, and high for the GNEE at 0.89. In terms of convergence, figure 5.15 shows that all three simulations reached the convergence criterion of 10^{-1} with fairly coarse step sizes. However, it was found that this convergence criterion is not sufficient for this particular simulation, because spectral dynamics down to -100 dB are modeled. In other words, spectral dynamics at -50 dB and below have a negligible contribution to the global simulation error (equation 4.40) and therefore may not converge even if an error of 10^{-1} is reached. A more qualitative criterion is used for convergence in these simulations, where the maximal nonlinear phase shift $\phi_{\max}$ is reduced until no change in spectral dynamics are noticeable.

Results for this simulation show the pertinence of the GNEE model when harmonics generation are observed in experiments. The GNEE is the only one of the three models to accurately model THG at 520 nm. Extremely fine step size are required to model the spectral dynamics below -50 dB, but convergence can still be achieved with reasonable computing time.

Table 10: Numerical results with $\mathtt{Nt} = 2^{15}$, $P_0 = 12$ kW

Model	GNLSE	FD-GNLSE	GNEE
R^2	0.22	0.22	0.89
$1/\phi_{\max}$	100	200	1500
CPU time [s]	5	37	195

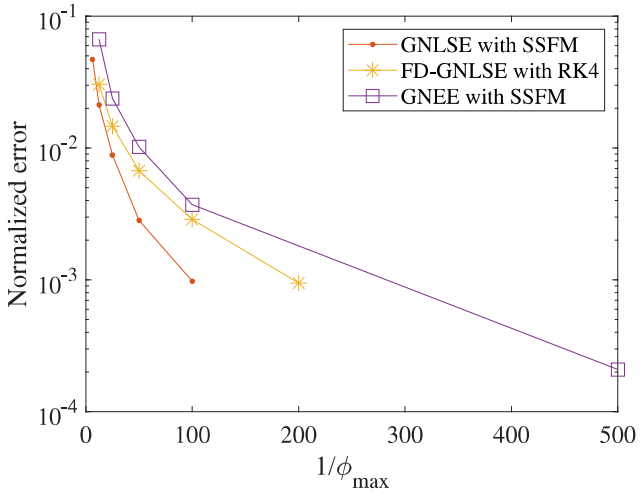

Figure 5.15: Convergence analysis for the three numerical methods with 12 kW (simulated) peak power

5.4 Example 4: Visible to Near-Infrared SC with Tapered Silica Fibers

In this example, numerical simulations are carried out with the experimental conditions from reference [34]. In their work, Birks *et al.* use fiber tapers drawn from commercially available SMF-28 fiber to generate SC spanning the 400 to 1600 nm region. The pump lies in the anomalous dispersion regime of the silica microwire at 850 nm. This is a typical example of SC generation by soliton fission and dispersive waves. Table 11 shows the measured pump parameters. Input pulse durations ranging from 200 to 500 fs were measured. In the simulations, 200 fs pulses are considered.

Table 11: Experimental pump parameters from [34]

Pump Parameter	P_0 [kW]	T_{FWHM} [fs]	λ_0 [nm]
Value	17	200 - 500	850

The fiber taper is drawn from SMF-28 silica fiber to a taper waist of 1.8 μm. Along the taper waist, the initial SMF-28 core is negligible in size and the mode is guided by the high-index contrast between silica and air, which ensures tight modal confinement and high nonlinearity. The fiber taper is schematized in figure 5.16.

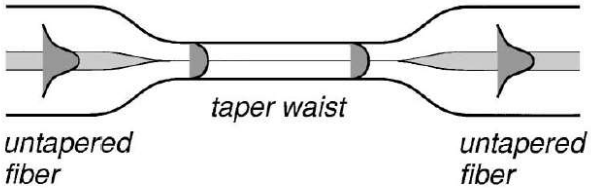

Figure 5.16: Diagram of the mode confinement along the taper 90 mm taper waist, taken from [34]

The dispersion curve of the 1.8 μm taper is shown in figure 5.17 (a). It is calculated by solving the characteristic equation for a step-index fiber with a silica core and an infinite air *cladding*. The ZDW is located at 688 nm, which puts the pump in the strong-anomalous dispersion regime. The effective mode area of the fundamental mode is calculated in the same way and is shown in figure 5.17 (b). With a constant $n_2 = 2.7 \cdot 10^{-20}$ for silica [2], the resulting nonlinear parameter is shown in orange in figure 5.17 (b). In this case, the corrected shock term approximation (shown with the dotted line) is sufficient to model the full frequency dependence of A_{eff}. The Raman parameters for fused silica are taken from [2] and are presented in table 12 with the other fiber parameters. Losses are neglected in the simulations.

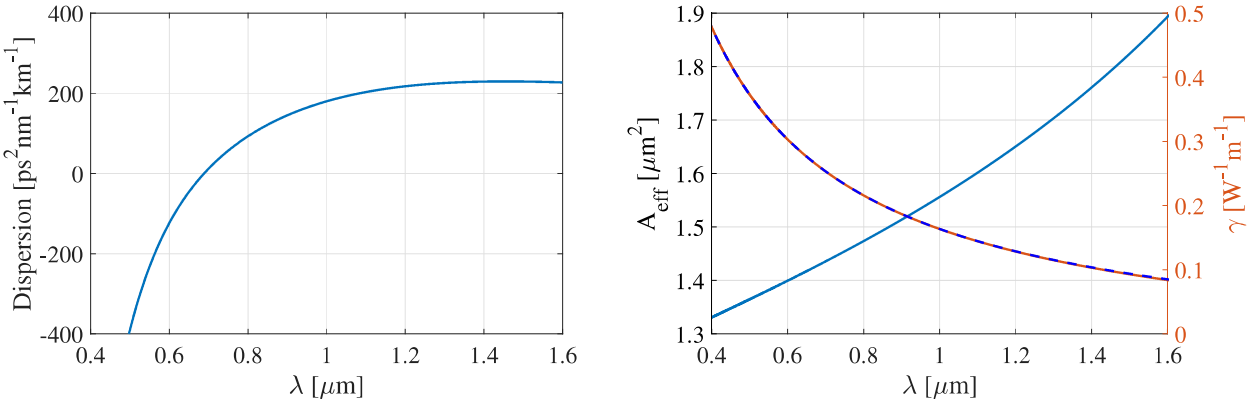

(a) (b)

Figure 5.17: (a) Calculated dispersion curve of the fiber taper with a ZDW of 688 nm. (b) Calculated effective mode area (blue), nonlinear parameter (orange) and shock term: $\gamma \approx \gamma_0 + \gamma_0\tau_0\Omega$ (dotted line).

Table 12: Parameters for the silica fiber taper

Parameter	L [cm]	n_2 [m^2/W]	$A_{eff}(\lambda_0)$ [μm^2]	γ_0 [km^{-1}W^{-1}]	f_R	τ_1 [fs]	τ_2 [fs]
Value	9	$2.7{\cdot}10^{-20}$	1.49	200	0.18	12.2	32

The simulation results and experimental output spectrum are shown in figure 5.19. All three models reproduce the soliton and dispersive wave dynamics with fidelity. The dispersive wave accumulation peak around 400 nm and the spectral dip around the ZDW of 688 nm are well reproduced. Soliton red-shifting dynamics are also relatively well reproduced. The difference between simulated spectra and the experimental spectrum on the long wavelength side is explained by the fact that soliton fission is sensitive to noise, peak power, and pulse duration [58]. Therefore, the difference between the exact experimental conditions and the simulation produce a different set of red-shifted fundamental soliton after the fission. The soliton fission phenomenon is clearly seen in the temporal profile evolution shown in figure 5.18. In the simulations, a peak power of 14 kW is used. This corresponds to a soliton number $N \approx 23$. The fission of the high-order soliton begins after 1 cm of propagation in the fiber taper. After the fission, individual fundamental red-shifted solitons are seen to drift in time at different rates; their group velocity differ because they are centered at different wavelengths.

In the same way, the acceleration of their temporal drift is the temporal manifestation of their continuous red shift from RIFS. The lower intensity (<20 dB) dispersive waves are also seen drifting from the initial pulse center.

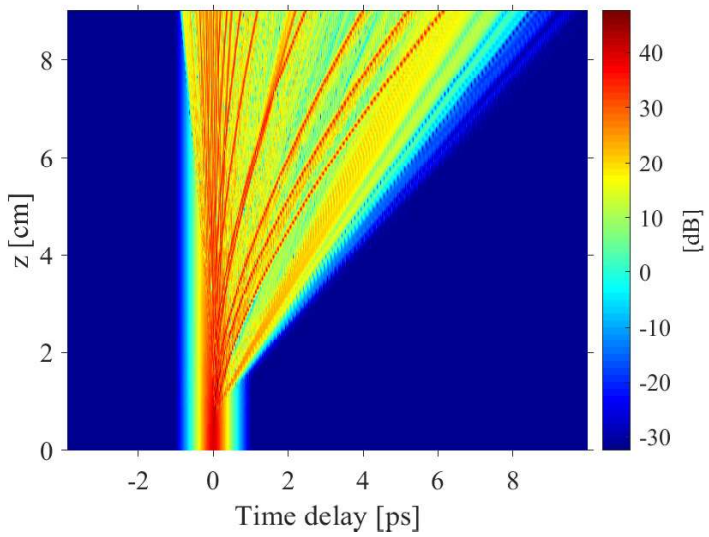

Figure 5.18: Temporal profile evolution along the tapered fiber, simulated with the GNLSE.

The quantitative performance analysis for the three models is presented in table 13. In terms of goodness of fit, all three models have similar performances, with the GNEE being slightly lower. The real differentiating factor is the convergence rate, shown in figure 5.20. In this example, the FD-GNLSE solved with the interaction-picture RK4 method converges much faster. This advantage in performance is presumably due to the way the stiff dispersive term is treated in a more mathematically exact way with the change of variable in the interaction picture method. This seems to have a significant effect in this example because dispersion is very high ($D = 122$ ps^{2}nm^{-1}km^{-1} at the pump wavelength). The GNEE is also solved with the interaction-picture RK4 method for this example, and it converges faster than the SSFM as a result.

While all three models are accurate enough for this example in terms of the physical mechanisms they encompass, the FD-GNLSE interaction-picture RK4 method has a clear advantage in terms of convergence rate and computing time.

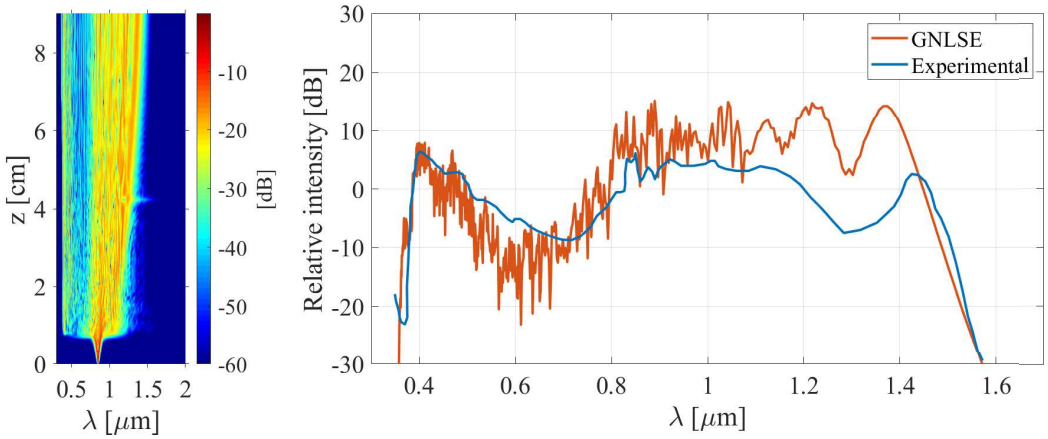

(a)

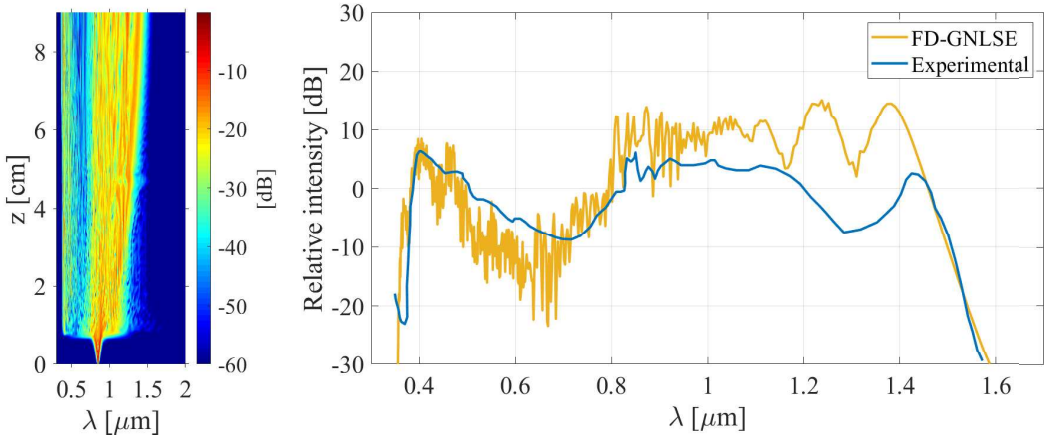

(b)

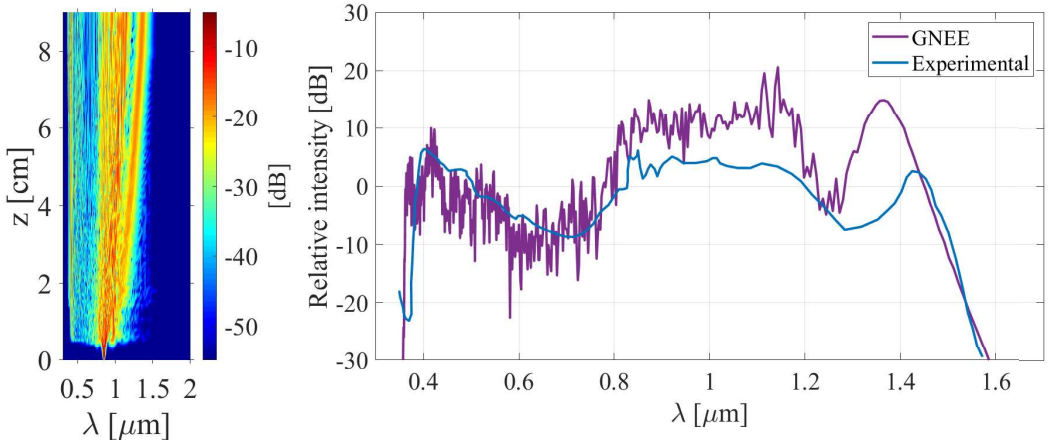

(c)

Figure 5.19: Numerical results for the GNLSE (a), the FD-GNLSE (b), and the GNEE (c) with 14 kW peak power, comparison with the experimental output spectrum. Spectral evolution is shown on the left and the output spectra are shown on the right.

Table 13: Numerical results with `Nt` $= 2^{15}$, $P_0 = 14$ kW

Model	GNLSE	FD-GNLSE	GNEE
R^2	0.48	0.42	0.34
$1/\phi_{\max}$	200	50	150
CPU time [s]	370	150	1834

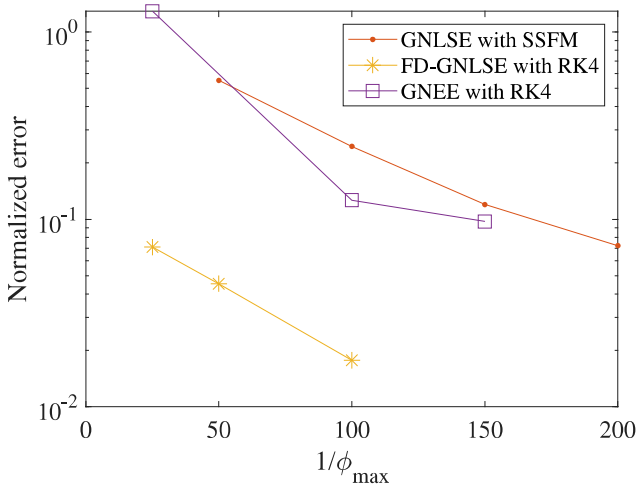

Figure 5.20: Convergence analysis for the three numerical methods with 14 kW (simulated) peak power

5.5 Discussion

Through the four examples presented here, it is shown that the *enhanced* versions of the GNLSE, namely the FD-GNLSE and the GNEE, are useful to model pulse propagation in specific experimental conditions, but that the GNLSE is sufficient in most cases.

Example 1 is a typical example of SC generation with a chalcogenide-based fiber. Other examples can be found in [3], [64], and [59]. In these experiments, the high nonlinearity of the chalcogenide glass generally produces a high-bandwidth mid-infrared SC through a chaotic mix of SPM, four-wave mixing, RIFS, and dispersive waves. Since the transmission

window of chalcogenide is limited to around 2 μm on the sort-wavelength side, THG dynamics likely do not occur or are heavily suppressed by the chaotic mix of nonlinear effects. As shown in the selected example, the GNEE therefore does not provide any advantages in these cases. Moreover, since the dispersion of γ is generally well modeled with the corrected shock term, the FD-GNLSE also does not add significant accuracy in terms of physics modeling.

Example 2 is chosen specifically for the large wavelength dependence of effective area. This is a rare case where the corrected shock term is not sufficient to model the full dispersion of γ. In this situation, the FD-GNLSE, which implicitly includes the full frequency-dependence of γ, has a clear advantage in terms of modeling.

In example 3, a specific case of non-phase matched single-mode THG is studied. The GNEE is the only model that includes THG dynamics and is therefore the most suitable of the three models in this case. However, these experimental conditions are not typical. THG in fibers is generally achieved via inter-modal phase matching of higher-order modes, as shown in [60]. Nonetheless, Kibler *et al.* [25] argue in their paper that the GNEE could be useful to model SC extending to the deep UV with near-IR pumping. To show this, they simulate SC generation in a 600 nm silica nanowire pumped by a 50 fs, 500 kW peak power pulse centered at 1060 nm. Their results, shown in figure 5.21, confirm the pertinence of their model for the simulation of extreme blue-shifted spectral broadening.

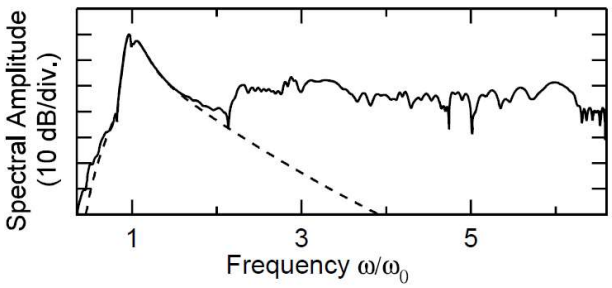

Figure 5.21: SC generation in a fused silica nanowire modelled using the GNEE (solid line), and without THG (dashed line), taken from [25].

Example 4 is a typical example of SC generation via soliton fission, RIFS an dispersive waves. Other examples can be found in [35], [37]. THG dynamics generally do not come into play in these cases, therefore the GNEE has no significant advantage, as shown in the results for example 4. Unless a speciality fiber with large effective mode area dispersion is used, the GNLSE with the corrected shock term is sufficient.

In the next chapter, it is also shown that the GNLSE with the corrected shock term is adequate for two other typical fibers: a ZBLAN step-index fiber and a chalcogenide glass PCF.

Chapter 6: Practical Implementation for a Cascaded Fiber System

This chapter presents the work I accomplished during my internship at the Femto-ST institute in France as part of my Masters degree. Under the supervision of Thibaut Sylvestre in Femto-ST's nonlinear optics group, and in collaboration with the company *Selenoptics*, I conducted numerical simulations for the analysis and optimization of a mid-infrared SC source prototype. In this work, the GNLSE is used for all simulations.

6.1 Introduction and Motivation

Mid-infrared SC sources in the 2 to 20 μm molecular fingerprint region are in demand for a wide range of applications including optical coherence tomography, remote sensing, molecular spectroscopy, and frequency metrology ([1],[28]). The spectral coverage of practical mid-infrared SC sources is often limited by the availability of suitable mid-infrared pump lasers and the transmission windows of mid-infrared optical fibers. In this work, we numerically investigate SC generation in a cascaded fiber system pumped with a commercially available 500 ps fiber laser in the telecommunication window. This cascaded fiber system was experimentally investigated by *Selenoptics* and *Le Verre Fluoré* companies, and was shown to generate a flat broadband mid-infrared SC from 2 to 10 μm. Their experimental work paves the way for cheaper, practical, and robust broadband SC sources in the mid-infrared. The aim of this numerical study is therefore to provide insight over the physical mechanisms at play in their system to shed light on possible optimizations. We first expose the details of the experimental cascaded fiber system with the physical parameters and the models used for each component, and we discuss the experimental results measured by *Selenoptics*. Then, the numerical results are discussed and compared to the experimental results. The conclusion presents the recommendations proposed to *Selenoptics* to optimize their cascaded system based on the simulation results.

6.2 *Selenoptic*'s Experimental Setup

The experimental cascaded fiber system setup developed by *Selenoptics* is schematized in figure 6.1. It consists of a pump source, three different fibers, and a window filter, all of which are commercially available. The pump laser is an Erbium-doped fiber laser centered at 1550.6 nm producing 460 ps pulses at a repetition rate of 90 kHz with an average power of 750 mW. This translates to a pump peak power of about 18 kW. A length of 20 cm of single mode SMF-28 silica fiber is directly pigtailed to the fiber laser output. The SMF-28 fiber end is butt-coupled to the second fiber, which is a step-index ZBLAN fiber of 25 m length from the company Le Verre Fluoré. Between the ZBLAN fiber and the third fiber, there is a Germanium window filter which acts as a low-pass filter to avoid optical damage and two-photon absorption from short wavelengths in the final fiber segment. The last fiber segment consists of 9 m of chalcogenide glass PCF. A detailed overview of the linear and nonlinear parameters of each fiber is presented in the subsequent sections. The output spectra are measured with a Fourier-transform infrared (FTIR) spectrometer. The measured spectra are presented in the next subsection.

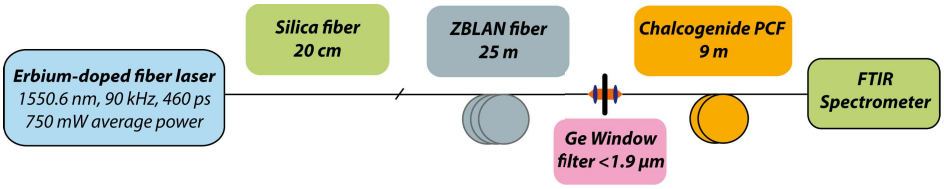

Figure 6.1: Experimental cascaded fiber setup from *Selenoptics* for mid-infrared SC generation, taken from [59].

6.3 Experimental Results

Selenoptics provided experimental data for the spectra measured at three key points in the cascaded fiber setup. The first spectrum, shown in figure 6.2 (blue curve), is measured directly at the output of the ZBLAN fiber, before the filter. The second spectrum, shown in figure 6.2 (red curve), is measured after the filter. This is the spectrum injected into the chalcogenide fiber.

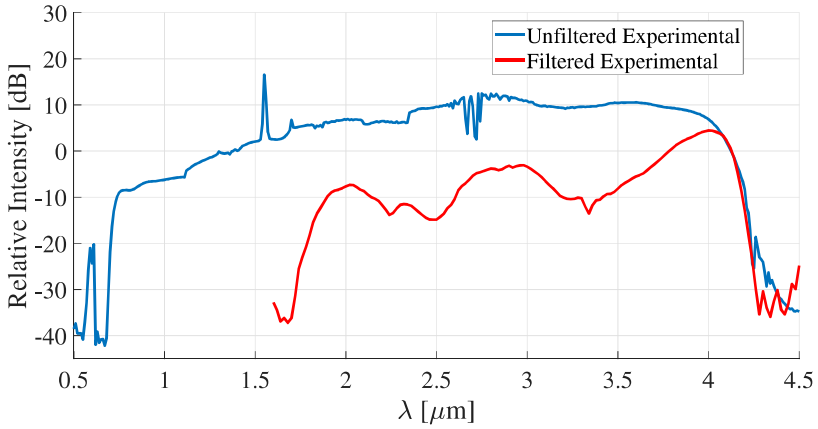

Figure 6.2: Experimental spectra measured at the output of the ZBLAN fiber (blue) and after the filter (red).

The final spectrum measured at the output of the chalcogenide fiber is shown in figure 6.3. Each of the measured spectra show a decrease in spectral intensity for shorter wavelengths and significant modulations in intensity (especially from 2 to 4 μm). The simulations show that those are not entirely a result of actual SC dynamics, but presumably artefacts from the wavelength sensitivity of the spectrometers used for measurement. The measured average power at the output is 16 mW, which corresponds to roughly 2% of the pump's average power (750 mW). Significant losses occur in the cascaded system, mainly from the free-space optics between the ZBLAN fiber and the chalcogenide fiber: Fresnel reflections and coupling losses from mode field diameter mismatch, cleaving imperfections, and alignment imperfections. Table 14 shows an estimation of the losses at each stage of the system.

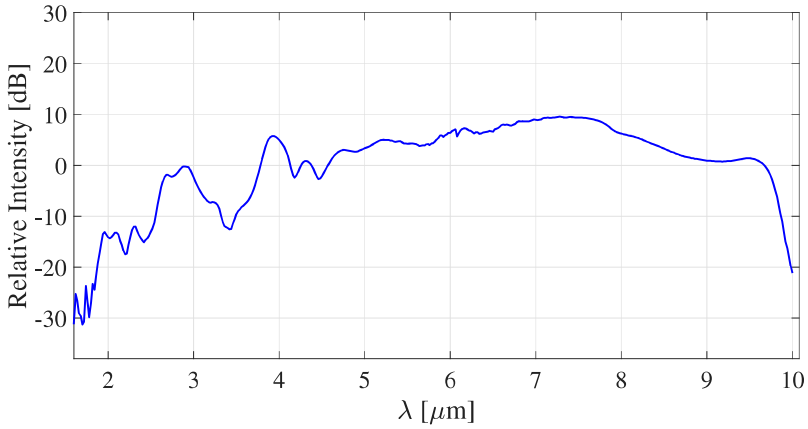

Figure 6.3: Experimental spectra measured at the output of the chalcogenide PCF.

Table 14: Optical losses in the cascaded fiber system

Stage	Pump-SMF connexion	20 cm SMF	SMF-ZBLAN connexion	25 m ZBLAN	Free-space optics	Coupling to chalcogenide fiber	9 m chalco-genide
Loss	0.2 dB	0 dB	1 dB	See Fig. 6.7	5 dB	3-6 dB	See Fig. 6.11

6.4 Fiber Characteristics

6.4.1 Fiber 1 : SMF-28

The first fiber segment consists of a length of 20 cm of standard SMF28 step-index silica fiber. The nonlinear parameters for fused silica fiber are taken from [2] and presented in table 15:

Table 15: Nonlinear parameters for the SMF28 fiber

Parameter	L (cm)	n_2 (m^2/W)	A_{eff} (μm^2)	γ_0 ($km^{-1}W^{-1}$)	f_R	τ_1 (fs)	τ_2 (fs)
Value	20	$2.7{\cdot}10^{-20}$	85	1.3	0.18	12.2	32

The wavelength dependence of A_{eff} and n_2 is negligible over the spectrum bandwidth along this first fiber segment. The dispersion characteristics of SMF-28 are modeled using a Taylor

series expansion. The second and third-order dispersion terms are sufficient considering the initial pulse is long and does not undergo significant change in the 20 cm of SMF28 fiber. The following values are used: $\beta_2 = -21.4 \cdot 10^{-27}$ s^2/m, $\beta_3 = 0.12 \cdot 10^{-39}$ s^3/m (from [2]). The resulting dispersion curve is shown in figure 6.4. The 1550 nm pump is in the anomalous dispersion regime. Optical losses are neglected for this fiber segment.

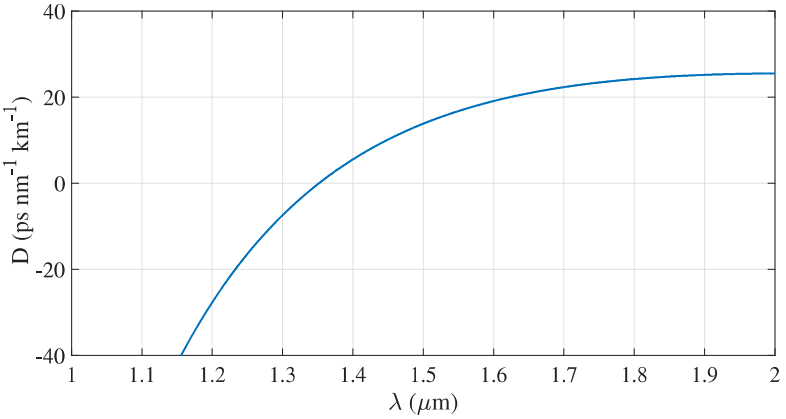

Figure 6.4: Dispersion curve used for numerical modeling of the SMF-28 fiber.

6.4.2 Fiber 2: ZBLAN Step-Index Fiber

The second fiber consists of a length of 25 m of commercially available step-index ZBLAN fiber from Le Verre Fluoré [61]. The core diameter is 8.5 μm and the cladding diameter is 125 μm. The dispersion curve is presented in figure 6.5 (a). *Selenoptics* provided dispersion values from 1.2 to 2.2 μm. To obtain the dispersion of the fiber over the full bandwidth, the characteristic equation for a step-index fiber with the wavelength-dependent core and cladding indices is solved. The ZDW is 1525 nm, therefore the 1550 nm pump is in the slightly-anomalous dispersion regime. Figure 6.5 (b) shows the calculated effective mode area and resulting nonlinear parameter with $n_2 = 2.1 \cdot 10^{-20}$m^2/W taken from [18].

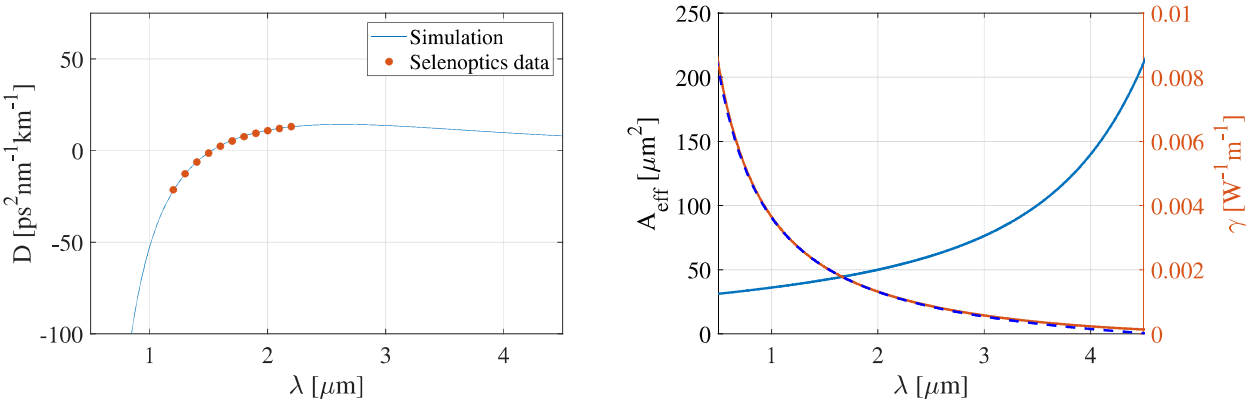

(a) (b)

Figure 6.5: (a) Calculated dispersion curve of the ZBLAN fiber with a ZDW of 1525 nm. (b) Calculated effective mode area (blue), nonlinear parameter (orange) and shock term: $\gamma \approx \gamma_0 + \gamma_0\tau_0\Omega$ (dotted line).

The nonlinear parameters for the ZBLAN fiber are presented in table 16:

Table 16: Nonlinear parameters for the ZBLAN fiber

Parameter	L (cm)	n_2 (cm^2/W)	$A_{eff}(\lambda_0)$ (μm^2)	γ_0 (km^{-1}W^{-1})	f_R
Value	2500	$2.1{\cdot}10^{-16}$	43	2	0.2

The wavelength dependence of the nonlinear index is neglected. The Raman response function h_R is obtained with the model presented in [18] and mentioned in section 2.2, where the measured Raman gain $g_R(\Omega)$ is approximated by a sum of two Gaussian functions, and the response function is extracted from the complex part of the Fourier transform:

$$h_R(T > 0) = C \cdot \int_0^\infty g_R(\Omega)\sin(\Omega T)\mathrm{d}\Omega \tag{6.1}$$

where C is a normalization constant chosen such that $\int_{-\infty}^{\infty} h_R(T)\mathrm{d}T = 1$. The following equation is used in the simulations to model $g_R(\Omega)$:

$$g_R(\Omega) = a_1 \exp\left(\frac{(\Omega/(2\pi) - \nu_1)^2}{2\omega_1^2}\right) + a_2 \exp\left(\frac{(\Omega/(2\pi) - \nu_2)^2}{2\omega_2^2}\right) \tag{6.2}$$

with $a_1 = 0.54 \cdot 10^{-11}$cm/W, $a_2 = 0.25 \cdot 10^{-11}$cm/W, $\nu_1 = 17.4$ THz, $\nu_2 = 12.4$ THz, $\omega_1 = 0.68$ THz, $\omega_2 = 3.5$ THz, from [18]. $g_R(\Omega)$ is plotted in figure 6.6. Here, the anti-Stokes absorption is neglected in the frequency-domain Raman response.

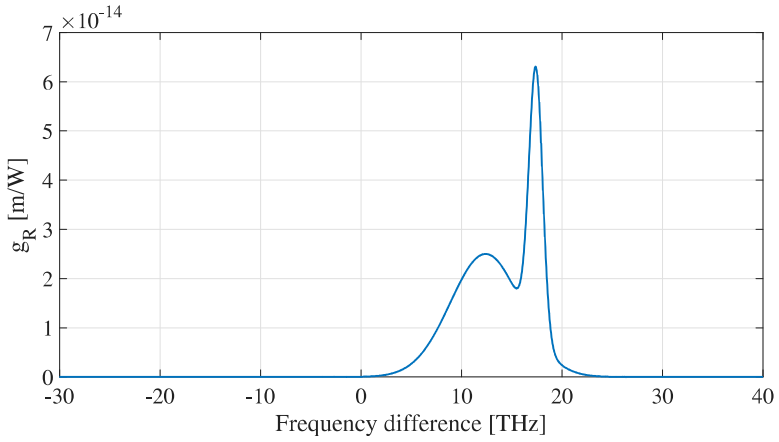

Figure 6.6: Numerical model for the Raman gain of the ZBLAN fiber.

Figure 6.7 show the optical losses for the ZBLAN fiber modeled after the data from Le Verre Fluoré. The transmission window limit of the ZBLAN fiber, which ends around 4.5 μm is the most important feature of the loss curve as it will ultimately limit spectral broadening.

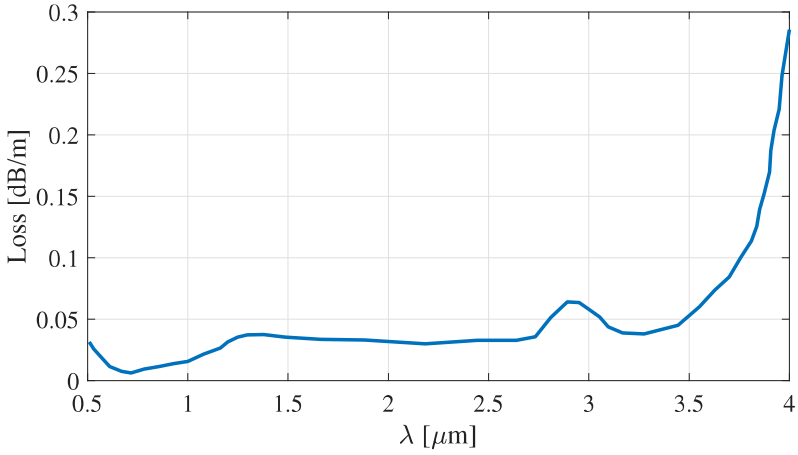

Figure 6.7: Optical losses for the ZBLAN fiber.

6.4.3 Window filter

The short-wavelength filtering of the ZBLAN fiber output is achieved experimentally with a combination of a germanium window filter (THORLABS WG91050-C9) and lenses with Ar anti-reflective coatings. This filtering system aims to cut all the energy below 2 μm in the ZBLAN fiber output spectrum to prevent two-photon absorption and optical damage in the chalcogenide fiber. The global transmission function of this filtering system is modeled with a supergaussian function of the following form:

$$T = \exp\left(- \left(\frac{\lambda - \Lambda_0}{\Delta\lambda} \right)^m \right) \tag{6.3}$$

The parameters Λ_0, m, and $\Delta\lambda$ are adjusted to obtain the best possible fit with the experimental spectrum measured after the filtering system (see figure 6.2). The following values are used: $\Lambda_0 = 11.87$ μm, $m = 80$, and $\Delta\lambda = 10$ μm. The resulting transmission function is plotted in the bandwidth of interest in figure 6.8.

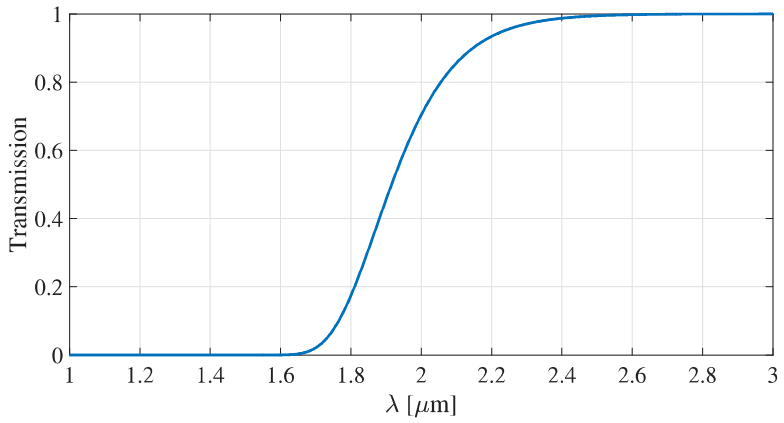

Figure 6.8: Modelization of the filter transmission.

6.4.4 Fiber 3: Chalcogenide PCF

The third fiber segment consists of a microstructured chalcogenide PCF from *Selenoptics*. It is made of $As_{38}Se_{62}$ glass, has a core diameter of 11.2 μm, a pitch of 7.11 μm, and an air-hole diameter of 3.23 μm. Figure 6.9 shows a cross section of the fiber with dimensions for the air hole structure.

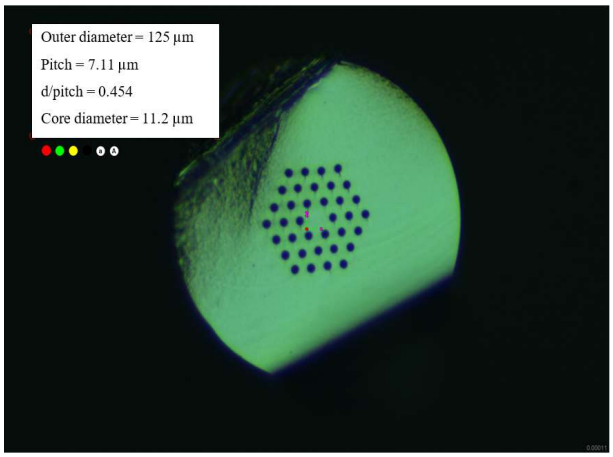

Figure 6.9: Cross section of the microstructured chalcogenide fiber.

The dispersion curve for the fundamental mode is calculated by the finite-element method using the COMSOL software with the wavelength dependent index and the dimensions provided by *Selenoptics*. The result is shown in figure 6.10 (a). The zero dispersion wavelength is 4.838 μm. The calculated effective mode area is shown in figure 6.10 (b) with the resulting nonlinear parameter (orange curve). A constant nonlinear index of $n_2 = 1.1 \cdot 10^{-17}\mathrm{m}^2/\mathrm{W}$ is assumed [1]. The corrected shock term approximation is sufficient in this case.

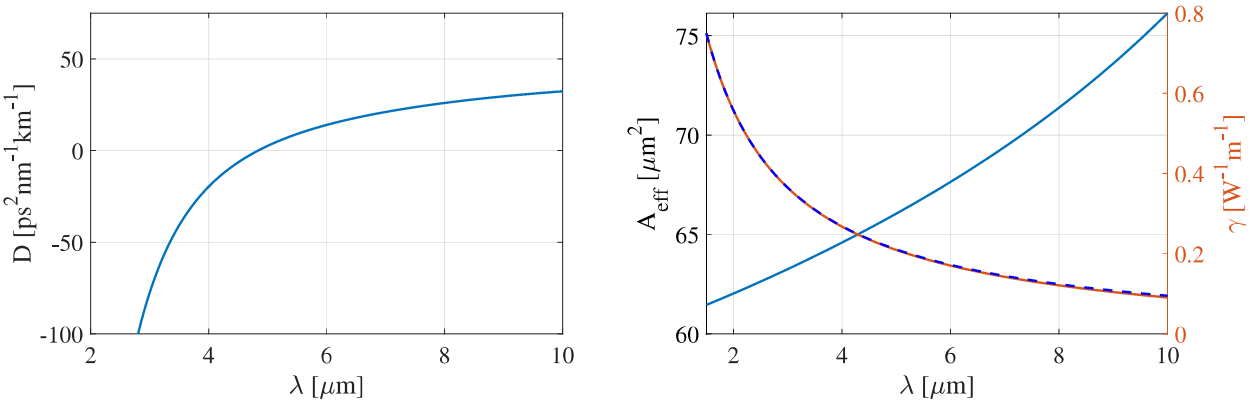

Figure 6.10: (a) Calculated dispersion curve of the chalcogenide PCF with a ZDW of 4838 nm. (b) Calculated effective mode area (blue), nonlinear parameter (orange) and shock term: $\gamma \approx \gamma_0 + \gamma_0\tau_0\Omega$ (dotted line).

The nonlinear properties of $As_{38}Se_{62}$ glass are approximated by the properties of As_2Se_3, which can be readily found in the literature. The following table shows the nonlinear parameters considered for this fiber:

Table 17: Nonlinear parameters for $As_{38}Se_{62}$ microstructured fiber

Parameter	L (cm)	n_2 (m^2/W)	$A_{eff}(\lambda_0)$ (μm^2)	γ_0 ($km^{-1}W^{-1}$)	f_R	τ_1 (fs)	τ_2 (fs)
Value	900	$1.1{\cdot}10^{-17}$	62	720	0.1	23.2	195

The Raman parameters are taken from [52]. This gives Raman gain peak centered around 6.9 THz with a linewidth of about 3.2 THz. Optical losses for the chalcogenide fiber (provided by *Selenoptics*) are shown in figure 6.11. The transmission window ends at around 10 μm, and there is an absorption peak around 4.6 μm due to the presence of Se-H chemical bounds in the glass.

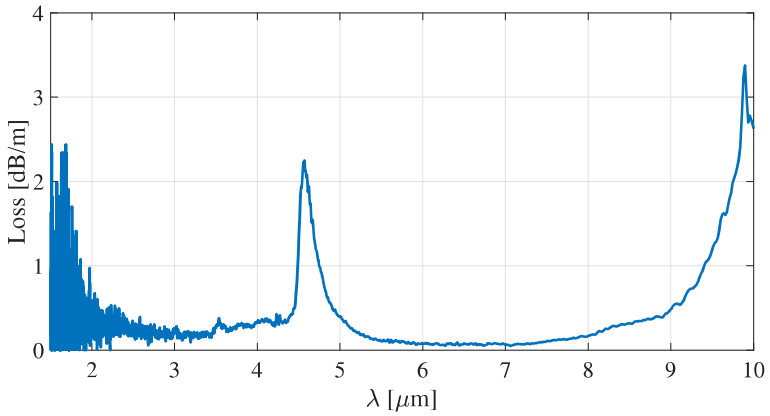

Figure 6.11: Measured optical losses for the chalcogenide PCF.

6.5 Simulation Results

The simulation results are now presented for the measured pulse duration of 460 ps and two shorter pulse durations of 200 and 50 ps. We aim to show that the quasi-CW SC mechanisms are still well reproduced with shorter pulse durations as to ultimately save computing time. Since the experimental pulse duration is long and the spectral broadening spans many octaves, the number of necessary discretization points is very large ($\texttt{Nt}{>}2^{19}$), which leads to

lengthy simulations. A peak power of 6 kW is chosen for the three pump pulses to get the best match with experimental results. As mentioned before, a lower peak power than the experimental peak power (18 kW) is used. This is due to the fact that the simulation model considers perfectly polarized and single-mode propagation. In experimental conditions, random polarization and multi-mode behavior is generally detrimental to spectral broadening mechanisms, hence the need for less power in simulations. Simulations are carried out for the three pump pulse durations in the SMF-28 fiber and the ZBLAN fiber. As expected from the theory of SC generation with quasi-CW pulses (see section 2.5), it is shown that the same mechanisms occur for the three different pump pulse durations, and that the experimental SC bandwidths at the output of the ZBLAN and chalcogenide fibers can be achieved with pump pulses as short as 50 ps. The SSFM algorithm requires high longitudinal precision in the chalcogenide fiber because of high nonlinearity ($\gamma_0 = 720$ km^{-1}W^{-1}). As a result, simulations for 200 ps and 460 ps pump pulses, which require at least $\texttt{Nt} = 2^{21}$ sample points, would require unreasonable computing times. Therefore, simulations in the chalcogenide fiber are only carried out with the intermediate ZBLAN results from the 50 ps pump pulse.

The spectral and temporal evolutions in this section are represented with color maps of relative intensity with a 40 dB range from blue to red. This means the maximum relative intensity will appear in deep red, and all points with intensities that are lower by 40 dB or more will appear in deep blue, as shown in figure 6.12.

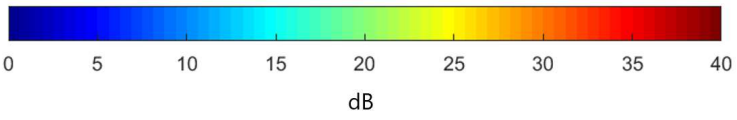

Figure 6.12: Color scale for time and spectral evolution maps.

6.5.1 Fiber 1: SMF-28

The simulation results for 20 cm of propagation in the SMF-28 fiber are shown in figure 6.13 for a 460 ps pulse. The pulse shape remains virtually unchanged throughout this fiber segment. The only notable feature is the apparition of MI sidebands in the spectrum around

1.51 and 1.59 μm, which correspond to the theoretical MI wavelength values derived from equation 3.6 (a more detailed view is shown in figure 6.15). They can be seen appearing on either side of the pump in the spectral evolution (figure 6.13 on the right). The results for the 200 and 50 ps pulses are identical: the pulse shape is unaffected and MI sidebands appear around the same wavelengths. The results from this simulation are taken as initial pulses for the ZBLAN fiber simulations. It is worth noting, however, that the simulations show this first fiber segment has little to no effect on the overall SC evolution in the ZBLAN and chalcogenide fibers.

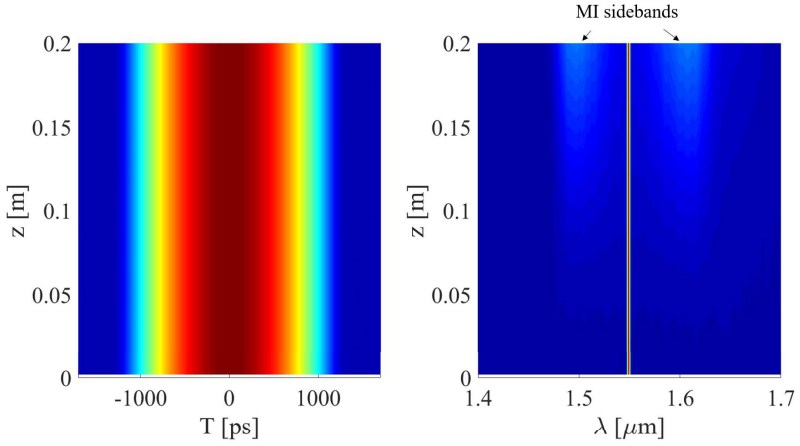

Figure 6.13: Temporal and spectral evolution in the SMF-28 fiber for a 460 ps pulse. 40 dB dynamic range (see figure 6.12).

6.5.2 Fiber 2: ZBLAN Fiber

The simulated spectral and temporal evolution in the ZBLAN fiber are shown in figure 6.14 for the three pulse lengths. On the right, the final spectrum after 25 m of propagation is compared to the experimental result. The break-up of the pulse into a train of solitons can be seen around 2 m. Beyond this point, the continuous RIFS of the solitons is clearly seen in the spectral evolution and in the temporal evolution as they gradually separate from the main pulse due to their dispersion increasing with the RIFS. Events of soliton collision can also be observed in the spectral evolution. They manifest themselves as sharp increases in the spectrum bandwidth on the long-wavelength side (e.g. around 16 m in the 50 ps spectral

evolution). Dispersive waves can be seen rapidly drifting away from the main pulse in the time evolution. In each of the three cases, the dispersive waves are not fully contained in the time window for the entire propagation length. Their time aliasing did not affect the overall SC dynamics and is suppressed with the post-processing of the plots.

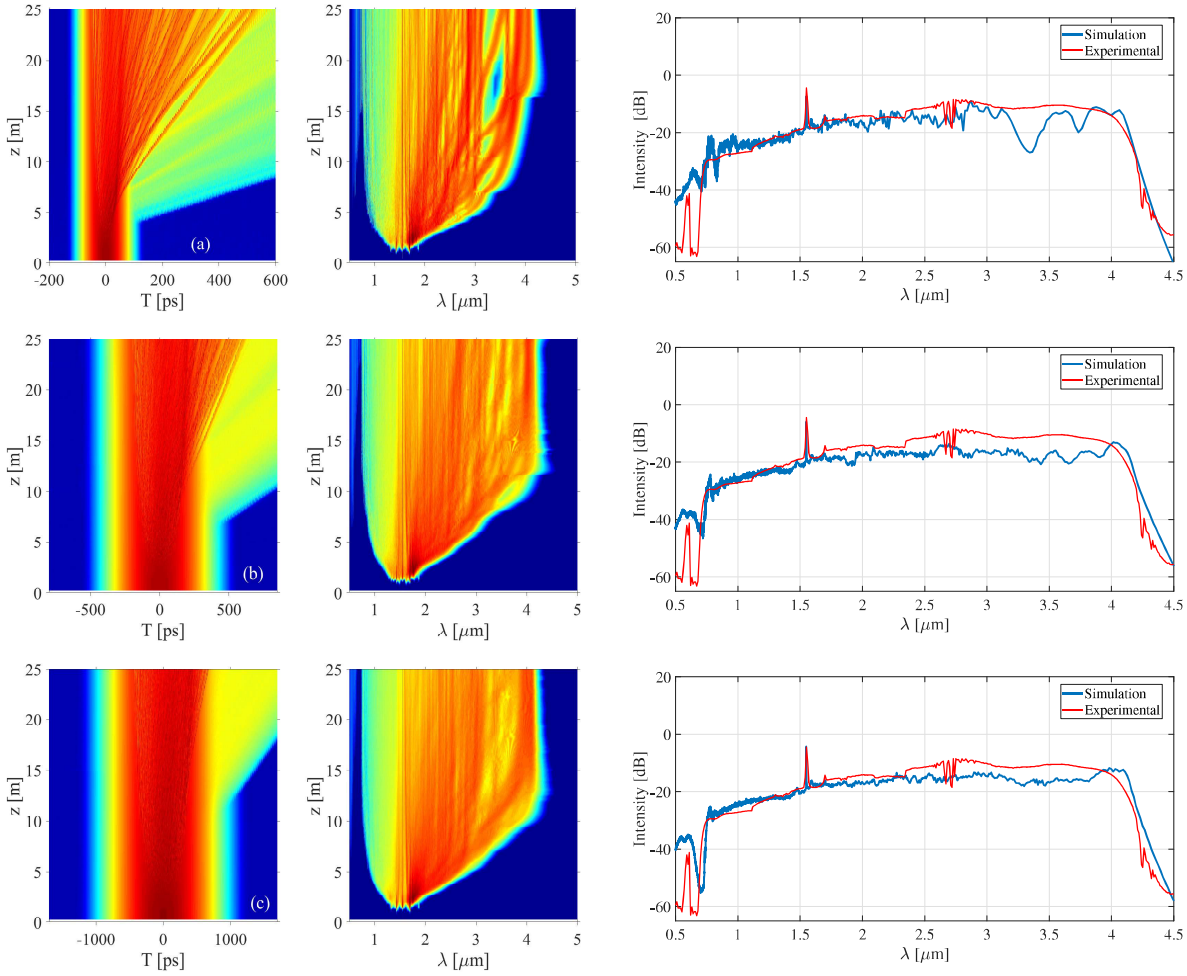

Figure 6.14: Spectral and time-domain evolution for the 50 ps (a), 200 ps (b), and 460 ps (c) pump pulse with the output spectra on the right. 40 dB dynamic range (see figure 6.12).

As expected from theory, the SC mechanisms in play are the same for the three pulse durations. Moreover, the final spectra for the three pulse lengths are nearly identical. This is due to the fact that the total bandwidth and soliton RIFS is only limited by the transmission window of the fiber (see figure 6.7) in the mid-infrared, which ends between 4 and 4.5 μm. In terms of bandwidth, all three pulse duration provide a nearly perfect match with

the experimental spectrum. However, the output spectrum becomes smoother as the pump pulse duration increases. This is due to the fact that a greater number of solitons are created from longer pulses, which leads to a more continuous range of values for total soliton RIFS.

From theory and simulation, it is confirmed that the time and spectral domain evolution of the 460 ps pulse is well approximated by the 50 ps pulse. Therefore, from now on, simulations are carried out only with the result from the 50 ps pump pulse to save computing time. To gain insight on the processes initiating SC generation in the ZBLAN fiber, figure 6.15 shows the details of the first 50 cm of spectral evolution. The strongest sidebands correspond to the MI-enabled Stokes and anti-Stokes Raman sidebands around 1.42 and 1.70 μm. Around 1.51 and 1.59 μm are the residual MI sidebands from the SMF-28 fiber. Very weak MI ZBLAN sidebands are visible around 1.39 and 1.755 μm. Each of the wavelength pairs given here and identified on the plot are calculated theoretically. The MI wavelengths are derived from equation 3.6, and the Raman wavelengths correspond to the peak of the ZBLAN Raman gain (figure 6.6), at 17.4 THz. As discussed in chapter 2.5, this gradual amplification of noise breaks up the pulse into a train of femtosecond pulses, as seen in figure 6.16. Figure 6.17 shows a zoom on three solitons from the pulse train. They have typical durations between 100 and 200 fs.

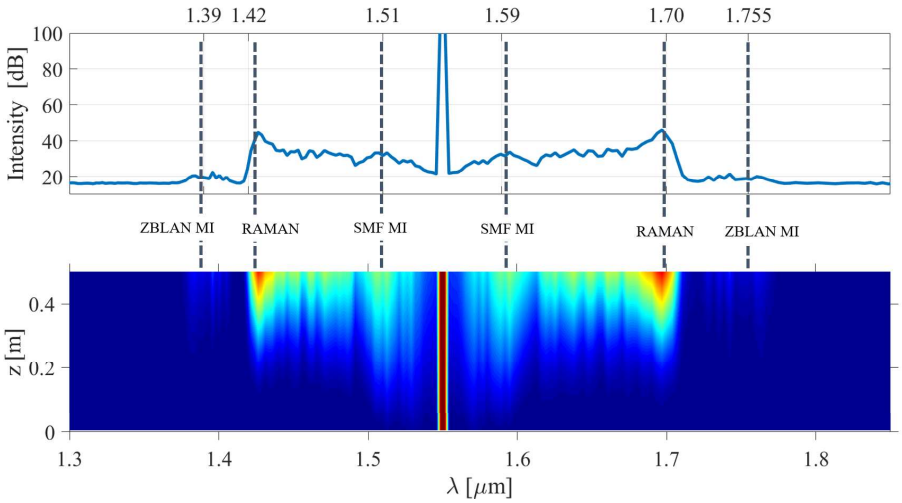

Figure 6.15: Initial spectral evolution in the ZBLAN fiber, 40 dB dynamic range (see figure 6.12). The wavelengths marked with the dotted lines correspond to the theoretical MI and Raman wavelengths calculated with equation 3.6 and the Raman gain peak at 17.4 THz respectively.

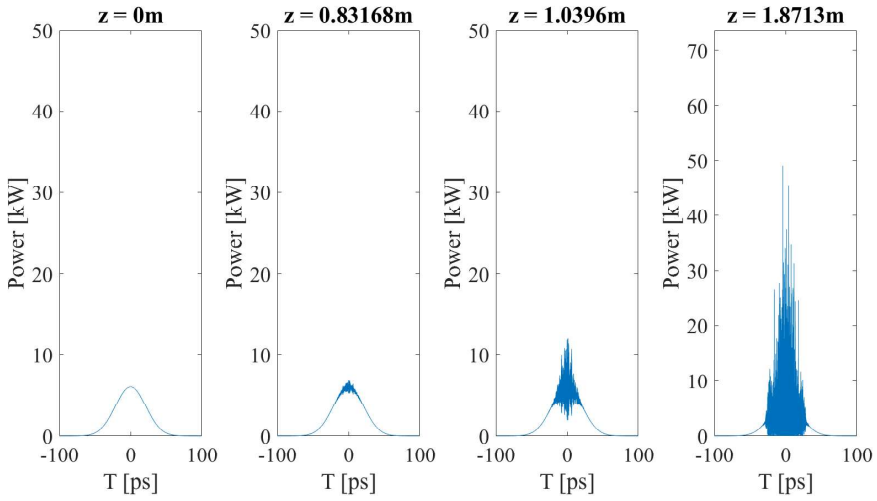

Figure 6.16: Initial temporal evolution in the ZBLAN fiber.

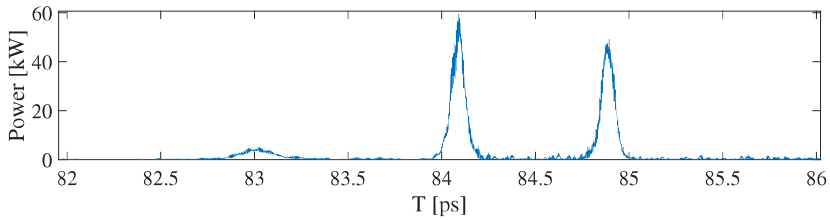

Figure 6.17: Typical solitons from the pulse train.

Figure 6.18 shows the filtered simulated spectrum (filtered with the transmission function of figure 6.8) compared with the experimental filtered spectrum. This is the spectrum injected in the chalcogenide fiber. The dynamics of the experimental spectrum are related to the measurement technique and not a consequence of actual SC dynamics.

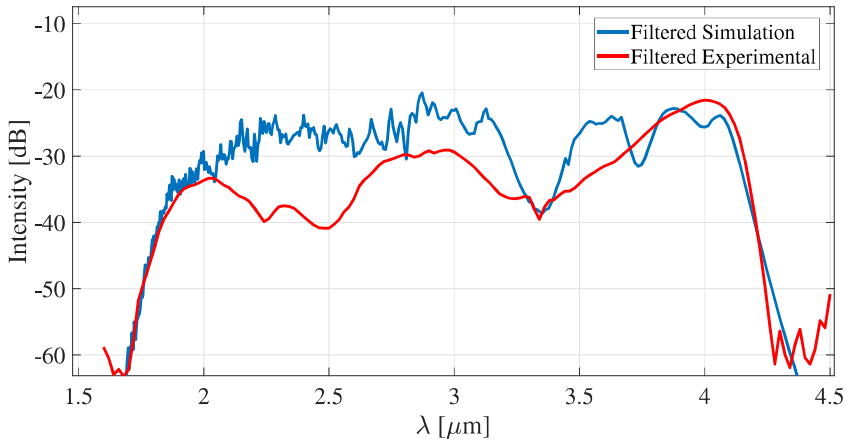

Figure 6.18: Filtered spectrum injected in the chalcogenide fiber.

6.5.3 Fiber 3: Chalcogenide PCF

The simulation result for the first 2 cm of propagation in the chalcogenide fiber are shown in figure 6.19. The injected spectrum from the filtered ZBLAN output lies entirely in the normal dispersion regime of the chalcogenide fiber which has its ZDW at 4.838 μm (marked by the dotted line). The initial spectral evolution shows that, from the train of thousands of pulses injected in the chalcogenide fiber, a fraction of them have a small enough width T_0 to drift through the zero-dispersion via RIFS (see equation 3.4). The pulses crossing the ZDW

evolve back into solitons and create an initial low-intensity continuum on the long-wavelength side through RIFS.

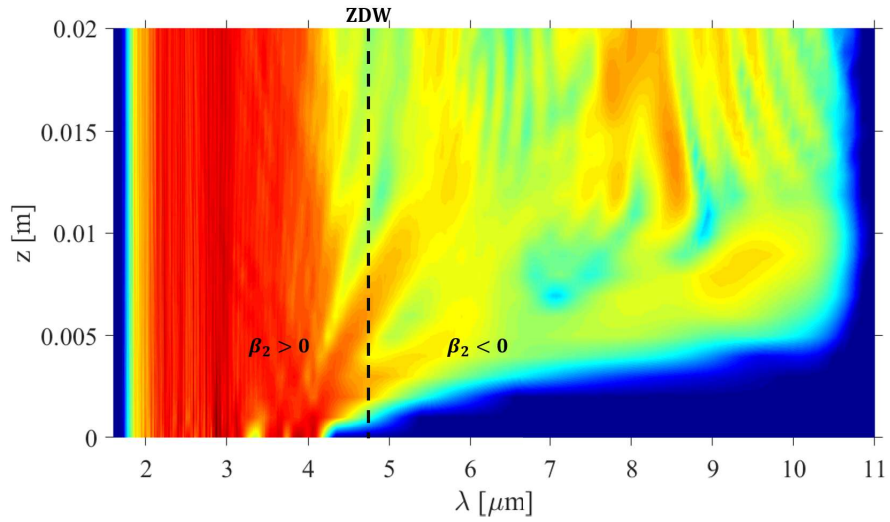

Figure 6.19: Initial spectral evolution in the chalcogenide PCF. 40 dB dynamic range (see figure 6.12).

The spectral evolution over the full 9 m of chalcogenide fiber is shown in figure 6.20. The top of the figure shows the final output spectrum compared to the experimental spectrum. In terms of spectral bandwidth, the numerical result matches nearly perfectly with the experimental measurement. As in the ZBLAN fiber, spectral broadening in the chalcogenide PCF is only limited by its transmission window.

The spectral evolution of figure 6.20 shows interesting SC dynamics. From 0 to 5 m, most of the energy remains in the normal dispersion regime ($\beta_2 > 0$). Energy rapidly accumulates at the limit of the transmission window (around 9.5 μm) from the pulses that initially crossed the ZDW. These solitons tend to accumulate around this wavelength as their RIFS is stopped by the limit of the transmission window. The effect of the absorption peak at around 4.6 μm (see figure 6.11) can be clearly seen on the low-energy continuum. From the beginning, the main train of pulses can be seen drifting (though RIFS) towards the ZDW. After 5 m most of the pulses remain *trapped* by the ZDW barrier and stop their frequency drift. From 5 m onward, a fraction of the pulses cross the ZDW barrier and start evolving as solitons on the

anomalous dispersion side ($\beta_2 < 0$). This gradually adds energy to the initial low-energy continuum via the RIFS of the solitons. The spectrum then evolves towards *thermalization*, where energy is equally distributed throughout the transmission bandwidth. The output is therefore a relatively flat spectrum from 2 to 9.7 μm.

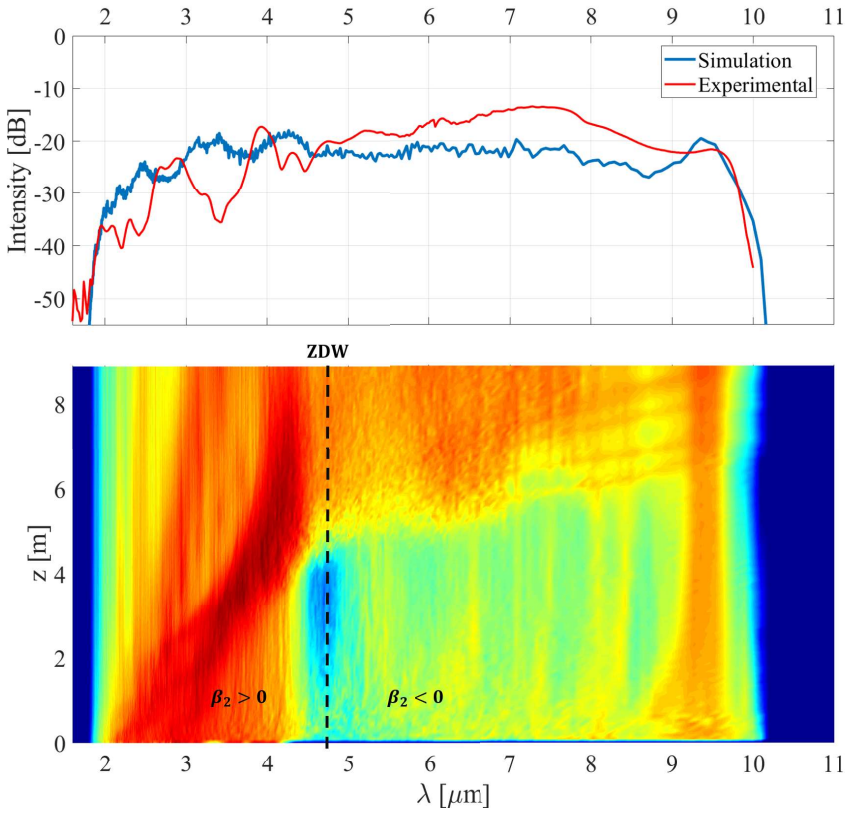

Figure 6.20: Full spectral evolution in the chalcogenide PCF with final output spectrum. 40 dB dynamic range (see figure 6.12).

6.5.4 Fiber 3: Alternative Chalcogenide PCF

In this subsection, simulation results for an alternative 3rd fiber in the cascaded system are presented. The chosen fiber was presented by Saghaei *et al.* [62] in 2015 as part of an experimental study on mid-infrared SC generation. It is microstructured with the same air-hole pattern as the one use experimentally by *Selenoptics*. Figure 6.21 shows a diagram of its cross-section. It is made of As_2Se_3 glass, which has similar nonlinear properties to $As_{38}Se_{62}$ glass. The main difference is its lower ZDW, which is at 3.81 μm. This is due to

the different dimensions of its air-hole structure: it has a core diameter of 7 μm, a pitch of 5 μm, and an air-hole diameter of 3 μm.

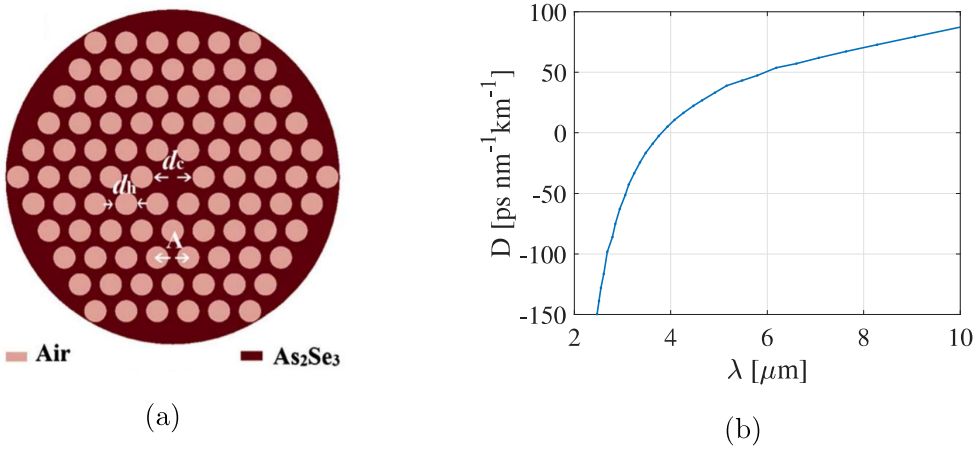

(a) (b)

Figure 6.21: (a) Cross-section of the alternative chalcogenide fiber (adapted from [62]). (b) Dispersion curve with a ZDW of 3.81 μm.

Figure 6.22 shows the spectral evolution over 1 cm of this alternative chalcogenide fiber. This short propagation distance allowed to carry out the simulation with the filtered ZBLAN spectrum from a 460 ps pump pulse. With the ZDW at 3.81 μm, a fraction of the filtered ZBLAN output spectrum is injected directly in the anomalous dispersion regime of this fiber (on the right of the dotted line in figure 6.22). This allows a great number of solitons to form directly without having to cross the ZDW barrier. Through RIFS, the solitons rapidly fill the transmission window with a relatively high-energy continuum. Therefore, by shifting the ZDW to 3.81 μm with this alternative chalcogenide fiber, the simulations show that an almost flat SC spanning the 2-10 μm window could be generated with only 1 cm of fiber.

The study of broadening dynamics in this fiber shows that, over the first centimeters of propagation, energy injected in the normal dispersion regime tends to stay concentrated on that side of the ZDW, and energy injected in the anomalous dispersion regime rapidly spreads to fill the transmission window. Therefore, shifting the ZDW further towards short wavelengths (with an even smaller core diameter) would help achieve an even flatter SC with only a few centimeters of fiber. This would reduce cost and the overall losses in the cascaded

system.

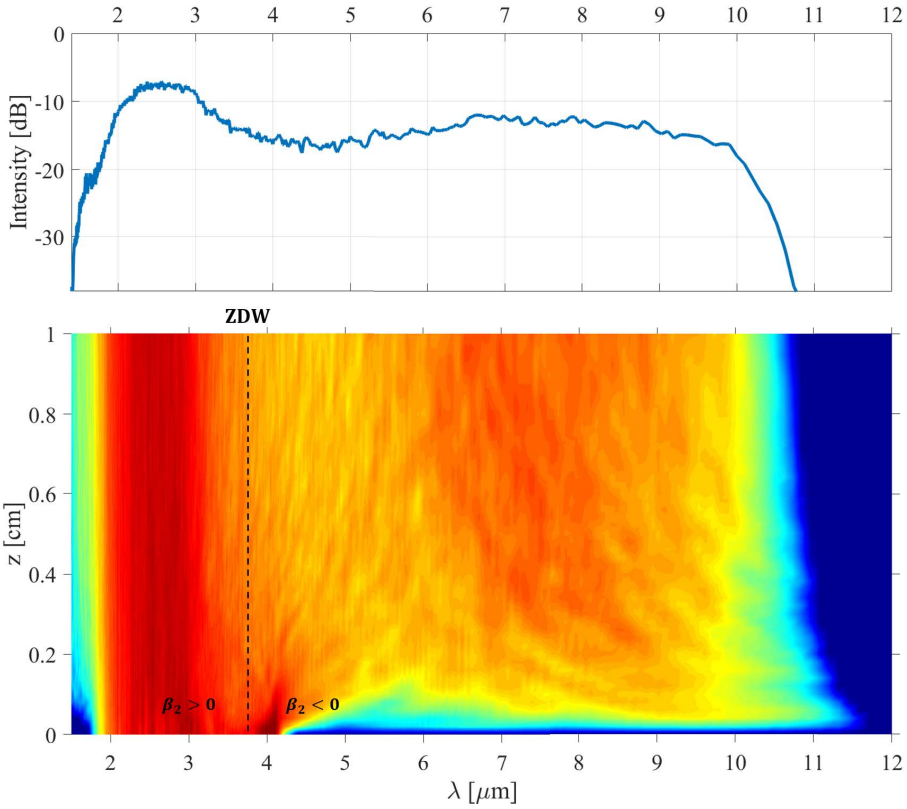

Figure 6.22: Spectral evolution in the 7 μm-core chalcogenide fiber. 40 dB dynamic range (see figure 6.12).

6.6 Recommendations

The simulations are consistent with the theory of quasi-CW SC generation. It is observed numerically that noise amplification through MI and Raman gain leads to the break-up of the pulse envelope into a chaotic train of solitons which broadens the spectrum through RIFS and dispersive waves. It is also confirmed that the same SC mechanisms take place for pump pulses as short as 50 ps. This allows to approximate 460 ps pulse evolution with a 50 ps pulse for greatly reduced computing time. In terms of bandwidth, the numerical results are nearly identical to the experimentally measured spectra, both at the output of the ZBLAN fiber and the chalcogenide fiber. The final output spectrum is a flat broadband SC from 2 to 10 μm. Further broadening is only limited by the transmission window of the chalcogenide

fiber.

Our main recommendation consists of using a chalcogenide microstructured fiber with a smaller core diameter as the third fiber of the cascaded system. This would shift its ZDW towards shorter wavelengths and, according to our simulations, allow to fill the desired window (from 2 to 10 μm) with a few centimeters of fiber.

Our second recommendation consists of exploring different options for the filtering system and to avoid free-space optics if possible. The free-space optics and the re-coupling to the chalcogenide fiber induce considerable losses in the system. An all-fiber filtering system, for example, could provide more robustness and less loss.

Finally, we also recommend exploring telluride-based fibers as a fourth fiber to add to the system. This would potentially allow to further broaden the spectrum and reach wavelengths beyond 10 μm [63].

Chapter 7: Conclusion

In this work, three waveguide pulse propagation models were investigated: the GNLSE, the FD-GNLSE, and the GNEE. The three models were used to simulated SC generation in four different examples from the experimental literature. The simulation results confirmed that the widely-used GNLSE model is sufficiently accurate to model most physical mechanisms involved in SC generation. However, the pertinence of the two other models was demonstrated through key examples. The FD-GNLSE proved useful in a case where the dispersion of γ was very strong in the fiber and the shock term in the GNLSE was not sufficient to approximate it, even with the effective area slope correction. The GNEE was shown to be useful in a case of non-phase-matched single-mode THG in a highly nonlinear fiber. Examples of deep-UV SC generation are also thought to be more accurately modeled through the GNEE. This could be investigated in future work along with cases of sub 10 fs pulses and sub-cycle dynamics. To allow for a more a more thorough performance comparison, a convergence analysis was carried out for each simulations in the four case study fibers. The results showed that the GNLSE solved with the SSFM has a performance advantage in terms of convergence rate for cases where spectral broadening is dominated by noise-seeded phenomena such as soliton fission and MI. This was explained by the lower number of noise-inducing discrete FFT operations in the GNLSE-SSFM algorithm. It was also shown in the tapered silica fiber case study that the FD-GNLSE solved with the RK4 method has a convergence rate advantage when high dispersion is involved.

The extent of the scope of the GNLSE was shown through a practical example of analysis and optimization of a SC source. In this work, GNLSE-based simulations were used to fully model a cascaded fiber SC source designed by the company *Selenoptics*. The simulation results allowed to make precise recommendations regarding their prototype: to consider a chalcogenide PCF with a smaller core for the third fiber, to explore different options for the filtering system, and to consider adding a fourth fiber made of telluride glass to potentially extend the SC deeper in the mid-infrared.

References

[1] Dudley, J. M., & Taylor, J. R. (Eds.). (2010). *Supercontinuum generation in optical fibers*. Cambridge University Press.

[2] Agrawal, G. P. (2012). *Nonlinear fiber optics* (5th edition), Academic Press.

[3] Hudson, D. D., Antipov, S., Li, L., Alamgir, I., Hu, T., El Amraoui, M., Messadeq, Y., Rochette, M., Jackson, S. & Fuerbach, A. (2017). Toward all-fiber supercontinuum spanning the mid-infrared. *Optica*, 4(10), 1163-1166.

[4] Al-Kadry, A., Li, L., El Amraoui, M., North, T., Messaddeq, Y., & Rochette, M. (2015). Broadband supercontinuum generation in all-normal dispersion chalcogenide microwires. *Optics letters*, 40(20), 4687-4690.

[5] Al-Kadry, A., El Amraoui, M., Messaddeq, Y., & Rochette, M. (2014). Two octaves mid-infrared supercontinuum generation in As 2 Se 3 microwires. *Optics Express*, 22(25), 31131-31137.

[6] Godin, T., Combes, Y., Ahmad, R., Rochette, M., Sylvestre, T., & Dudley, J. M. (2014). Far-detuned mid-infrared frequency conversion via normal dispersion modulation instability in chalcogenide microwires. *Optics letters*, 39(7), 1885-1888.

[7] Al-Kadry, A., & Rochette, M. (2013). Maximized soliton self-frequency shift in nonuniform microwires by the control of third-order dispersion perturbation. *Journal of Lightwave Technology*, 31(9), 1462-1467.

[8] Al-Kadry, A., Baker, C., El Amraoui, M., Messaddeq, Y., & Rochette, M. (2013). Broadband supercontinuum generation in As 2 Se 3 chalcogenide wires by avoiding the two-photon absorption effects. *Optics letters*, 38(7), 1185-1187.

[9] Alfano, R. R., & Shapiro, S. L. (1970). Observation of self-phase modulation and small-scale filaments in crystals and glasses. *Physical Review Letters*, 24(11), 592.

[10] Kolesik, M., & Moloney, J. V. (2004). Nonlinear optical pulse propagation simulation: From Maxwell's to unidirectional equations. *Physical Review E*, 70(3), 036604.

[11] Brabec, T., & Krausz, F. (1997). Nonlinear optical pulse propagation in the single-cycle regime. *Physical Review Letters*, 78(17), 3282.

[12] Laegsgaard, J. (2007). Mode profile dispersion in the generalized nonlinear Schrödinger equation. *Optics express*, 15(24), 16110-16123.

[13] Genty, G., Kinsler, P., Kibler, B., & Dudley, J. M. (2007). Nonlinear envelope equation modeling of sub-cycle dynamics and harmonic generation in nonlinear waveguides. *Optics express*, 15(9), 5382-5387.

[14] Ferreira, M. F. (2011). *Nonlinear effects in optical fibers* (Vol. 2). John Wiley & Sons.

[15] Snyder, A. W., & Love, J. (2012). *Optical waveguide theory*. Springer Science & Business Media.

[16] Griffiths, D. J. (2010). *Introduction to quantum mechanics*. Pearson international edition (Pearson Prentice Hall, 2005).

[17] Blow, K. J., & Wood, D. (1989). Theoretical description of transient stimulated Raman scattering in optical fibers. *IEEE Journal of Quantum Electronics*, 25(12), 2665-2673.

[18] Agger, C., Petersen, C., Dupont, S., Steffensen, H., Lyngsø, J.K., Thomsen, C.L., Thøgersen, J., Keiding, S.R. & Bang, O. (2012). Supercontinuum generation in ZBLAN fibers—detailed comparison between measurement and simulation. *JOSA B*, 29(4), 635-645.

[19] Kibler, B., Dudley, J. M., & Coen, S. (2005). Supercontinuum generation and nonlinear pulse propagation in photonic crystal fiber: influence of the frequency-dependent effective mode area. *Applied Physics* B, 81(2-3), 337-342.

[20] Milam, D. (1998). Review and assessment of measured values of the nonlinear refractive-index coefficient of fused silica. *Applied optics*, 37(3), 546-550.

[21] DeMartini, F., Townes, C. H., Gustafson, T. K., & Kelley, P. L. (1967). Self-steepening of light pulses. *Physical Review*, 164(2), 312.

[22] Kolesik, M., Wright, E. M., & Moloney, J. V. (2004). Simulation of femtosecond pulse propagation in sub-micron diameter tapered fibers. *Applied Physics B*, 79(3), 293-300.

[23] Boyce, W. E., & DiPrima, R. C. (2012). *Elementary differential equations* (Vol. 6). New York: Wiley.

[24] Ferrando, A., Zacarés, M., de Córdoba, P. F., Binosi, D., & Montero, Á. (2005). Forward-backward equations for nonlinear propagation in axially invariant optical systems. *Physical Review E*, 71(1), 016601.

[25] Genty, G., Kibler, B., Kinsler, P., & Dudley, J. M. (2008). Harmonic extended supercontinuum generation and carrier envelope phase dependent spectral broadening in silica nanowires. *Optics express*, 16(15), 10886-10893.

[26] Liao, M., Chaudhari, C., Qin, G., Yan, X., Suzuki, T., & Ohishi, Y. (2009). Tellurite microstructure fibers with small hexagonal core for supercontinuum generation. *Optics Express*, 17(14), 12174-12182.

[27] Kinsler, P., & New, G. H. C. (2005). Wideband pulse propagation: Single-field and multifield approaches to Raman interactions. *Physical Review A*, 72(3), 033804.

[28] Dudley, J. M., Genty, G., & Coen, S. (2006). Supercontinuum generation in photonic crystal fiber. *Reviews of modern physics*, 78(4), 1135.

[29] Afshar, S., & Monro, T. M. (2009). A full vectorial model for pulse propagation in emerging waveguides with subwavelength structures part I: Kerr nonlinearity. *Optics express*, 17(4), 2298-2318.

[30] Wright, L. G., Christodoulides, D. N., & Wise, F. W. (2015). Controllable spatiotemporal nonlinear effects in multimode fibres. *Nature Photonics*, 9(5), 306.

[31] Picozzi, A., Millot, G., & Wabnitz, S. (2015). Nonlinear optics: Nonlinear virtues of multimode fibre. *Nature Photonics*, 9(5), 289.

[32] Poletti, F., & Horak, P. (2008). Description of ultrashort pulse propagation in multimode optical fibers. *JOSA B*, 25(10), 1645-1654.

[33] Wright, L. G., Ziegler, Z. M., Lushnikov, P. M., Zhu, Z., Eftekhar, M. A., Christodoulides, D. N., & Wise, F. W. (2017). Multimode nonlinear fiber optics: Massively parallel numerical solver, tutorial, and outlook. *IEEE Journal of Selected Topics in Quantum Electronics*, 24(3), 1-16.

[34] Birks, T. A., Wadsworth, W. J., & Russell, P. S. J. (2000). Supercontinuum generation in tapered fibers. *Optics letters*, 25(19), 1415-1417.

[35] Ranka, J. K., Windeler, R. S., & Stentz, A. J. (2000). Visible continuum generation in air–silica microstructure optical fibers with anomalous dispersion at 800 nm. *Optics letters*, 25(1), 25-27.

[36] Petersen, C.R., Møller, U., Kubat, I., Zhou, B., Dupont, S., Ramsay, J., Benson, T., Sujecki, S., Abdel-Moneim, N., Tang, Z. & Furniss, D. (2014). Mid-infrared supercontinuum covering the 1.4–13.3 μm molecular fingerprint region using ultra-high NA chalcogenide step-index fibre. *Nature Photonics*, 8(11), 830.

[37] Husakou, A. V., & Herrmann, J. (2001). Supercontinuum generation of higher-order solitons by fission in photonic crystal fibers. *Physical Review Letters*, 87(20), 203901.

[38] Dudley, J. M., Genty, G., Dias, F., Kibler, B., & Akhmediev, N. (2009). Modulation instability, Akhmediev Breathers and continuous wave supercontinuum generation. *Optics express*, 17(24), 21497-21508.

[39] Nicholson, J. W., Abeeluck, A. K., Headley, C., Yan, M. F., & Jørgensen, C. G. (2003). Pulsed and continuous-wave supercontinuum generation in highly nonlinear, dispersion-shifted fibers. *Applied Physics B*, 77(2-3), 211-218.

[40] Abeeluck, A. K., & Headley, C. (2005). Continuous-wave pumping in the anomalous- and normal-dispersion regimes of nonlinear fibers for supercontinuum generation. *Optics Letters*, 30(1), 61-63.

[41] Sánchez, A. D., Fierens, P. I., Hernández, S. M., Bonetti, J., Brambilla, G., & Grosz, D. F. (2018). Anti-Stokes Raman gain enabled by modulation instability in mid-IR waveguides. *JOSA B*, 35(11), 2828-2832.

[42] Liu, Y., Tu, H., & Boppart, S. A. (2012). Wave-breaking-extended fiber supercontinuum generation for high compression ratio transform-limited pulse compression. *Optics letters*, 37(12), 2172-2174.

[43] Tomlinson, W. J., Stolen, R. H., & Johnson, A. M. (1985). Optical wave breaking of pulses in nonlinear optical fibers. *Optics letters*, 10(9), 457-459.

[44] Fisher, R. A., & Bischel, W. K. (1975). Numerical studies of the interplay between self-phase modulation and dispersion for intense plane-wave laser pulses. *Journal of Applied Physics*, 46(11), 4921-4934.

[45] Zhang, Q., & Hayee, M. I. (2008). Symmetrized split-step Fourier scheme to control global simulation accuracy in fiber-optic communication systems. *Journal of Lightwave Technology*, 26(2), 302-316.

[46] Hult, J. (2007). A fourth-order Runge–Kutta in the interaction picture method for simulating supercontinuum generation in optical fibers. *Journal of Lightwave Technology*, 25(12), 3770-3775.

[47] Shampine, L. F., & Reichelt, M. W. (1997). The matlab ode suite. *SIAM journal on scientific computing*, 18(1), 1-22.

[48] MathWorks, (2019). *Fast Fourier Transform*. Retrieved October 15, 2019 from https://www.mathworks.com/help/matlab/ref/fft.html

[49] Sinkin, O. V., Holzlohner, R., Zweck, J., & Menyuk, C. R. (2003). Optimization of the split-step Fourier method in modeling optical-fiber communications systems. *Journal of lightwave technology*, 21(1), 61-68.

[50] Steel, R. G. JH-Torrie. 1960. Principles and procedures of statistics, with special reference to the biological sciences. *McGraw Hill Book Company*, Inc: London, 420, 425.

[51] Slusher, R. E., Lenz, G., Hodelin, J., Sanghera, J., Shaw, L. B., & Aggarwal, I. D. (2004). Large Raman gain and nonlinear phase shifts in high-purity As 2 Se 3 chalcogenide fibers. *JOSA B*, 21(6), 1146-1155.

[52] Hu, J., Menyuk, C. R., Shaw, L. B., Sanghera, J. S., & Aggarwal, I. D. (2010). Maximizing the bandwidth of supercontinuum generation in As_2Se_3 chalcogenide fibers. *Optics express*, 18(7), 6722-6739.

[53] Alt, R. (1978). Error propagation in fourier transforms. *Mathematics and Computers in Simulation*, 20(1), 37-43.

[54] Klimczak, M., Siwicki, B., Zhou, B., Bache, M., Pysz, D., Bang, O., & Buczyński, R. (2016). Coherent supercontinuum bandwidth limitations under femtosecond pumping at 2 µm in all-solid soft glass photonic crystal fibers. *Optics express*, 24(26), 29406-29416.

[55] Lorenc, D., Aranyosiova, M., Buczynski, R., Stepien, R., Bugar, I., Vincze, A., & Velic, D. (2008). Nonlinear refractive index of multicomponent glasses designed for fabrication of photonic crystal fibers. Applied Physics B, 93(2-3), 531.

[56] Kibler, B., Fischer, R., Genty, G., Neshev, D. N., & Dudley, J. M. (2008). Simultaneous fs pulse spectral broadening and third harmonic generation in highly nonlinear fibre: experiments and simulations. *Applied Physics B*, 91(2), 349-352.

[57] OFS Optics, (2019). *Highly Nonlinear Fiber Optical Fiber*. Retrieved October 30, 2019 from https://fiber-optic-catalog.ofsoptics.com/viewitems/optical–fibers/highly-nonlinear-fiber-optical-fibers1

[58] Demircan, A., & Bandelow, U. (2007). Analysis of the interplay between soliton fission and modulation instability in supercontinuum generation. *Applied Physics B*, 86(1), 31-39.

[59] Venck, S., St-Hilaire, F., Ghosh, A. N., Chahal, R., Caillaud, C., Meneghetti, M., Troles, J., Joulain, F., Cozic, S., Poulain, S., Huss, G., Rochettem, M., Dydley, J., Brilland, L., & Sylvestre, T. 2-10 μm Mid-Infrared Supercontinuum Generation in Cascaded Optical Fibers: Experiment and Simulation, *SPIE Photonics West*, LASE, paper 11264-8, San Francisco, Feb. 3, 2020.

[60] Efimov, A., Taylor, A. J., Omenetto, F. G., Knight, J. C., Wadsworth, W. J., & Russell, P. S. J. (2003). Phase-matched third harmonic generation in microstructured fibers. *Optics Express*, 11(20), 2567-2576.

[61] Le Verre Fluoré, (2019). *ZFG Singlemode*. Retrieved November 2, 2019 from https://leverrefluore.com/products/passive-fibers/zfg-singlemode/

[62] Saghaei, H., Ebnali-Heidari, M., & Moravvej-Farshi, M. K. (2015). Midinfrared supercontinuum generation via As2 Se3 chalcogenide photonic crystal fibers. *Applied optics*, 54(8), 2072-2079.

[63] Cui, S., Boussard-Plédel, C., Troles, J., & Bureau, B. (2016). Telluride glass single mode fiber for mid and far infrared filtering. *Optical Materials Express*, 6(4), 971-978.

[64] Cheng, T., Nagasaka, K., Tuan, T. H., Xue, X., Matsumoto, M., Tezuka, H., ... & Ohishi, Y. (2016). Mid-infrared supercontinuum generation spanning 2.0 to 15.1 μm in a chalcogenide step-index fiber. *Optics letters*, 41(9), 2117-2120.

Appendix

A. SSFM code for the GNLSE

```
function [A, Af] = GNLSE_SSFM_func(E,L,h_ratio,gamma0,taushock,chi,fR,
    betas,maxorder,wrel,dt,lossw,shift,npts,nplots)

    %%%%%%%%%%%%%%%%%%%%%%%%%%%%%%%%%%%%%%%%%%%%%%%%%%%%%%%%%%%%%%%%%%%%%%%%
    % Francois St-Hilaire, MEng, McGill University                          %
    % Adapted from a J.M. Dudley code (Femto-ST)                            %
    % This function solves the GNLSE                                        %
    % With a SSFM and adaptive step size method.                            %
    % Inputs: E = Initial time domain envelope                              %
    %         L = Fiber length                                              %
    %         h_ratio = Inverse of max phase shift per step                 %
    %         gamma0 = NL parameter at center wavelength                    %
    %         taushock = shock timescale                                    %
    %         chi = Ramain gain FT(h_R)                                     %
    %         fR = Raman fraction                                           %
    %         betas = vector of beta coefficients [B2 B3 B4 B5...]          %
    %         maxorder = max beta order                                     %
    %         wrel = relative angular frequency vector centered at w0       %
    %         w0 = reference frequency                                      %
    %         t = time vector                                               %
    %         dt = time increment                                           %
    %         lossw = losses [1/m]                                          %
    %         shift = shift amount fro frequency window                     %
    %         npts = number of discretization points                        %
    %         nplots = number of saved propagation points                   %
    % Outputs: A = Pulse envelope saved at nplots points in z               %
    %          Af = Pulse spectrum saved at nplots points in z              %
    %%%%%%%%%%%%%%%%%%%%%%%%%%%%%%%%%%%%%%%%%%%%%%%%%%%%%%%%%%%%%%%%%%%%%%%%


```

```
31      E = fftshift(E);
32      z = 0;
33      ind1 = [(2:npts) 1];
34      ind2 = [npts (1:npts-1)];
35      sel = (L/(nplots-1));
36      plotsel = sel;
37      plotn = 1;
38      A = zeros(nplots,npts);
39      Af = zeros(nplots,npts);
40      A(1,:) = fftshift(E);
41      Af(1,:) = fftshift(circshift((fft(E)),shift));
42      beta = 0;
43          for ii = 2:maxorder
44              beta = beta + betas(ii-1).*wrel.^(ii)./factorial(ii);
45          end
46      beta = fftshift(beta);
47
48      k = 0;
49      while z<L
50        k = k+1;
51          %% Nonlinear step
52          A0 = E;
53          peakP = max(abs(E).^2);
54          h = (1./(gamma0.*peakP))./h_ratio;
55          IFT = fft(abs(A0).^2);
56          Iz = (1-fR)*(abs(A0).^2)+fR*ifft(chi.*IFT);
57          NLfn = A0.*Iz;
58          A1 = A0-h/2*1/(2*dt).*gamma0.*taushock.*(NLfn(ind1)-NLfn(ind2));
59          IFT = fft(abs(A1).^2);
60          Izh = (1-fR)*(abs(A1).^2)+fR*ifft(chi.*IFT);
61          NLfn = A1.*Izh;
62          A1 = A0-h.*1i.*gamma0.*A1.*(Izh-Iz)-h.*1./(2.*dt).*gamma0.*
                taushock.*(NLfn(ind1)-NLfn(ind2));
63          E  = A1.*exp(-1i.*gamma0.*h.*Iz);
64
65          %% Dispersion + birefringence step
```

```
66          betaop = exp(-1i*h*beta);
67          EFT = circshift(fft(E),shift);
68          EFT = EFT.*betaop;
69
70          %%  Include loss
71          EFT= EFT.*(fftshift(exp(-lossw.*h)));
72          E  = ifft(circshift(EFT,-shift));
73          z = z+h
74
75          %% save
76          if (z > plotsel)
77             plotsel = plotsel+sel;
78             plotn = plotn+1;
79             A(plotn,:) =  fftshift(E);
80             Af(plotn,:) = fftshift(EFT);
81          end
82      end
83  end
```

B. IP-RK4 code for the FD-GNLSE

```
function [A, Af] = FDGNLSE_RK4_func(E,L,h_ratio,gamma,gamma0,Aeff,Aeff0,
    chi,fR,betas,maxorder,wrel,lossw,shift,npts,nplots)

    %%%%%%%%%%%%%%%%%%%%%%%%%%%%%%%%%%%%%%%%%%%%%%%%%%%%%%%%%%%%%%%%%%%%%%%%
    % Francois St-Hilaire, MEng, McGill University                          %
    % This function solves the FD-GNLSE from Travers et al. (2010)         %
    % 'Nonlinear Fiber optics overview'                                     %
    % With an IP RK4 method and adaptive step size method.                  %
    % Inputs: E = Initial time domain envelope                              %
    %         L = Fiber length                                              %
    %         h_ratio = Inverse of max phase shift per step                 %
    %         gamma = n2*w/(c*sqrt(Aeff0 *Aeff(w)))                         %
    %         gamma0 = NL parameter at center wavelength                    %
    %         Aeff = frequency dependent effective area                     %
    %         Aeff0 = Aeff at reference frequency                           %
    %         chi = Ramain gain FT(h_R)                                     %
    %         fR = Raman fraction                                           %
    %         betas = vector of beta coefficients [B2 B3 B4 B5...]          %
    %         maxorder = max beta order                                     %
    %         wrel = relative angular frequency vector centered at w0       %
    %         lossw = losses [1/m]                                          %
    %         shift = shift amount fro frequency window                     %
    %         npts = number of discretization points                        %
    %         nplots = number of saved propagation points                   %
    % Outputs: A = Pulse envelope saved at nplots points in z               %
    %          Af = Pulse spectrum saved at nplots points in z              %
    %%%%%%%%%%%%%%%%%%%%%%%%%%%%%%%%%%%%%%%%%%%%%%%%%%%%%%%%%%%%%%%%%%%%%%%%

    Aeff = fftshift(Aeff);
    gamma = fftshift(gamma);
    E = fftshift(E);
    z = 0;
    EFT = circshift(fft(E),shift);
```

```
33      CFT = (Aeff./Aeff0).^(-1/4).*EFT;
34      sel = (L/(nplots-1));
35      plotsel = sel;
36      plotn = 1;
37      A = zeros(nplots,npts);
38      Af = zeros(nplots,npts);
39      A(1,:) = fftshift(E);
40      Af(1,:) = fftshift(circshift((fft(E)),shift));
41      beta = 0;
42          for ii = 2:maxorder
43              beta = beta + betas(ii-1).*wrel.^(ii)./factorial(ii);
44          end
45      beta = fftshift(beta);
46      k = 0;
47      while z<L
48        k = k+1;
49          A0 = E;
50          peakP = max(abs(A0).^2);
51          h = (1./(gamma0.*peakP))./h_ratio;
52          C = ifft(circshift(CFT.*exp(-1i.*beta.*z),-shift));
53          IFT = fft(abs(C).^2);
54          Iz = (1-fR)*(abs(C).^2)+fR*ifft(chi.*IFT);
55          k1 = -1i.*gamma.*circshift(fft(C.*Iz),shift).*exp(1i.*beta.*z);
56          CFT1 = CFT+k1.*h./2;
57          C = ifft(circshift(CFT1.*exp(-1i.*beta.*(z+h/2)),-shift));
58          IFT = fft(abs(C).^2);
59          Iz = (1-fR)*(abs(C).^2)+fR*ifft(chi.*IFT);
60          k2 = -1i.*gamma.*circshift(fft(C.*Iz),shift).*exp(1i.*beta.*(z+h
               /2));
61          CFT1 = CFT+k2.*h./2;
62          C = ifft(circshift(CFT1.*exp(-1i.*beta.*(z+h/2)),-shift));
63          IFT = fft(abs(C).^2);
64          Iz = (1-fR)*(abs(C).^2)+fR*ifft(chi.*IFT);
65          k3 = -1i.*gamma.*circshift(fft(C.*Iz),shift).*exp(1i.*beta.*(z+h
               /2));
66          CFT1 = CFT + h.*k3;
```

```
67          C = ifft(circshift(CFT1.*exp(-1i.*beta.*(z+h)),-shift));
68          IFT = fft(abs(C).^2);
69          Iz = (1-fR)*(abs(C).^2)+fR*ifft(chi.*IFT);
70          k4 = -1i.*gamma.*circshift(fft(C.*Iz),shift).*exp(1i.*beta.*(z+h))
                ;
71          CFT = CFT + (k1/6+k2/3+k3/3+k4/6).*h;
72
73          %%   Include loss
74          CFT= CFT.*(fftshift(exp(-lossw.*h)));
75          E  = ifft(circshift(CFT.*(Aeff./Aeff0).^(1/4).*exp(-1i.*beta.*z),-
                shift));
76          z = z+h
77
78          %% save
79          if (z > plotsel)
80             plotsel = plotsel+sel;
81             plotn = plotn+1;
82             A(plotn,:) =  fftshift(E);
83             Af(plotn,:) = fftshift(CFT.*(Aeff./Aeff0).^(1/4).*exp(-1i.*beta
                   .*z));
84          end
85      end
86  end
```

C. SSFM code for the GNEE

```
function [A, Af] = GNEE_SSFM_func(E,L,h_ratio,gamma0,taushock,chi,chi_p,fR
    ,betas,maxorder,wrel,w0,t,dt,lossw,shift,npts,nplots)

    %%%%%%%%%%%%%%%%%%%%%%%%%%%%%%%%%%%%%%%%%%%%%%%%%%%%%%%%%%%%%%%%%%%%%%%%
    % Francois St-Hilaire, MEng, McGill University                          %
    % Adapted from a J.M. Dudley code (Femto-ST)                            %
    % This function solves the GNEE from Kibler et al. (2007)              %
    % Nonlinear envelope equation modeling of sub-cycle dynamics and       %
    % harmonic generation in nonlinear waveguides.                          %
    % With a SSFM and adaptive step size method.                            %
    % Inputs: E = Initial time domain envelope                              %
    %         L = Fiber length                                              %
    %         h_ratio = Inverse of max phase shift per step                 %
    %         gamma0 = NL parameter at center wavelength                    %
    %         taushock = shock timescale                                    %
    %         chi = Ramain gain FT(h_R)                                     %
    %         chi_p = FT(h'_R) (see reference paper)                        %
    %         fR = Raman fraction                                           %
    %         betas = vector of beta coefficients [B2 B3 B4 B5...]          %
    %         maxorder = max beta order                                     %
    %         wrel = relative angular frequency vector centered at w0       %
    %         w0 = reference frequency                                      %
    %         t = time vector                                               %
    %         dt = time increment                                           %
    %         lossw = losses [1/m]                                          %
    %         shift = shift amount fro frequency window                     %
    %         npts = number of discretization points                        %
    %         nplots = number of saved propagation points                   %
    % Outputs: A = Pulse envelope saved at nplots points in z               %
    %          Af = Pulse spectrum saved at nplots points in z              %
    %%%%%%%%%%%%%%%%%%%%%%%%%%%%%%%%%%%%%%%%%%%%%%%%%%%%%%%%%%%%%%%%%%%%%%%%

    E = fftshift(E);
```

```
33      z = 0;
34      ind1 = [(2:npts) 1];
35      ind2 = [npts (1:npts-1)];
36      sel = (L/(nplots-1));
37      plotsel = sel;
38      plotn = 1;
39      A = zeros(nplots,npts);
40      Af = zeros(nplots,npts);
41      A(1,:) = fftshift(E);
42      Af(1,:) = fftshift(circshift((fft(E)),shift));
43
44      beta = 0;
45          for ii = 2:maxorder
46              beta = beta + betas(ii-1).*wrel.^(ii)./factorial(ii);
47          end
48
49      beta = fftshift(beta);
50
51      k = 0;
52      while z<L
53        k = k+1;
54          %% Nonlinear step
55          A0 = E;
56          peakP = max(abs(E).^2);
57          h = (1./(gamma0.*peakP))./h_ratio;
58          IFT = fft(abs(A0).^2);
59          g = (2/3).*ifft(chi.*IFT);
60          Iz = (1-fR)*(abs(A0).^2+(1/3).*exp(1i.*2.*w0.*t).*A0.^2)+fR.*g;
61          NLfn = A0.*Iz+fR.*(2/3).*ifft(chi_p.*fft(A0.^2)).*exp(1i.*w0.*t).*
                real(exp(1i.*w0.*t).*A0);
62          A1 = A0-h/2*1/(2*dt).*gamma0.*taushock.*(NLfn(ind1)-NLfn(ind2));
63          IFT = fft(abs(A1).^2);
64          g = (2/3).*ifft(chi.*IFT);
65          Izh = (1-fR)*(abs(A1).^2+(1/3).*exp(1i.*2.*w0.*t).*A1.^2)+fR.*g;
66          NLfn = A1.*Izh+fR.*(2/3).*ifft(chi_p.*fft(A1.^2)).*exp(1i.*w0.*t)
                .*real(exp(1i.*w0.*t).*A1);
```

```
67          A1 = A0-h.*1i.*gamma0.*A1.*(Izh-Iz)-h.*1./(2.*dt).*gamma0.*
                taushock.*(NLfn(ind1)-NLfn(ind2));
68          E  = A1.*exp(-1i.*gamma0.*h.*Iz);
69
70          %% Dispersion + birefringence step
71          betaop = exp(-1i*h*beta);
72          EFT = circshift(fft(E),shift);
73          EFT = EFT.*betaop;
74
75          %%   Include loss
76          EFT= EFT.*(fftshift(exp(-lossw.*h)));
77          E  = ifft(circshift(EFT,-shift));
78          z = z+h
79
80          %% save
81          if (z > plotsel)
82             plotsel = plotsel+sel;
83             plotn = plotn+1;
84             A(plotn,:) =  fftshift(E);
85             Af(plotn,:) = fftshift(EFT);
86          end
87      end
88  end
```

C. IP-RK4 code for the GNEE

```
function [A, Af,plotn] = GNEE_RK4_func(E,L,h_ratio,gamma0,taushock,chi,
    chi_p,fR,betas,maxorder,wrel,w0,t,lossw,shift,npts,nplots)

    %%%%%%%%%%%%%%%%%%%%%%%%%%%%%%%%%%%%%%%%%%%%%%%%%%%%%%%%%%%%%%%%%%%%%%%%
    % Francois St-Hilaire, MEng, McGill University                          %
    % This function solves the GNEE from Kibler et al. (2007)              %
    % Nonlinear envelope equation modeling of sub-cycle dynamics and        %
    % harmonic generation in nonlinear waveguides.                          %
    % With an IP RK4 method and adaptive step size method.                  %
    % Inputs: E = Initial time domain envelope                              %
    %         L = Fiber length                                              %
    %         h_ratio = Inverse of max phase shift per step                 %
    %         gamma0 = NL parameter at center wavelength                    %
    %         taushock = shock timescale                                    %
    %         chi = Ramain gain FT(h_R)                                     %
    %         chi_p = FT(h'_R) (see reference paper)                        %
    %         fR = Raman fraction                                           %
    %         betas = vector of beta coefficients [B2 B3 B4 B5...]          %
    %         maxorder = max beta order                                     %
    %         wrel = relative angular frequency vector centered at w0       %
    %         w0 = reference frequency                                      %
    %         t = time vector                                               %
    %         lossw = losses [1/m]                                          %
    %         shift = shift amount fro frequency window                     %
    %         npts = number of discretization points                        %
    %         nplots = number of saved propagation points                   %
    % Outputs: A = Pulse envelope saved at nplots points in z               %
    %          Af = Pulse spectrum saved at nplots points in z              %
    %%%%%%%%%%%%%%%%%%%%%%%%%%%%%%%%%%%%%%%%%%%%%%%%%%%%%%%%%%%%%%%%%%%%%%%%

    E = fftshift(E);
    z = 0;
    sel = (L/(nplots-1));
```

```
33      plotsel = sel;
34      plotn = 1;
35      A = zeros(nplots,npts);
36      Af = zeros(nplots,npts);
37      A(1,:) = fftshift(E);
38      Af(1,:) = fftshift(circshift((fft(E)),shift));
39      beta = 0;
40          for ii = 2:maxorder
41              beta = beta + betas(ii-1).*wrel.^(ii)./factorial(ii);
42          end
43      beta = fftshift(beta);
44
45      k = 0;
46      while z<L
47        k = k+1;
48          %% Nonlinear step
49          A0 = E;
50          Af0 = circshift(fft(A0),shift).*exp(1i.*beta.*z);
51          peakP = max(abs(E).^2);
52          h = (1./(gamma0.*peakP))./h_ratio;
53          IFT = fft(abs(A0).^2);
54          g = (2/3).*ifft(chi.*IFT);
55          Iz = (1-fR)*(abs(A0).^2+(1/3).*exp(1i.*2.*w0.*t).*A0.^2)+fR.*g;
56          NLfn = A0.*Iz+fR.*(2/3).*ifft(chi_p.*fft(A0.^2)).*exp(1i.*w0.*t).*
                real(exp(1i.*w0.*t).*A0);
57          k1 =-1i.*(1+taushock.*wrel).*gamma0.*circshift(fft(NLfn),shift).*
                exp(1i.*beta.*z);
58          Af1 = Af0+(h./2).*k1;
59          A1 = ifft(circshift(Af1.*exp(-1i.*beta.*(z+h/2)),-shift));
60          IFT = fft(abs(A1).^2);
61          g = (2/3).*ifft(chi.*IFT);
62          Iz = (1-fR)*(abs(A1).^2+(1/3).*exp(1i.*2.*w0.*t).*A1.^2)+fR.*g;
63          NLfn = A1.*Iz+fR.*(2/3).*ifft(chi_p.*fft(A1.^2)).*exp(1i.*w0.*t).*
                real(exp(1i.*w0.*t).*A1);
64          k2 = -1i.*(1+taushock.*wrel).*gamma0.*circshift(fft(NLfn),shift).*
                exp(1i.*beta.*(z+h/2));
```

```
65          Af1 = Af0 + h./2.*k2;
66          A1 = ifft(circshift(Af1.*exp(-1i.*beta.*(z+h/2)),-shift));
67          IFT = fft(abs(A1).^2);
68          g = (2/3).*ifft(chi.*IFT);
69          Iz = (1-fR)*(abs(A1).^2+(1/3).*exp(1i.*2.*w0.*t).*A1.^2)+fR.*g;
70          NLfn = A1.*Iz+fR.*(2/3).*ifft(chi_p.*fft(A1.^2)).*exp(1i.*w0.*t).*
               real(exp(1i.*w0.*t).*A1);
71          k3 = -1i.*(1+taushock.*wrel).*gamma0.*circshift(fft(NLfn),shift).*
               exp(1i.*beta.*(z+h/2));
72          Af1 = Af0 + h.*k3;
73          A1 = ifft(circshift(Af1.*exp(-1i.*beta.*(z+h)),-shift));
74          IFT = fft(abs(A1).^2);
75          g = (2/3).*ifft(chi.*IFT);
76          Iz = (1-fR)*(abs(A1).^2+(1/3).*exp(1i.*2.*w0.*t).*A1.^2)+fR.*g;
77          NLfn = A1.*Iz+fR.*(2/3).*ifft(chi_p.*fft(A1.^2)).*exp(1i.*w0.*t).*
               real(exp(1i.*w0.*t).*A1);
78          k4 = -1i.*(1+taushock.*wrel).*gamma0.*circshift(fft(NLfn),shift).*
               exp(1i.*beta.*(z+h));
79          Af2 = Af0 + (k1/6+k2/3+k3/3+k4/6).*h;
80          EFT = Af2.*exp(-1i.*beta.*(z+h));
81
82          %%   Include loss
83          EFT= EFT.*(fftshift(exp(-lossw.*h)));
84          E  = ifft(circshift(EFT,-shift));
85          z = z+h
86
87          %% save
88          if (z > plotsel)
89             plotsel = plotsel+sel;
90             plotn = plotn+1;
91             A(plotn,:) =  fftshift(E);
92             Af(plotn,:) = fftshift(EFT);
93          end
94
95      end
96  end
```